Towards the Certification of Bonded Primary Fiber Metal Laminate Structures by Bolted Disbond Arrest Features

I. van Teeseling

Technische Universiteit Delft

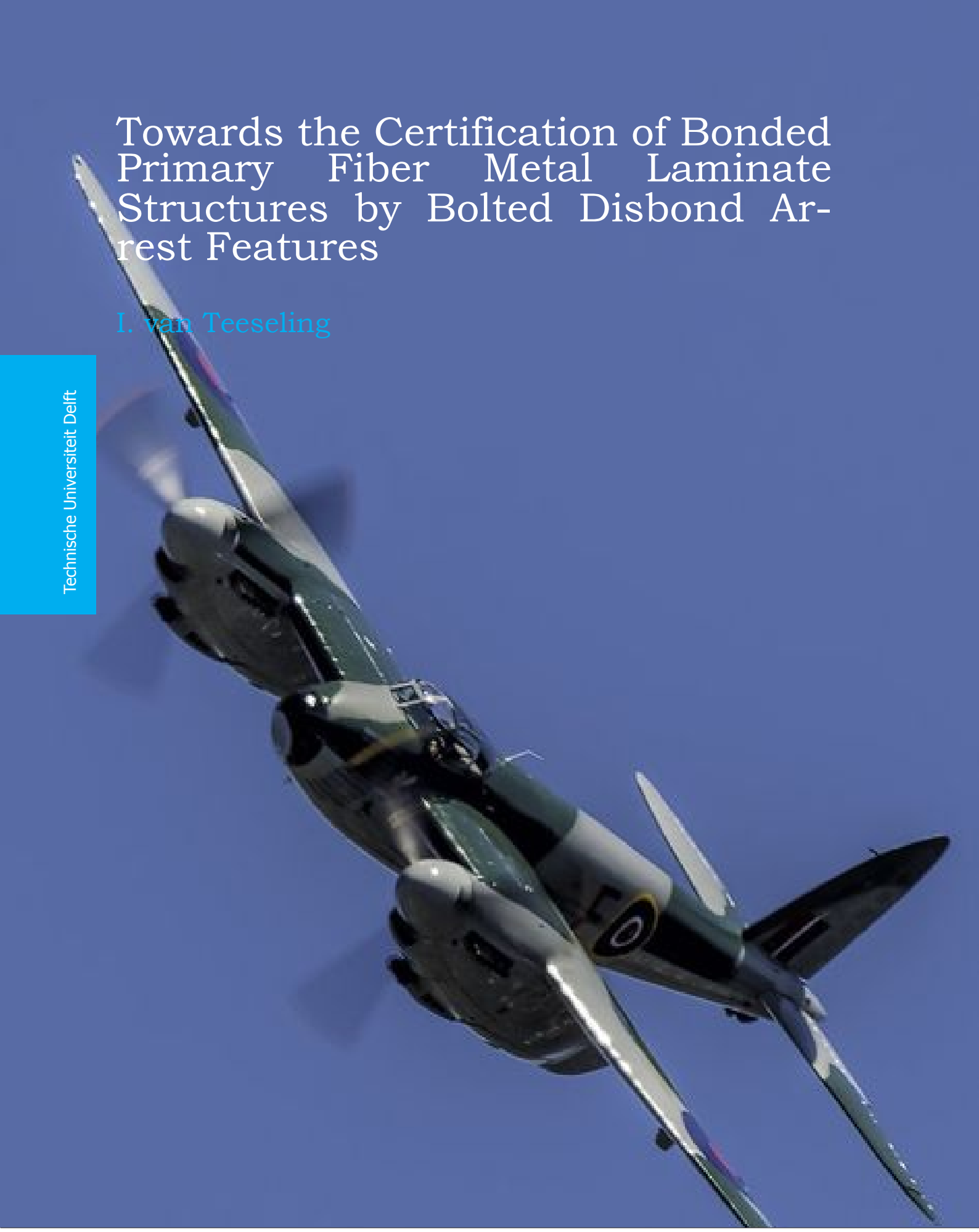

TU Delft Delft University of Technology

Challenge the future

Towards the Certification of Bonded Primary Fiber Metal Laminate Structures by Bolted Disbond Arrest Features

by

I. van Teeseling

in partial fulfillment of the requirements for the degree of

Master of Science
in Aerospace Engineering

at the Delft University of Technology,
to be defended publicly on Monday January 7, 2019 at 09:30 AM.

Supervisor:	Dr. C. D. Rans	
Thesis committee:	Dr. ir. R. C. Alderliesten,	TU Delft
	Dr. C. Kassapoglou,	TU Delft
	Dr. I. Fernandez Villegas,	TU Delft

TU Delft Delft University of Technology

Acknowledgements

Writing this sentence means that I am approaching the end station of the most challenging roller coaster that I have experienced in my professional and academic life. The past few months have brought me moments of excitement, disappointments, complete and utter identity crises and finally a proud sense of accomplishment. For me it was very important to make the most out of this unique opportunity to devote so much of your time to a project that can be shaped by your own personal interest. I can happily say that I have achieved just that.

Of course, writing this thesis would not have been possible without a group of important people to whom I would like to express my gratitude.

I cannot start thanking anyone else than my daily super visor: Calvin Rans. Early on, I decided that the success of the thesis would mainly depend on having the right supervisor. For me, this has been proven to be correct after working together with Calvin. His unique ability to appreciate an individual's way of thinking and to adopt his supervising methods accordingly has been very inspirational. Despite my continuous harassment in the form of panicking emails and running by at Calvin's office without any notice seeking for help, Calvin always showed a willingness to help and to teach. Thank you, Calvin!

I want to thank Thomas Kruse from Airbus for taking me under his wing and freeing up several days of his schedule to get me started. And of course: thank you for the awesome tour through the Airbus production plants in Finkenwerder!

I am very grateful towards the staff of the Aerospace Structures and Materials Laboratory, particularly Cees and Gertjan. Without the experience and help of Cees, none of the specimens and components needed for my experimental tests would have been possible. In a similar way, the help of Gerjan was crucial in getting the final test setup to work. Thank you both!

The same goes for the DEMO staff whom I value greatly for their patience and for always responding so quickly to problems that needed fixing. Ed, thank you for the many hours of work spend on helping me with finishing the specimens!

Of course, I also want to thank my thesis committee for being part of my final graduation; René Alderliesten, Christos Kassapoglou and Irene fernandez villegas.

Thank you to all my fellow students in general and Bart, Bram and Derron in particular. Sharing ideas and discussions with the three of you has taught me a lot and it has been a great contribution to my overall experience.

Finally, I want to thank my father, Eric van Teeseling, for helping me by providing critical and valuable feedback on the report.

I. van Teeseling
Delft, December 2018

Summary

Joining primary structures today still relies on mechanical fastening, despite its drawbacks in the now widely used anisotropic materials such as GLAss REinforced aluminum (GLARE) and Fibre Reinforced Polymers (FRP). Bonding is a promising alternative [1], but its application is hindered by a lack of confidence in its damage tolerance behavior and the difficulties associated with quality assurance. Certification of bonded primary joints could be feasibly by demonstrating the ability to achieve the arrest or at least retardation of damage growth by Disbond Arrest Features (DAF).

Bolted DAFs have been shown to arrest quasi static [2] and fatigue disbond growth [3–6] in bonded Carbon Fibre Reinforced Polymers (CFRP) specimens. In bonded Fibre Metal Laminate (FML) specimens the retardation of disbond growth by bolted DAFs lasted only briefly due to the initiation and growth of adherend fatigue damages [7]. Overall, a fundamental understanding of the mechanisms behind the arrest of disbond growth and their interaction with adherend fatigue damages is lacking.

This research aims to establish both the potential and weaknesses of bolts as DAFs in bonded FML joints under fatigue loading. More specific, it focuses on (1) the conditions necessary for arrest, (2) the conditions provided by a bolt as DAF, (3) the effect of adherend fatigue damages on the arrest of disbond growth and (4) whether a slow growing disbond front can initiate a fatigue crack.

Cracked Lap Shear (CLS) specimens with either a self developed Clamped Disbond Arrest Feature (CDAF) or a Bolted Disbond Arrest Feature (BDAF) have been fatigue tested. The CDAF is used to study the effect on disbond growth of reducing the Mode I Strain Energy Release Rate (SERR) and to see if an arrested disbond front can initiate a fatigue crack. A quasi analytical disbond growth model has been developed to study the conditions necessary for arrest and the relation between the DGR and fatigue crack initiation due to the disbond front. The CDAF is modeled by including its effect on the SERR which is calculated using a Finite Element Method (FEM) model.

Experimental and model results with the CDAF in place displayed that Mode I reduction has a superior effectiveness in the arrest of disbond growth compared to Mode II. However, model simulations indicate the need for Mode II reduction at elevated loads. Numerical analysis of the SERR with a CDAF showed that Mode I reduction depends on the applied clamping pressure, but also that its effect quickly diminishes further away from the pressure-loaded area. It has consistently been observed that a fatigue crack initiates in the direct proximity of the disbond front when fully arrested by the CDAF. This was successfully replicated by the quasi analytical model. The FML adherends failed in fatigue before the effect of adherend fatigue damage on the arrest of disbond growth could be studied.

Based on these observations, two conclusions are drawn. First, Mode I reduction is the main driver for achieving the arrest of disbond growth. Second, an arrested disbond front can initiate a fatigue crack.

The following is suggested, but cannot be concluded. First, the discrete clamping pressure of a bolt as DAF is not effective in widely spreading the reduction of Mode I. Second, experimental results suggest that the initiation and growth of fatigue cracks in the FML adherends might be a bigger problem than the actual disbond growth.

In the process, a novel quasi analytical model has been developed and validated to predict the disbond growth and fatigue crack initiation in a FML CLS specimen with or without a CDAF under Constant Amplitude (CA) loading with a fixed R-ratio. Also, an algorithm has been developed and verified which can locate the disbonded region using Digital Image Correlation (DIC) by leveraging knowledge of the strain field in relation to the disbond front.

Contents

List of Figures

List of Tables

Acronyms

1D 1-dimensional. 15, 29, 79, 80, 82

2D 2-dimensional. 4, 6, 15, 30, 33, 45, 47, 50, 80, 82

3D 3-dimensional. 6, 12, 55, 77, 82

Arall Aramide Reinforced ALuminium Laminate. 8

BDAF Bolted Disbond Arrest Feature. v, xi, xii, 17, 20–22, 25, 26, 35, 37–44, 47, 51, 54–64, 72, 73, 77–79, 81, 82, 89, 92

BOPACS Boltless Assembling of Primary Aerospace Composite Structures. 2, 4–6, 11, 18, 20

CA Constant Amplitude. v, xiii, 24, 87, 99, 100

CARALL CArbon Reinforced ALuminium Laminate. 8

CDAF Clamped Disbond Arrest Feature. v, xi, xii, xx, 17, 20–22, 25, 26, 33–35, 37–39, 41–44, 47–62, 64–68, 70–73, 76, 77, 81, 82, 89, 92

CFRP Carbon Fibre Reinforced Polymers. v, xi, 1–7, 13, 18, 20

CLS Cracked Lap Shear. v, xi–xiii, xv, 6, 7, 11, 12, 15, 17–24, 28–33, 35–37, 44–46, 50–52, 55, 62, 63, 66, 75–77, 79–87, 91

CLT Classical Laminate Theory. 31

CTE Coefficient of Thermal Expansion. 9

CZM Cohesive Zone Model. 10

DAF Disbond Arrest Features. v, xi, xii, xv, xx, 2–8, 10–15, 17, 18, 20–23, 26, 28, 29, 35–39, 41, 44, 47, 48, 50, 52, 53, 55–58, 60–62, 66, 69, 70, 72, 73, 75–78, 80–82, 87

DAGR Disbond Area Growth Rate. xi, xii, 23, 27, 28, 35, 51, 54–56, 81

DCB Double Cantilever Beam. xiii, 99, 100

DGR Disbond Growth Rate. v, xi, xii, 2, 4, 6, 7, 12, 15–18, 23–30, 32, 35, 37, 38, 48, 51–57, 59–61, 64–73, 76, 78–82, 87, 88

DIC Digital Image Correlation. v, xi, xiii, 11, 12, 25–28, 35, 38–41, 55, 76, 82, 95

FAA Federal Aviation Authorities. 2, 4

FCG Factige Crack Growth. 9

FEA Finite Element Analysis. 4

FEM Finite Element Method. v, xi, xiii, 2, 4, 6, 7, 10, 17, 32, 33, 45, 47, 48, 55, 82–86

FM Fracture Mechanics. 10

FML Fibre Metal Laminate. v, xi, xii, 1–4, 7–11, 13–16, 23, 28–31, 33, 35, 47, 57, 65, 66, 75, 76, 78–80, 87, 90

FRP Fibre Reinforced Polymers. v, 1

GF Glass Fiber. 19, 20, 38, 82, 99

GFRP Glass Fibre Reinforced Polymers. 8, 10

GLARE GLAss REinforced aluminum. v, xi, 6, 8–10, 19, 20, 23, 24, 45, 79, 99

LEFM Linear Elastic Fracture Mechanics. 3, 10, 11, 29, 30, 32, 99

MM Mixed Mode. xv, 4, 6, 7, 11, 12, 29, 30, 32, 56, 73, 82, 99, 101, 102

MR Mode Ratio. xii, 11, 12, 32, 44, 45, 79, 84, 86, 100, 101

MVF Mixed Volume Fraction. 87

NDI Non Destructive Inspection. 2, 11, 76

PM Palmgren–Miner. 30, 33, 71

SERR Strain Energy Release Rate. v, xii, xiii, xix, 3, 4, 6, 10–12, 14, 17, 28–33, 35, 44–51, 53–56, 58, 59, 64–66, 69, 70, 72, 75, 77, 79–86

SIF Stress Intensity Factor. 10

SLJ Single Lap Joint. xii, 12, 31, 63

TUDelft Delft University of Technology. 4, 5, 23

UD Un Directional. 19, 20, 38, 82, 99

VA Variable Amplitude. 29, 79

VCCT Virtual Crack Closure Technique. 6, 33, 45, 82

WSLS Wide Single Lap Shear. xi, 6, 7

XFEM Extended Finite Element Method. 10

Nomenclature

Symbols

Symbol	Description	Unit
b	Disbond length	$[mm]$
i	Disbond increment	$[-]$
m	Interface coefficient in the Paris relation (exponent by [8])	$[-]$
n	Interface coefficient in the Paris relation	$[-]$
v	Poisson's ratio	$[-]$
A	Area	$[mm^2]$
Ae	Aspect ratio of the disbonded region	$[-]$
C	Interface coefficient in the Paris relation	Function of $[m]$
F	Force	$[N]$
G	Strain Energy Release Rate (SERR)	$[N/m^2]$
L	Length	$[mm]$
N	Load cycle	$[cycle]$
P	Pressure	$[MPa]$
S	Nominal stress	$[MPa]$
T	Temperature	$[C^\circ]$
t	Thickness	$[mm]$
W	Width	$[mm]$
da/dN	Crack growth rate	$[mm/cycle]$
db/dN	Disbond growth rate	$[mm/cycle]$
dA_b/dN	Disbond area growth rate	$[mm^2/cycle]$
dT	Temperature difference	$[C^\circ]$
$G_{eq,1}$	Linear elastic fracture parameter (from [8])	$[N/m^2]$
$G_{\%}$	SERR footprint	$[-]$

Subscripts

Symbol	Description
a	Adhesive
$application$	Application
ave	Average
b	Disbond
$crack$	Crack
$cure$	Curing
$c1$	Clamped region 1
$c2$	Clamped region 2
max	Maximum
min	Minimum
$taper$	Taper
xy	xy-direction
yx	yx-direction
AC	Point A to C
BC	Point B to C
CB	Point C to B
$CDAF$	Clamped Disbond Arrest Feature (CDAF)
DAF	Disbond Arrest Features (DAF)
L	Left
R	Right
I	Mode I
II	Mode II
III	Mode III
I/II	Mixed Mode I and II
$I/II/III$	Mixed Mode I, II and III
0%	Pure Mode I
100%	Pure Mode II
$21kN$	Fatigue load of 21 kN
$26kN$	Fatigue load of 26 kN
$28kN$	Fatigue load of 28 kN

1

Introduction

The past decades have seen a growing trend in the development and application of new aerospace materials and novel structural concepts to answer an increasing industry need to reduce aircraft weight, prolong operational life, minimize (un)scheduled downtime and to reduce maintenance cost [1]. Examples include the application of the fatigue superior material GLARE in the A380, Fibre Reinforced Polymers (FRP) which represent more than 50% of the total airframe weight in the B787 [22] and A350 [23] and the Carbon Fibre Reinforced Polymers (CFRP) wings in the new A220 (previously CSeries) aircraft [24].

Ironically, the growing application of these new materials in primary structures has not triggered an equivalent evolution in joining technologies. Mechanical joining methods, developed for metals which are ductile and isotropic, are still the State-of-the-Art despite the problems arising when being used in anisotropic materials such as FRP or Fibre Metal Laminate (FML). Adhesive bonding has shown to be a great, innovative alternative in this application for metals and especially for FRP or FML materials.

The Benefits and Challenges of Bonded Primary Structures

Bonding has several benefits compared to the use of mechanical fasteners in structural joints. For example: discrete loads transfer is eliminated which improves the fatigue performance and allows for thinner, more compact and thus lighter joints. Also, drilling fastener holes is not required which in FRP and FML materials is a resource expensive and potentially base material damaging process. Furthermore, the unlocking of new structural, production and repair concepts could lead to improved aircraft designs and maintenance programs.

The main challenges for bonded joints in primary structures lie with the ill understood damage tolerance characteristics and the difficulties associated with quality assurance of a bond line. Manufacturing defects and/or impact damages could grow rapidly leading to catastrophic disbonding of components. The instantaneous occurrence and rapid growth of these damage modes make them discrete in time and therefore difficult to predict and account for with reasonable inspection and maintenance programs [25]. These factors have hindered the widespread application of bonded joints in primary structures despite their potential [5].

Certification of Bonded Joints in Primary Structures

Bonded joints are generally classified into three categories: (1) co-curing, (2) co-bonding and (3) secondary bonding [5]. Secondary bonding is most difficult to certify due to the presence of two adhesive-component interfaces. However, it is the most viable method from a manufacturing and service-life point of view.

Three options are stated in the Federal Aviation Administration's (FAA) Advisory Circular AC 20-107B of 9/8/2009 to show compliance with the certification regulations for bonded joints [26]:

> *"For any bonded joint, the failure of which would result in catastrophic loss of the airplane, the limit load capacity must be substantiated by one of the following methods:*

1. *The maximum disbonds of each bonded joint consistent with the capability to withstand the loads in paragraph (a)(3) of this section must be determined by analysis, tests, or both. Disbonds of each bonded joint greater than this must be prevented by design features*
2. *Proof testing must be conducted on each production article that will apply the critical limit design load to each critical bonded joint*
3. *Repeatable and reliable non-destructive inspection techniques must be established that ensure the strength of each joint"*

Currently, and also in the near future, no suitable NDI method exists to comply with option 3. Option 2 is not practical nor economically viable for any commercial aircraft manufacturer as it requires testing of all bonded structures which is resource expensive and detrimental to manufacturing lead-time. So according to the current certification guidelines, the only practical and economically feasible option is option 1; adding Disbond Arrest Features (DAF) to disrupt adhesive damage growth.

Certification of Bonded Primary Structures by Bolted Disbond Arrest Features

The European project Boltless Assembling of Primary Aerospace Composite Structures (BOPACS) started in 2012 to investigate several concepts for DAFs. It was concluded that lockbolts are capable of arresting disbond growth under fatigue loading in bonded Carbon Fibre Reinforced Polymers (CFRP) joints [3, 5]. More recently, a joint research program by Boeing, Washington University and the Federal Aviation Authorities (FAA) was published demonstrating the arrest of quasi static disbond growth by bolted DAFs in bonded CFRP specimens [2]. Continuing on the success of BOPACS, Hanx [7] performed an initial study to assess the arresting capabilities of bolted DAFs in bonded FML joints. A significant reduction of the Disbond Growth Rate (DGR) was observed, but the arresting effect was perceived only briefly before disbond growth started to accelerate again. It was hypothesized by [7] that the initiation and growth of adherend fatigue damages lead to the demise of the arresting capabilities of the bolted DAFs.

These bolted DAFs may be applied by a assuming certain likely hood of bond line damage events [25] and their capability to arrest disbond growth. By doing so, the damage tolerance characteristics of bonded joints can potentially be guaranteed whilst drastically reducing the number of fasteners that are currently required.

From the above the potential of bolted DAFs becomes clear coupled with the interest in its development by both the industrial and academic society. However, the current understanding of the mechanisms responsible for achieving the arrest of disbond growth is very limited. Moreover, the unfavourable interaction between the arrest of disbond growth and adherend fatigue damages in bonded FML joints has never been investigated.

The Research Goal and Structure of this Report

This research aims to to deepen today's understanding of the potential and weaknesses of bolts as DAFs in bonded FML joints. This is achieved by experimental fatigue testing and model simulations of coupon specimens with different DAF configurations. The model simulations are performed using a self developed quasi analytical and a Finite Element Method (FEM) model.

The research presented in this report is structured according to the following chapters. In chapter 2 the available literature on bolted DAFs in bonded joints is reviewed. This review will be used in chapter 3 to formulate the project plan; problem statement, research objective and hypotheses and the envisioned output. The solution methodology is given in chapter 4 which thoroughly covers the experimental fatigue test set-up, the FEM model and the quasi analytical model. The results of the fatigue test campaign and the verification of both models are discussed in chapter 5. The analysis using the FEM model, the experimental results and the quasi analytical model are discussed in chapter 6, chapter 7 and chapter 8 respectively. The conclusions of the research are presented in chapter 9 together with the limitations of the current research accompanied by recommendations for future work.

2

Literature Review

The use of Disbond Arrest Features (DAF) in bonded joints is considered beyond the State-of-the-Art and research has mainly focused on Carbon Fibre Reinforced Polymers (CFRP) and Fibre Metal Laminate (FML) bonded joints. Although limited in volume, the existing research has shown promising results that stimulate the need to continue the investigation of the mechanisms responsible for the arrest of disbond growth and how the design of these features should be performed.

This chapter summarizes an exhaustive literature review that was performed to capture the available knowledge on DAFs with a focus on the use of bolts as DAFs. Additionally, other topics have been reviewed that are relevant to this research; fatigue in bonded FMLs and experimental fatigue testing methods. By synthesizing the literature review, knowledge gaps are identified which are used to formulate concrete research objectives, questions and the envisioned research output; all detailed in chapter 3.

2.1. Disbond Arrest Features

The desired function of DAF is to reduce the driving force for damage growth so that a required damage tolerance can safely be guaranteed. In the case of a bonded joint, this driving force is typically discussed in terms of the energy released upon the formation of a new fracture surface known as the Strain Energy Release Rate (SERR) denoted by G. The SERR is typically calculated for given states using Linear Elastic Fracture Mechanics (LEFM) which assumes the material to be in the linear elastic range. The SERR can be split into three different components defined by the loading (or crack opening) modes: Mode I (G_I), Mode II (G_{II}) and Mode III (G_{III}) as depicted in fig. 2.1. The behaviour of a given material or adhesive can then be characterized in terms of its resistance to growth based on this driving force parameter.

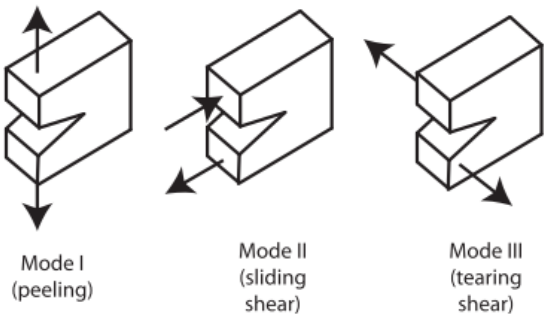

Figure 2.1: Crack tip loading modes (from Bürger [8]).

A DAF is simply a design feature which reduces the SERR by restricting the deformation of the joined parts that is caused by an incremental growth of fracture surface. Thus, a DAF influences disbond

growth by restricting the Mode I, Mode II, and/or Mode III opening of a disbond. Numerous types of DAFs exist such as: bond-line toughening (i.e. toughened adhesives or particle integration), trough-the-thickness reinforcements (i.e. stitching, tufting or z-pins) or geometric modifications (i.e. enhancing fibre bridging) which are described very well in the literature review of Hanx [7]. This research however, only focuses on the application of a bolt as DAF.

Considering a simple bolt passing through a bondline as illustrated in fig. 2.2, several ways can be considered in which the bolt can arrest a disbond [2, 3, 6]. First, Mode I can be suppressed by the bolt clamping force and due to the bolt rotation under joint loading, causing a localized clamping behaviour underneath the fastener head. Secondly, the bolt can provide a secondary load path once the disbond passes the bolt location. This secondary load path reduces bondline loads, primarily in the form of shear, effectively reducing Mode II. Thirdly, friction between the disbonded regions of the adherends can also occur as a result of the clamping force provided by the bolt. This friction also provides an alternative load path that reduces the shear load transfer, and thus Mode II, of the bondline.

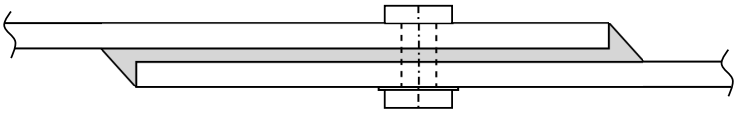

Figure 2.2: Illustrative example of a bonded joint with a bolted DAF.

Combining mechanical fasteners and adhesive bonding is already often done in so called bonded-bolted hybrid joints to reduce peel stresses near the bond-line edges or for fail-safe purposes. The latter requires the mechanical fasteners to carry design ultimate-load in case of (partial) bond-line failure and is frequently referred to as using chicken rivets. For the purpose of DAFs however, mechanical fasteners only obstruct the adhesive disbond growth and do not contribute to the joint load carrying capability.

2.2. Effectiveness of Bolts as Disbond Arrest Features

The previous section has introduced the bolted DAF and the mechanisms through which it can reduced the Mode I, Mode II and Mode III SERR components. The effectiveness of a bolt as DAF in arresting disbond growth is depended on two factors. First is the impact on the DGR of the three SERR components when they are reduced in size and second is the the ability of a bolt to provide the reduction of the SERR components. These two questions lie at the foundation of the research published in the literature.

Three research groups have been identified as the sole contributors to the published work regarding the effectiveness of bolted DAFs in bonded joints: (1) Washington University in cooperation with the Boeing Company and the Federal Aviation Authorities (FAA) [2, 6, 27–38], (2) the European research project Boltless Assembling of Primary Aerospace Composite Structures (BOPACS) [3–5] and (3) Delft University of Technology (TUDelft) [7]. Their work has been summarized in table 2.1 and can be grouped into two categories defined by the materials used for the adherends: CFRP and FML.

2.2.1. Carbon Fiber Reinforced Polymer adherends

Washington University has mainly investigated the arresting behavior of a single and double fasteners placed in bonded CFRP joints under quasi static Mode I, Mode II and Mixed Mode (MM) loading [2, 28, 31, 32]. The arresting behavior under fatigue loading has only been covered to a limited extent by Richard [6]. An excellent and exhaustive overview of the quasi static loading research has recently been published [2] so only the most relevant information will be stated here.

2D Finite Element Analysis (FEA) was used in conjunction with a probabilistic approach to demonstrate the reliability of a single mechanical faster acting as DAF in bonded CFRP joints under quasi static Mode I and MM oading [39]. Next, a Mode II test [29], a MM test [30, 32], 2D FEM models [27, 28, 31, 32] and analytical models [28, 32] have been developed for single fastener research. It was learned that a single fastener did not fully arrest disbond growth under quasi static loading. Therefore, research continued with two fasteners placed in series under both quasi static loading and fatigue loading at

Table 2.1: Overview of the existing literature on bolted DAFs (note: (+/-) signs for the labels static and fatigue indicate the direction of loading where (+) is tensile and (-) is compressive).

Research group	Washington University							BOPACS			TUDelft
Year	2009	2012	2012	2013	2016	2017	2018	2015	2015	2017	2017
Main work	[39]	[27]	[28]	[31]	[32]	[6]	[2]	[3]	[4]	[5]	[7]
Related work			[29]		[30]	[33–38]	[6, 28, 31, 32]			[7]	
Specimen geometry and material											
adherend	CFRP	CFRP	CFRP	CFRP	CFRP	CFRP	CFRP	CFRP	CFRP	CFRP GLARE	GLARE
Specimen type	DCB	CSL	Custom	CLS	CLS	CLS	CLS	CLS	CLS	WSLS	WSLS
Nr. fasteners	1	1	1	2	1	2	1, 2, 4	1	1	4	4
Experiment and model load cases											
Static	+	+	+	+	+	+	+	+/-			
Fatigue						+/-		+/-	+	+	+
Loading mode	G_I, $G_{I/II}$	G_I, $G_{I/II}$	G_{II}	$G_{I/II}$	G_I, $G_{I/II}$	$G_{I/II}$	G_I, $G_{I/II}$	$G_{I/II}$	$G_{I/II}$	$G_{I/II/III}$	$G_{I/II/III}$
Models developed and utilized											
FEM 1D				X		X	X				
FEM 2D	X	X	X	X	X	X	X				X
FEM 3D				X		X	X	X	X		X
Analytical			X		X	X	X				
Design space investigated											
Fast. type									X		
Fast. preload		X	X	X	X	X	X	X			
Fast. clearance		X			X	X	X	X			
Fast. size					X	X	X	X	X		
Fast. compliance			X	X	X	X	X				
Fast. spacing				X		X	X				
Friction coeff.		X		X	X	X	X				
Laminate		X	X	X	X	X	X				
Specimen width				X			X				
Pre-crack											X

50% and 75% of the test specimen's static strength [6, 31].

Several conclusions were drawn regarding the arresting mechanisms of fasteners. First of all, three arresting mechanisms were identified which are listed below from the largest to smallest effect [2]:

1. Mode I elimination by the fastener clamping load
2. Mode II reduction by crack-face friction load transfer in the direct proximity of the fastener
3. Mode II reduction by the fastener shear engagement

Secondly, despite complete Mode I elimination, sufficient mode II reduction is needed for full arrest under quasi static loading. This was only achieved when 2 fasteners were placed in series [6]. Thirdly, fatigue loading yielded similar conclusions, but crack-face friction is relatively more important since Mode II reduction by fastener shear engagement is less effective at lower applied loads [6]. The latter is supported by experimental observations where full fatigue disbond growth arrest occurred in the proximity of the second fastener without it being engaged in shear.

Based on the investigated design space, key parameters were identified [2]. Fastener preload and the friction coefficient heavily influence the Mode II reduction through crack-face friction. Also, increasing the fastener preload was found to extend the range of Mode I elimination more forward of the fastener. Initial clearance delays and decreases the arresting effect [2], especially with fatigue loading due to the lower relative displacements of the adherends [37, 38]. The joint-fastener flexibility impacts the Mode II reduction by fastener engagement and was observed to increase as a result of bolt hole damaging during loading [37, 38]. For fatigue disbond growth predictions, the adhesive fatigue threshold was required to fully capture the arresting effect [6].

The European research project BOPACS initiated in 2012 with Airbus and TUDelft amongst its partners, aiming to move away from using bolts in CFRP joints. Several DAF concepts such as bond-line toughening, corrugation, lockbolts and various z-pin configurations were evaluated based on their disbond arresting capability. Contrary to their initial goal, lockbolts were selected as they displayed the best ar-

resting performance, but also because of their easy integration into existing production infrastructures.

The influence of lockbolt size, preload and clearance fit were tested using CFRP Cracked Lap Shear (CLS) specimen with a single bolt in various configurations [3]. Tested at 22% of the static strength, the lockbolt with an axial clearance clearly performed less well whilst a radial clearance did not seem to have an influence. These observations lead to the conclusion that Mode I suppression is the main disbond arrest mechanism under fatigue loading. Their findings are in agreement with [2, 6] except that Mode II reduction bolt shear engagement and crack-face friction are not emphasized and the latter is even ignored completely.

In the final stage, fatigue tests with Wide Single Lap Shear (WSLS) specimens were performed which displayed a full arrest of damage growth after more than 3,000,000 load cycles as shown in fig. 2.4(a). Disbond growth acceleration was observed again for an additional 1,000,000 cycles until finale failure after increasing the fatigue load by 33% [3].

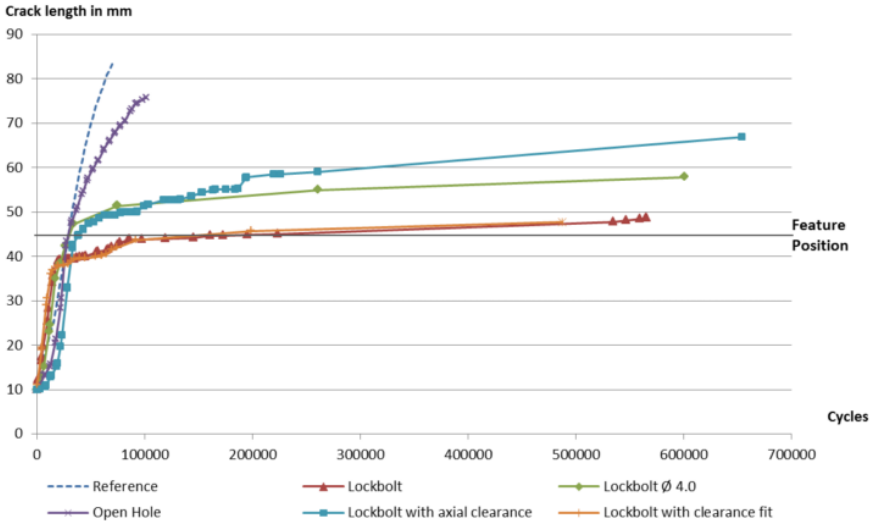

Figure 2.3: Comparison of tested bolted DAF parameters (from Kruse *et al.* [3]).

2.2.2. Fiber Metal Laminate Adherends

As a BOPACS spin-off, Hanx [7] studied the fatigue disbond growth arresting behavior of Hi-Loks in bonded WSLS specimens using a GLAss REinforced aluminum (GLARE) 2A-4/3-0.3 grade with AL2024-T3 aluminum for the adherends. Test results, shown in fig. 2.4(b), show a significant reduction in DGR, but the arrest of the disbond growth lasted relatively short compared to that observed in BOPACS. Furthermore, it was observed that final failure of the joint was a combination of bond line failure and adherend fatigue failure. It was hypothesized that the bolted DAF itself may actually initiate fatigue damage leading to the loss of its arresting capability. Subsequently, fatigue testing was performed with WSLS specimens with through-the-thickness pre-cracks added to the bolt holes to stimulate fatigue crack growth so that its influence on the arresting behavior could be studied. Although not conclusive, the results gave a strong indication that these fatigue cracks negatively impact the arresting capability of a bolted DAFs.

2.2.3. Developed Numerical and Analytical Models

Several numerical and analytical models have been developed by all three research groups to study bolted DAFs. 2D FEM models of the CLS specimen with a single fastener [32, 39] and two fasteners [6, 31] have been developed that simplify the fasteners as a set of springs. The fastener clearance and preload have been included through non-linear spring stiffness definitions [2]. 3D FEM models capable of predicting disbond growth [4–6, 32] or just the SERR and stress fields [7] were developed that all deploy the Virtual Crack Closure Technique (VCCT) for the calculations of the SERR components.
Analytical methods have been developed with a single fastener for quasi static Mode II [28] and MM

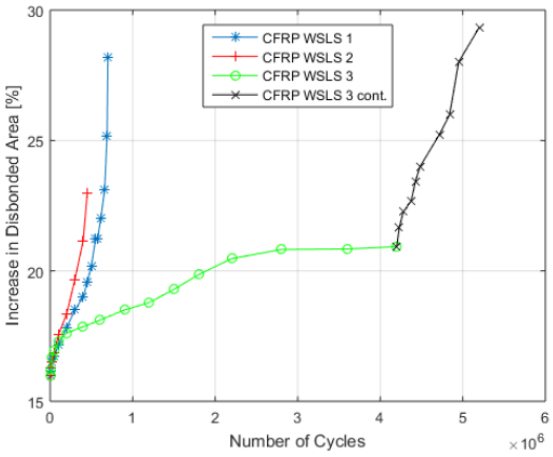

(a) CFRP adherends without (CFRP WSLS1, CFRP WSLS2) and with (CFRP WSLS 3, CFRP WSLS 3 cont.) bolted DAF (from Kruse [5]).

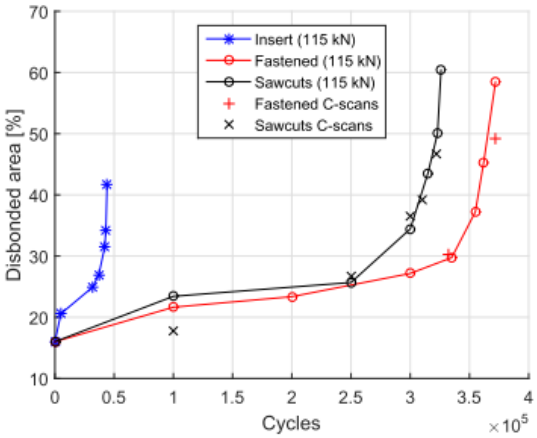

(b) FML adherends without (Insert (115 kN)) and with (bolted (115 kN), Sawcuts (115 kN)) bolted DAF (from Hanx [7]).

Figure 2.4: Comparison of fatigue disbond growth in bonded CFRP [5] and FML [7] WSLS specimens.

[32] loading. The MM method is a beam based model using the Principle Of Minimum Potential Energy combined with the Rayleigh-Ritz solving method to approximate static equilibrium and is very well documented in [32]. The only fatigue disbond growth model is a FEM base solution of truss/bar elements implemented in MATLAB and includes two fasteners placed in series [6]. Richard [6] includes the experimentally obtained adhesive fatigue threshold, laminate stiffness, bolt flexibility [37] and the fastener stiffness degrading effect due to hole damaging [38] leading to improved predictions.

2.2.4. A Critical Review: What Next?

By reviewing the State-of-the-Art in bolted DAFs four topics are highlighted: (1) the proven arresting capability of bolted DAFs in bonded CFRP joints, (2) the plausible, but unproven arresting capability of bolted DAFs in bonded FML joints (3) the limited understanding of the arresting mechanisms and (4) the relation between the arrest of disbond growth and adherend fatigue damage initiation/growth.

- Proven arrest capability in bonded CFRP joints has been achieved in both high cycle [3, 5] and low cycle [6] fatigue tests using the CLS specimen. Furthermore, WSLS specimen testing, which is a closer representation of real life conditions than the CLS specimen, has shown successful fatigue disbond growth arrest [5]. Future research is required for multi-directional loading, variable amplitude loading, R-ratio effect etc., but the arresting capability has been shown

- Plausible arrest capability in bonded FML joints has been observed by reduction of the DGR, but the effect lasted only for a limited number of load cycles. Fatigue crack initiation in the aluminum face sheet is hypothesized as the root cause for the rapid elimination of the arresting effect [7], but this has not been conclusive. Also, the role of adherend delamination is not well understood

- The Status-Quo is not aligned on the bolted DAF arresting mechanisms. It is agreed that Mode I suppression is the main crack arrest driver [2, 5, 6], but the importance of Mode II reduction by fastener shear engagement and crack-face friction is only emphasized by [2, 6] and the latter is ignored by [3–5] . Furthermore, [6] concludes that two fasteners in series are required for full fatigue disbond growth arrest which is contradicted by [3, 5]. However, this conflict seems to be related to the applied load magnitude, which was 50-75% and 20% of the maximum static load for [6] and [3] respectively

- All studies try to understand the arresting mechanism by changing bolt parameters and experimentally or numerically observing the change in disbond growth. This approach will expand on the bolt itself, but it is unlikely to enable a fundamental understanding of the arresting mechanisms in bonded joints. To given an example: strictly speaking Mode I cannot yet be regarded

as the main driver for arrest since its effect has never been tested in isolation; only using a bolt which affects both Mode I and Mode II. An alternative approach would be the other way around: understanding what conditions are required for arrest in general and using that knowledge to design DAF concepts

- The interdependence of disbond growth, arresting behavior and adherend damage initiation/growth has not been researched nor is it well understood. However, the FML program has shown that, through a yet unknown mechanism, adherend damage can have a detrimental effect on the arresting behavior of the fasteners. Future research into the unknown relation between arresting behavior and adherend damage initiation/growth is crucial to justify a damage tolerant bonded joint design using bolted DAFs

2.3. Fatigue in Bonded Fiber Metal Laminates

Based on the literature review in bolted DAFs, it is apparent that the application of such features in bonded FML joints is complicated by the fatigue behavior of the FML adherends. As a result, a critical review of this process is necessary for this investigation.

Fatigue damage in a bonded joint can occur in (1) the adhesive (cohesive or adhesive) or (2) in the adherend. In FML adherends, fatigue damage can occur as a fatigue crack, most likely in one of the aluminum plies, and/or as a delamination growing between the metal and adjacent GFRP plies [40]. Results of Hanx [7] have shown that the initiation of aluminum fatigue cracks might reverse the arresting capability of bolted DAFs. To make a sound model, adhesive disbond growth and aluminum fatigue crack initiation must be covered. Fatigue crack growth, delamination initiation and growth play a role as well, but are outside the modeling scope; they will be discussed but models will not be reviewed.

2.3.1. Introduction to Fiber Metal Laminates

Fibre Metal Laminate (FML)s have been developed to answer the need for a more damage tolerant material [41] resulting in composite material using a combination of metallic and fibre reinforced polymer layers. Beneficial characteristics are combined of both materials; the isotropic behaviour, high bearing strength, high impact resistance and good repair-ability from metals and the excellent fatigue properties, high strength and stiffness from fibre reinforced polymers. Especially in fatigue, fracture toughness, impact corrosion and fire resistance, significant improvements are observed compared to monolithic constitutive [42].

Various commercially available types of FMLs exist such as GLAss REinforced aluminum (GLARE), Aramide Reinforced ALuminium Laminate (Arall) and CArbon Reinforced ALuminium Laminate (CARALL). Because this research is a continuation of Hanx [7], GLARE was selected for the type of FML. Six generic GLARE grades have been defined for certification in order to limit the vast amount of laminate lay up possibilities. An overview of these GLARE grades can be found in [41], but important to mention is the coding of the standard GLARE grades as it will be used throughout this report. To give an example: GLARE 4B-4/3-0.4, which means GLARE type 4, subclass B, with 4 metallic layers and 3 Glass Fibre Reinforced Polymers (GFRP) layers, where the aluminum layers are 0.4 mm thick. The standard thickness per GFRP layer is 0.133 mm and holds no further specification [43].

2.3.2. Damage Modes and their Interactions

Similar to the tests performed by Hanx [7], more examples can be found in the literature where the existence and interaction of failure modes has been observed in bonded FML joints.

Beumler [44] fatigue tested GLARE skins repaired with a bonded elliptical GLARE patch. Delamination growth initiated and propagated between the aluminum face sheet and the adjacent glass fiber prepreg of the repaired skin. The delamination originated from fatigue cracks that had initiated and linked up in the aluminum face sheet of the repaired skin around the edge of the bonded repair patch.

Pascoe [45] developed a model to predict delamination growth in the adhesive interface of bonded patch repairs and performed fatigue tests for model input and validation. Specimens with an aluminum

patch bonded to a GLARE skin showed fatigue crack initiation in the GLARE aluminum face sheet followed by a growing delamination between the aluminum face sheet and adjacent fibre prepreg. In one case this delamination overtakes the delamination in the adhesive skin-patch interface similarly as observed in Beumler [44].

Interestingly, fatigue testing two other specimens with aluminum adherends, fatigue cracks were initiated in the proximity of the front of an artificial delamination in the skin-patch adhesive interface [45]. The fatigue crack initiated well before any disbond growth occurred so it seems that a stationary disbond front can act as a local stress raiser leading to early adherend fatigue initiation:

"*As it appears delaminations can initiate fatigue cracking in the adherends, a greater understanding of the interactions between bond-line damage and adherend damage is needed.*"

—J.A. Pascoe, Delamination of Bonded Repairs [45]

What [45] had observed was the effect of the peak stresses in the adherend of a bonded joint adjacent to the disbond front that result from (1) the applied tensile load, (2) secondary bending and (3) a stress concentration caused by the stiffness step at the overlap edge [46, 47]. The severity of these three components combined is maximum in the around the overlap edge, or disbond front, as shown in fig. 2.5.

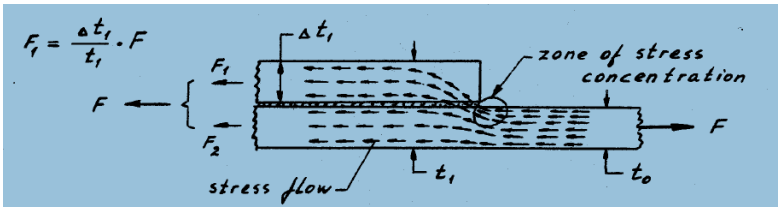

Figure 2.5: adherend stress concentration in bonded joints (from Poulis [9]).

2.3.3. Adherend Fatigue Initiation (and Growth)

Fatigue behavior of FMLs is characterized by the crack growth phase which is a large portion of the total fatigue life where it is negligible in monolithic metals. After a crack has initiated in a metal ply, the adjacent fibres are likely to be intact due to their higher fatigue resistance, which lets the metal ply stresses bypass the fatigue crack. This is called *fibre bridging* and significantly slows down the metal FCG.

On the other hand, the fatigue initiation life is reduced by residual tensile stresses in the aluminum layers resulting from the different Coefficient of Thermal Expansion (CTE) of both materials when cooled down from curing [48, 49]. Post-stretching can be applied where the metallic plies are stretched until plasticity. At the same time, the fibres remain elastic which results in lower, or even reversed, thermal residual stresses in the metallic layers after the process is finished [48].

In monolithic metals, S-N curves, which give the number of cycles up to failure, can be used to predict the number of cycles to fatigue crack initiation as the crack growth phase can be neglected. In FMLs however, the crack growth contribution to the total life cannot be neglected. To avoid the expensive program of replicating the existing monolithic metal S-N curves for FML applications, a crack length of 1 mm was defined as the end of the crack initiation phase in FMLs. With this definition, monolithic metal S-N curves can be used directly without the need for corrections [48, 49].

Spronk *et al.* [49] published an excellent step-by-step methodology to predict the number of load cycles to fatigue crack initiation in notched FMLs using monolithic metal fatigue data. The method background is explained to an even greater extent in [48]. Due to the quality and completeness of the article, the method will not be elaborated here and the reader is referred to [49] or [48].

Inter delamination can initiate and grow when fiber bridging occurs as the shear stresses between both plies increase leading to a delamination [48]. This delamination area takes the shape of an ellipse and grows simultaneously with the metal fatigue crack [48]. This effect has also been observed during fatigue testing of bolted DAFs in bonded FMLs Hanx [7] and during fatigue testing of regular bonded FMLs [44, 50]. Due to the lower growth resistance of a GFRP pre-preg layer, an initiated delamination could overtake an arrested adhesive disbond and become the new critical damage interface. Prediction of a delamination in GLARE can done using the proposed analytical model by [19].

2.3.4. Adhesive Disbond Growth

Pascoe *et al.* [51] created an exhaustive review of the adhesive damage growth models and identified four categories: (1) Cohesive Zone Model (CZM), (2) Fracture Mechanics (FM), (3) Extended Finite Element Method (XFEM) and (4) stress/strain based models. CZM and XFEM are FEM based solutions and not of interest to this research as it focuses on a (quasi) analytical approach. Furthermore, stress/strain based methods are well suited for static delamination problems, such as predicting the fatigue life, but not for damage growth problems [1, 51]. FM based methods are preferred for predicting damage growth [1, 51] and they can easily be implemented in a (quasi) analytical solution. FM methods relate damage growth rate in a material to a fracture parameter such as the Stress Intensity Factor (SIF) in metals or the Strain Energy Release Rate (SERR) in composite/adhesive interfaces.

The SIF quantifies the magnitude of the stress field ahead of the crack tip and is widely used in homogeneous materials such as metals to predict the crack growth rate [52] through the Paris-Law [53]:

$$\frac{da}{dN} = C_c \Delta K^{n_c} \tag{2.1}$$

where $\frac{da}{dN}$ is the crack length incremental increase per load cycle, C_c and n_c are curve fitting parameters and ΔK is the the applied SIF range $K_{max} - K_{min}$. It is important to emphasize that the C and n are simple curve fitting parameters which hold no physical meaning and that the Paris-Law is merely an empirical relation [54].

For composite/adhesive interfaces, the SERR is preferred for damage growth as the SIF calculations become very complex [51, 54]. The SERR equals the total amount of elastic energy made available for the adhesive per unit crack surface area increase. In Linear Elastic Fracture Mechanics (LEFM), the material is assumed linear elastic so no energy is dissipated to e.g. plasticity. Similar to the SIF, the SERR is used in a Paris-Law type of relation to describe damage growth rate:

$$\frac{db}{dN} = C\,[f(G)]^n \tag{2.2}$$

where $\frac{db}{dN}$ is the delamination length incremental increase per load cycle, C and n are curve fitting parameters. The literature deploys various forms of $f(G)$ such as G_{max} or (2) $\Delta G = G_{max} - G_{min}$, but these contain potential pitfalls according to Rans *et al.* [54]. G_{max} cannot describe a complete load cycle as it only holds monotonic information. Furthermore, ΔG is used in a way analogous to ΔK, but ΔG depends on both the cyclic and mean load component where ΔK depends on the cyclic load component only [54]. Not recognizing the additional mean load dependency has lead to fictitious or distorted observations in crack growth data [54]. Therefore, [54] a more robust similitude parameter is proposed by [54] which eliminates the mean load dependence:

$$\left(\Delta\sqrt{G}\right)^2 = \left[\sqrt{G_{max}} - \sqrt{G_{min}}\right]^2 \tag{2.3}$$

It important not to forget that similitude parameters used in FM, despite their usefulness to growth predictions, are selected purely on the basis of their empirical consistency without holding any physical justification [50]. It must be mentioned that [54] never argues $\left(\Delta\sqrt{G}\right)^2$ as a crack driving force, but solely as a justified similitude parameter.

Damage growth typically occurs in a bonded mode by a combination of both Mode I and Mode II loading whose mixture is defined by the Mode Ratio (MR): $MR = G_I/G$ where G_I and G are the Mode I and total SERR components. A model that can predict the disbond growth of a bonded joint with a DAF must therefore be capable of accounting for this Mixed Mode (MM) growth behavior.

Mixed-Mode Disbond Growth Models

Existing LEFM based MM models have been reviewed extensively by [8, 51, 55]. Generally, MM damage growth models use the Paris-Law and try to relate the C and n coefficients to the MR. It was shown by Blanco *et al.* [55] that the models [56–62] have a monotonic relation between the Paris-Law coefficients and the MR, but that a non-monotonic relation can exist. A non-monotonic relation was proposed by [55] which is now the most widely used model together with [61].

Later, Bürger [8] reviewed [55] and later models [63–66] and observed a complete lack of physical foundation. Only [66] includes a physical damage parameter, but this is just for $MR > 50\%$. Bürger [8] criticizes [55, 61] for ignoring that the Paris-Law coefficients, used to argue accuracy of their model, are highly sensitive to the curve fitting methodology used and the scatter in the crack growth data. Furthermore, Bürger [8] notes that [55, 61] validate their models with more more MR data points than the minimum required leaving their accuracy across various crack growth data having less Mode Ratio data points questionable.

Indeed, [8] obtained unconservative results using the model of [55] and the linear superposition model of [57] gave inaccurate results indicating that an interaction between Mode I and Mode II exists. Triggered by the apperent lack of physical foundation in the Status-Quo, Bürger [8] analyzed adhesive MM fracture surfaces and identified the adhesive principle stress as the crack driving force. His new model incorporates the adhesive stresses for the fracture parameter and only pure Mode I and Mode II crack growth data is required as input. Compared to experimental results, the predicted rate shows an excellent fit at MR = 25% and 50%, but the predictions are conservative for MR = 75%.

After the work of [8], a model was proposed by [67] based on earlier work [68, 69] by adopting the well known Hartman-Schijve equation from metal crack propagation. Disbond growth data showed to collapse for various R-ratios, MRs and temperatures, but the relation is purely empirical and has no physical foundation. The author therefore considers the model proposed by [8] as the State-of-the-Art in LEFM based MM damage growth models as it is the only attempt to provide a full physical foundation.

Another important observation is that not a single model was found that simultaneously models the damage growth in the adhesive and in the adherend [1, 70]. Studying the interdependence between disbond growth, disbond growth arrest by a bolted DAF and fatigue crack initiation/growth in a bonded FML will need the development of a novel model.

2.4. Relevant Experimental Methods

The application of DAFs in practice requires considerations for the design of the bonded joint, loads to be transferred, and specific boundary conditions in order to truly assess the arresting potential of the feature. For studying the general behavior of a DAF, however, a more simplified and controllable representation of a bonded joint is desirable; a so-called coupon test. The Cracked Lap Shear (CLS) specimen was independently identified in an extensive study by both BOPACS and the Washington University as the leading specimen configuration to study DAF behavior. The extensive and successful application of the CLS specimen has lead to the early decision to adopt the specimen for this research.

Experimental evaluation of a DAF requires Non Destructive Inspection (NDI) methods to obtain information about the damage progression so that the influence of a DAF can be quantified. For this purpose, NDI methods exist such as ultrasonic testing, embedded strain measurements which are reviewed in [7]. Recently, Digital Image Correlation (DIC) has been used as an in-situ measuring technique to find the disbond front based on gradients in the measured strain fields in the adherend by [7, 45].

Both the CLS specimen and the DIC inspection technique will be briefly covered here.

2.4.1. The Cracked Lap Shear Specimen

The CLS specimen, depicted in fig. 2.6, was used by [2, 6] and [5] to test the MM arresting behavior of bolted DAFs. The CLS was selected for its geometry and MR which are similar to bonded aircraft joints. In addition, multiple bolts can easily be installed and the disbond growth testing region can increased by simply increasing the specimen length. Most interesting however, is that the Disbond Growth Rate (DGR) is constant along a major portion of the overlap length [10, 15, 71] which is a perfect reference for evaluating the disbond growth behavior of a DAF.

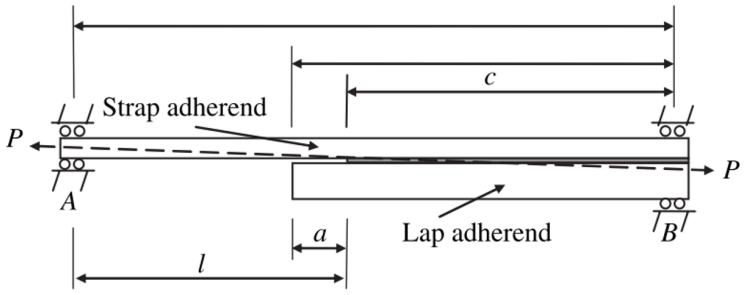

Figure 2.6: The Cracked Lap Shear (CLS) (from Da Silva and Öchsner [10]).

The CLS specimen was developed by Brussat *et al.* [71] who found that the total SERR is independent of the crack length for an infinitely long specimen. The geometric non-linear behavior of the CLS specimen must be included in the analysis to correctly predict the constant SERR distribution [10, 15, 71–73]. Over the years, the CLS specimen has been used to investigate disbond growth [72, 74] and for determining the critical adhesive fracture parameters [75, 76].

Lai *et al.* [73] published an article to assist the design of a CLS specimen by giving closed-form solutions for the SERR with various support boundary conditions. It is shown that clamped-clamped boundary conditions provide the most constant SERR over crack length. Also, it is warned that pinned supports can behave as clamped supports when bending moments can not overcome the pinned friction load leading to test result discrepancies [72].

An aggregated overview of the closed-form solutions for the CLS specimen was created during the literature review which is summarized in appendix B. Calculations of the CLS adhesive stresses [12, 13, 16] directly copy the solutions of the Single Lap Joint (SLJ) are only valid for a CLS specimen with roller-roller support boundary conditions [10]. Closed-form SERR solutions exist for a CLS specimen with non-identical adherend [16, 73, 77] and identical adherends [14, 71, 73] which give bad and good results respectively compared to [15].

2.4.2. The Digital Image Correlation Technique

The DIC technique uses a two camera set-up to track the 3D deformation of a given surface which can be used to calculate the strain field. These deformations are found by taking images of the surface which has been coated with a black and white speckle pattern. These speckle patterns are used by a commercial software package Vic3D to find the deformation relative to the surface of the previous image.

This technique has been used by Pascoe [45] and Hanx [7] to find the disbond front assuming that a gradient exists in the strain field of the surface of one of the adherends that corresponds to the disbond front location. Although effective, the accuracy was found to be become low with increasing adherent thicknesses [45]. Also, both [45] and [7] use a simple thresholding rule to determine the area of the strain field that corresponds to the disbonded region. It is expected by the author that leveraging knowledge of the strain field gained by modeling could be used to create a smarter and more effective algorithm to find the disbonded region.

3

Project Plan

By reviewing the relevant literature, the State-of-the-Art and Status-Quo in the application of bolted Disbond Arrest Features (DAF) to arrest disbond growth in bonded Carbon Fibre Reinforced Polymers (CFRP) and Fibre Metal Laminate (FML) joints have been formulated. Only bonded FML joints are considered for this research as it is a continuation of the work of Hanx [7].

This chapter details the problem statement, research objective, questions and hypotheses and the envisioned output of this research all of which were created based on the literature review. Additionally, a list of definitions is presented that are important for the correct interpretation of this report. One must realize that the project plan was not created in a single moment but rather through a dynamic and iterative process for the duration of writing this research.

3.1. Problem Statement

The problem statement will formulated considering a potential design paradox and a scientific and industrial perspective based on the literature review findings. The problem statement is detailed as;

- **A potential design paradox:** the potential design paradox is that the arrest of disbond growth in a bonded FML joint might lead to the initiation of fatigue cracks in the aluminum plies which in their turn could re-start the growth of the disbond;
  - First, [7] saw that the fatigue life prolongation in bonded FMLs by bolted DAFs was very brief and attributed the quick demise of the arresting capabilities to the initiation of fatigue cracks in the aluminum plies. Second, it was observed that a stationary disbond front can initiate fatigue cracks in the adjacent metal [45] or FML [44] adherends. If both observations are true, arresting a disbond front could initiate the same fatigue cracks that lead to the demise of the arresting capabilities of a DAF
- **Industrial perspective**: the industrial problem is the need for the currently non existent adhesively bonded, primary structural joint that can be certified in an economically viable way;
  - Especially in CFRPs and FMLs, bonding offers an improved performance over mechanically fastening, by removing discrete loads, reducing weight and production cost and by eliminating the need for drilling holes which can damage the adherend material
  - The application of bonded joints is hindered by a lack of confidence resulting from a limited understanding of their damage tolerance behaviour and the difficulties associated with assuring the quality of a bond line after production and during service-life
  - DAFs seem to provide the most realistic and economically feasible option to show compliance with the certification regulations for bonded primary structures in the near future. However, this technology is beyond the State-of-the-Art and the fundamental knowledge required for implementation is lacking

- **Scientific perspective**: the scientific problem is the challenge to understand the arresting mechanisms of bolted DAFs in bonded FML joints and how they interact with adherend damage modes. Evaluating the behavior of bolted DAFs in a bonded FML joint is particularly challenging because;
  - The arresting mechanisms of bolted DAFs in bonded joints is beyond the State-of-the-Art and research has mainly been empirical by looking at the influence of individual bolt characteristics. This poses a problem as fundamental knowledge is lacking and blind spots potentially exist in the domain of influential parameters other than bolt characteristics; if they exist.
  - The novelty of bolted DAFs in bonded joints implies that there are no readily available and accepted scientific approaches to investigate and quantify their arresting behavior. This poses a major complexity as both the relevant questions and the methodologies required to provide the answers are unknown
  - Identifying and isolating individual damage mechanisms and their interactions is very complex due to the non-linear nature of bonded joint behavior and the countless possible combinations of damage modes and interactions. However, the potential weakness in the arresting capability of a DAF caused by an interaction between the adhesive and adherend damage modes implies that this complex analysis is an inherent part of the research
  - A novel model will have to be developed as currently no bonded joint design methods exist that consider the damage growth in the adhesive and the adherend simultaneously. The lack of existence of these models is often attributed to the increased complexity that arises with the inclusion of multiple damage modes and their interaction [1]

Summarized, a design paradox potentially exists because an arrested disbond might initiate fatigue cracks that could re-start and accelerate disbond growth. From an industrial perspective there is a need to certify bonded joints using economically viable methods and bolted DAFs are a promising option. From a scientific perspective, there is a challenge to understand and evaluate the arresting capability of bolted DAFs in bonded FML joints and how it interacts with adherend damage modes.

3.2. Research Objective, Questions and Hypotheses

The literature review has been used to formulate the problem statement detailed in section 3.1 which will now be used to define the research objective. The research objective is;

To establish the disbond growth arresting potential and possible weaknesses of bolted Disbond Arrest Features (DAF) in bonded Fibre Metal Laminate (FML) joints by model simulations and experimental assessment of the arresting mechanisms and their relation to adherend fatigue damage modes.

The research objective can be dissected into two sub objectives for both of which a set of questions has been created all accompanied by a hypothesis to achieve manageable workflows;

- **Sub-objective 1**: Establish the disbond growth arresting potential of bolted DAFs in bonded FML joints;
  1. What are the conditions necessary to achieve an arrest of disbond growth?
     - Hypothesis 1: Reduction of the Mode I SERR is the main driving force for arrest
     - Hypothesis 2: Reduction of the Mode II SERR is required at elevated loads
  2. What conditions are provided by bolted DAFs to achieve an arrest of disbond growth?
     - Hypothesis 3: Mode I is only suppressed very locally around the fastener head therefore increasing the dependence on the reduction of Mode II
- **Sub-objective 2**: Establish the potential weaknesses of bolted DAFs in bonded FML joints;
  1. What is the effect of adherend fatigue damage modes on the arrested disbond growth?
     - Hypothesis 4: Fatigue crack initiation in the aluminum plies will re-start and accelerate the growth of an arrested disbond

2. Can an arrested disbond front initiate fatigue cracks in the aluminum plies of a bonded FML?
   - Hypothesis 5: A disbond front can already initiate fatigue cracks in the adjacent aluminum plies during slow disbond growth

3.3. The Envisioned Research Output

With the research objective and hypotheses known, the envisioned output of the research was created to act as a guidance for the initial development stages of the solution methodology.

Two outputs are envisioned that together encapsulate the hypotheses and thus the output of this research: the disbond growth and Disbond Growth Rate (DGR) in a FML CLS specimen with a DAF as illustrated in fig. 3.1(a) and fig. 3.1(b) respectively. Both outputs are briefly discussed here to provide the reader with a visual introduction to the framework of this research. A more detailed description is given in appendix A.

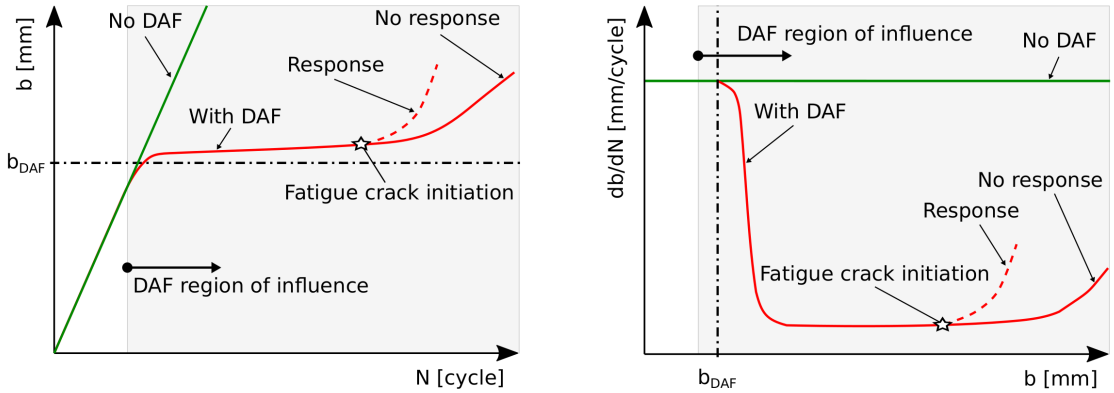

(a) Output 1: Disbond growth.

(b) Output 2: Disbond Growth Rate (DGR).

Figure 3.1: Envisioned output based on a FML CLS specimen with a DAF.

Output 1 Disbond growth in a FML CLS specimen with a DAF and adherend fatigue damage initiation

- The 1D disbond growth in a FML CLS specimen with and without a DAF is visualized in fig. 3.1(a) by plotting the disbond length b versus the number of load cycles N. The DAF is positioned at b_{DAF}. The constant DGR of a CLS specimen without a DAF allows for the evaluation of the arresting capability of a DAF. By mapping the moment of adherend fatigue damage initiation onto the results, it can be studied if it leads to the re-start and/or acceleration of the arrested disbond growth

Output 2 DGR in a FML CLS specimen with a DAF and adherend fatigue damage initiation

- The 1D DGR in a FML CLS specimen with and without a DAF is visualized in fig. 3.1(b) by plotting the DGR db/dN versus the disbond length b with respect to the DAF position; so $b_{DAF} = 0$. The disbond length is centered around the DAF so that the results of different DAF positions can be aggregated. The DGR is an important output because it represents a more direct measure of the effect of a DAF compared to the disbond length

Both figures here represent the arresting behavior in 1D, but in reality the behavior should be represented in 2D as the disbond front grows around the DAF. Therefore, similar figures will have to be created using the disbond area combined with some sort of description of the disbond shape. This will be further discussed in section 4.1.

3.4. Important Definitions

The following definitions are applied in this report unless stated otherwise;

- **Disbond**: refers to a damage in the bond line interface resulting in a local separation of the bonded adherends
- **Delamination**: refers to a damage in between two adjacent plies of the FML adherend resulting in a local separation
- **Crack**: refers to a fatigue damage in the aluminum ply of the FML adherend
- **Disbond growth arrest**: refers to the complete arrest of disbond growth; the DGR is reduced to zero
- **Disbond growth retardation**: refers to the slowing down of disbond growth; the DGR is not reduced to zero

4

Methodology

To achieve the research objective, a solution methodology has been developed which is comprised of three components. First, experimental fatigue tests using the Cracked Lap Shear (CLS) specimen have been performed to evaluate the arresting behavior of a bolt and a novel clamp as Disbond Arrest Features (DAF). These DAF configurations will be referred to as the Bolted Disbond Arrest Feature (BDAF) and the Clamped Disbond Arrest Feature (CDAF) for the remainder of this report. Second, a quasi-analytical model was created to study the disbond growth behavior with the CDAF and the relation between the Disbond Growth Rate (DGR) and fatigue crack initiation by the disbond front. Third, a Finite Element Method (FEM) model is developed to analyze the Strain Energy Release Rate (SERR) in a CLS specimen under the influence of the CDAF. This will also be used as an input for the Disbond Growth Model.

An overview of the three components and how they span across the research landscape, which is defined by the research sub objectives, is given in fig. 4.1. Figure 4.1 is a result of the development procedure of the solution methodology which is explained in more detail in appendix A. The overview is presented here to provide the reader with an introduction of the three components and how they are used throughout the research.

Objective / Method	1. Effectiveness of bolted DAFs		2. Weaknesses of bolted DAFs in bonded FMLs	
	1.1. Conditions necessary for arrest	1.2. Conditions provided by a bolt	2.1. Effect of adherent fatigue damage	2.2. Adherent fatigue initiation mechanisms
1a. CLS Experiments (Bolt DAF)		• Experimental evaluation of the arresting capability of a bolt as DAF	• Mapping of FML fatigue damage onto the disbond growth results	• Contribution of the bolt to the initiation of adherent fatigue damage
1b. CLS Experiments (Clamp DAF)	• Experimental evaluation of Mode I reduction as the main driver for arrest		• Mapping of FML fatigue damage onto the disbond growth results	• Experimental evaluation if a disbond front can initiate adherent fatigue damage
2. Disbond Growth Model (MATLAB)	• Disbond growth predictions of the Clamp DAF • Effect of Mode I and Mode II on arrest			• Model analysis of the relation between DGR and aluminum fatigue crack initiation
3. SERR Footprint Model (FEM)	**Model (2D):** • SERR analysis of the Clamp DAF	**Model (3D):** • SERR Footprint of the Bolted DAF • Note: not finished this research		

Figure 4.1: An overview of the solution methodology components and how they span across the various research topics.

4.1. Cracked Lap Shear Fatigue Experiments

Fatigue experiments have been performed using CLS specimens with different bond line materials and DAF configurations. The CLS specimen was selected as the literature review has shown that it has been successfully used in earlier studies with bolted DAFs in bonded CFRP joints [2, 5, 6]. This section further details the specimen configurations, specimen production, test setup and the data acquisition and processing methods of the performed fatigue tests.

4.1.1. Specimen Configurations

After the selection of the CLS specimen for this research, the specimen configurations have been designed. An overview of the CLS specimen configurations is given in fig. 4.2 which is segmented based on the specimen dimensions, adherend material, bond line interface, the DAF type and the DAF position.

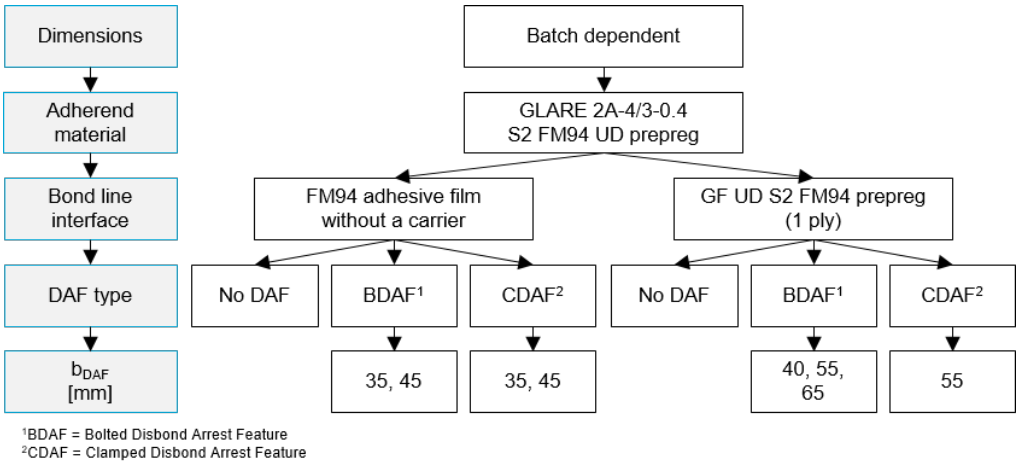

Figure 4.2: Segmentation of the CLS specimen configurations.

Dimensions

The CLS geometry is given in fig. 4.3 together with the important dimensions, assigned symbols and terminology. A bonded tab with length L_{c1} is added since the fatigue testing machine is axially aligned which would otherwise result in a bending preload due to the eccentricity of the CLS specimen [28, 30]. The edge of the bonded tab is tabered to remove stress concentrations. A saw tooth shaped Teflon foil is inserted in between the two adherends during the bonding process as an artificial disbond. The localized peak stresses at saw tooth tips provide a better and more even disbond initiation which was experienced as problematic when using a straight edge tabe during early test trials. DAFs can be placed at any position b_{DAF} with respect to the overlap edge. However, one has to take into account the boundaries of the testing range where the DGR is constant.

The dimensions are given in table 4.1 which are based on the dimensions used for the CLS specimens from BOPACS except for two adjustments. First, the width was slightly reduced so that the specimens fit in the test machine clamping fixtures. Second, the free section length was increased as it is a simple and effective method to decrease the likelihood of any influence of the boundary conditions. The dimensions differ per production batch due to manufacturing tolerances and improvements that were made to the specimen design throughout the testing program.

Table 4.1: CLS dimensions per production batch [mm].

Batch	Clamping		CLS							Teflon foil		
	L_{c1}	L_{c2}	L_{taper}	L_{AC}	L_{CB}	L_{AB}	L_{total}	W	t	b_0	b_{01}	b_{02}
2	50.14	50	14.27	67.94	144.50	212.44	312.58	43.56	2.34	20	30	20
4	59.49	50	14.35	63.37	144.59	207.96	317.44	43.56	2.35	20	30	20

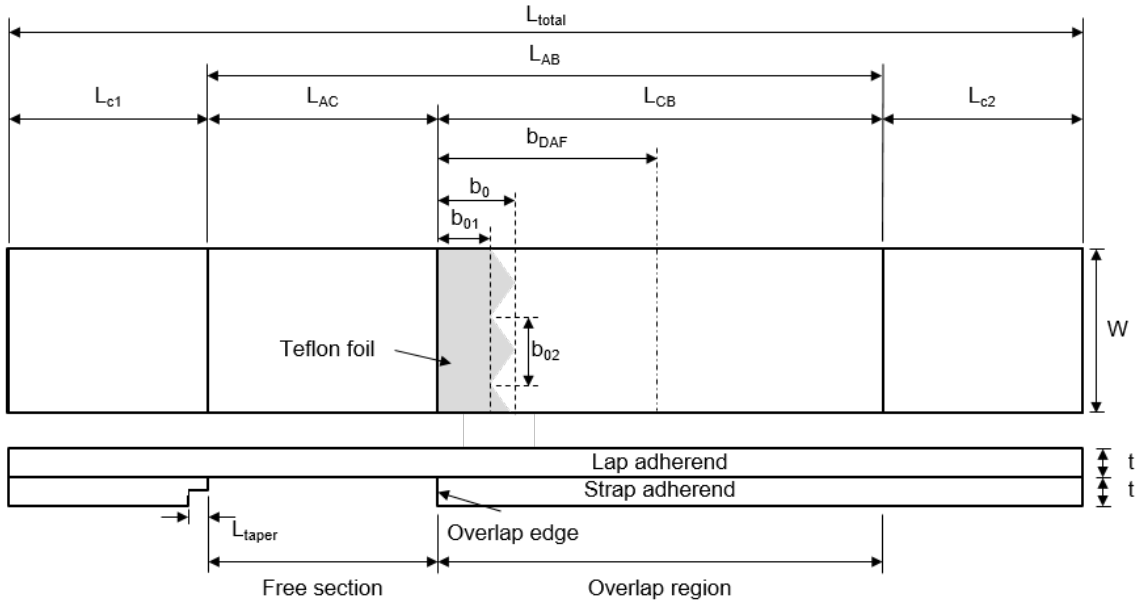

Figure 4.3: Geometric overview of the CLS specimen together with the important dimensions and terminology.

Adherend Material

All specimens are made out of GLARE 2A-4/3-0.4 with aluminum 2024-T3 metal plies and UD S2 FM94 GF prepreg plies similar to the work of Hanx [7]. Only the metal ply thickness which was increased from 0.3 to 0.4 mm to increase the allowable maximum loads for a larger Mode I and Mode II test range [14]. Similarly, only 0° plies are used for optimal strength and stiffness in the loading direction so that higher loads can be applied. The mechanical properties of Aluminum 2024-T3 and the prepreg material are given in table 4.2 and table 4.3 respectively.

Table 4.2: Mechanical properties of Aluminum 2024-T3 (directly adopted from Alderliesten [20]).

	Unit	2024-T3	
		L	LT
Young's Modulus	MPa	72400	
Strength at 4.7% strain	MPa	420	420
Tensile Yield Strength	MPa	347	299
Shear Modulus	MPa	27600	
Poisson's Ratio	-	0.33	
Thermal Expansion Coefficient	1/°C	$22{\cdot}10^{-6}$	

Table 4.3: Mechanical properties of the prepreg (directly adopted from Alderliesten [20]).

	Unit	S2-glass FM-73/BR127	
		L	LT
Thickness of single layer	mm	0.133	
Young's Modulus	MPa	48900	5500
Shear Modulus	MPa	5550	
Poisson's Ratio, v_{xy}	-	0.33	
Poisson's Ratio, v_{yx}	-	0.0371	
Thermal Expansion Coefficient	1/°C	$6.1{\cdot}10^{-6}$	$26.2{\cdot}10^{-6}$
Curing Temperature	°C	120	

Bond Line Material

Specimens were bonded using a FM94 adhesive film without a carrier with a single GF UD S2 FM94 prepreg ply. These specimens will be referred to as the adhesive and prepreg bondline specimens and the mechanical properties are given in table 4.4 and table 4.3 respectively. The resistance to disbond growth of the FM94 adhesive film requires high fatigue loads to be applied to achieve disbond growth. These loads led to plasticity and a very early onset of fatigue crack initiation in the aluminum plies during trials tests. The prepreg material has a lower resistance to disbond growth which was capitalized on to represent a 'weakened' bond line so that tests could be performed at lower loads. BOPACS encountered similar problems with the disbond jumping into the CFRP laminate and [2, 6] switched to co-cured specimens without an adhesive interface as co-bonded specimens with an adhesive interface proved to resilient too disbond growth.

Table 4.4: Mechanical properties of the FM94 adhesive film (from [21]).

	Unit	FM94 adhesive	
		L	LT
Shear Modulus	MPa	823	
Shear strength	Mpa	43.1	
Tensile strength	MPa	46.6	

Disbond Arrest Feature Type

Two different types of DAFs have been tested: the CDAF and the BDAF which are illustrated in fig. 4.4(a) and fig. 4.4(b) respectively.

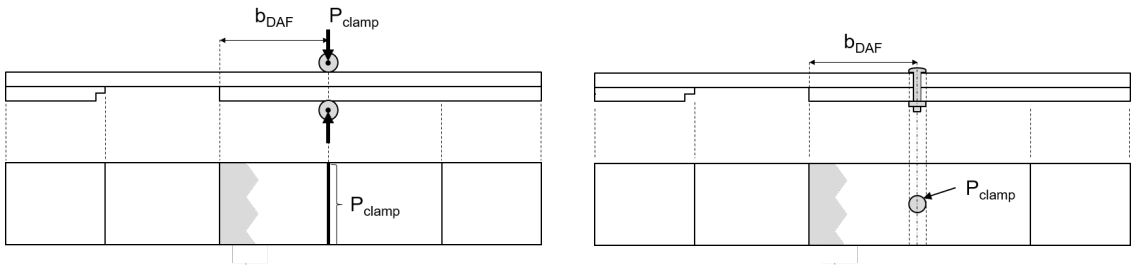

(a) Clamped Disbond Arrest Feature (CDAF) with a continuous clamping pressure application

(b) Bolted Disbond Arrest Feature (BDAF) with a discrete clamping pressure application

Figure 4.4: An illustrative example of a CLS specimen with a CDAF and a BDAF.

Bolted Disbond Arrest Feature:

- A 4.8 mm titanium Hi-Lok with an aluminum collar was selected based on the work of [7]. The spacing between the Hi-Lok and the specimen edge is greater than twice the Hi-Lok diameter which is a common design rule for the fastener spacing in GLARE [78]. However, this design rule is based on the static strength applications of the fasteners which does not apply to the current research. Only one BDAF will be used per specimen. A real life example of the CLS specimen with a BDAF is given in fig. 4.5

Clamped Disbond Arrest Feature:

- The aim of CDAF is to isolate the Mode I restriction of a BDAF and to idealize it by making it continuous across the width of the specimen. Additionally, the CDAF allows the testing of the hypothesis that a slow growing disbond front can initiate adherend fatigue damage
- The design and production was performed by hand in the machine shop of the Industrial Design Faculty. The design must satisfy the following criteria:

  1. The line of sight for the visual inspection of the disbond length may not be obstructed

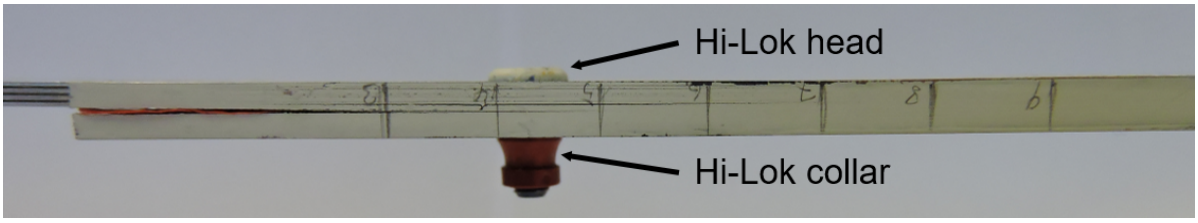

(a) Specimen 4_06_GF_HL_16.5 - Side view

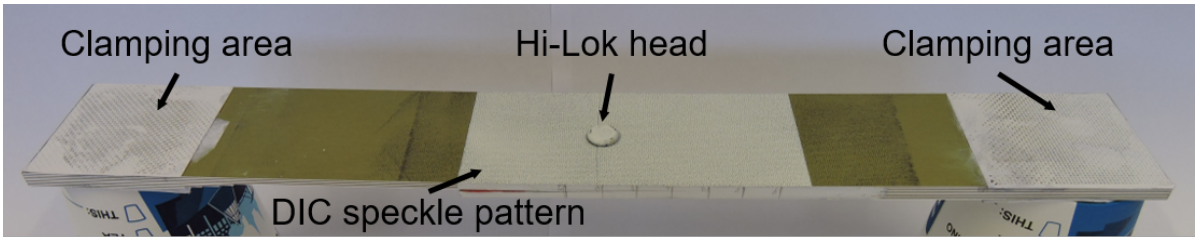

(b) Specimen 4_06_GF_HL_16.5 - Angled view

Figure 4.5: A real life example of a CLS specimen with a BDAF (photos taken after testing).

2. Weight has to be minimized to reduce its influence on the stress distributions in the CLS specimen
3. Inertial effects must be kept as low as possible
4. The clamp may not slide to much with respect to the CLS specimen
5. The applied clamping pressure must be able to be controlled and stay constant throughout the fatigue test

- The resulting clamp design is visualized in fig. 4.6(a) and fig. 4.6(b). The clamping pressure is applied by a bolt and the pressure level is controlled using torque wrench. A 'locking' nut secures the bolt in the clamped position. Intertial effects are limited by wedging foam supports between the specimen and the clamp which restrict the rotational movement without contributing to the overall stiffness of the specimen. Double sided adhesive tape between the specimen surfaces and the clamp avoids major relative sliding. Preliminary testing with a prototype and the final clamp design showed satisfactory results for all criteria

- The CDAF is installed with a bolt torque of 5 Nm which results in a clamping pressure of 100-200 MPa which was found the be similar to the pressure exerted by the Hi-Lok head (see appendix D). The surface on which the pressure is applied is approximately 0.4 mm long and has the width of the specimen

Disbond Arrest Feature Position

The position of the BDAF and CDAF with respect to the overlap region were determined differently for the adhesive and prepreg bondline specimens.

Adhesive bondline specimens:

- As previously mentioned, the high loads required to achieve disbond growth lead to early fatigue crack initiation in the aluminum plies. As a result, the cycle range available for testing was not sufficient to capture the entire disbond growth behavior with a single test. To solve the issue, the disbond growth behavior will be characterized by splitting the test into two separate tests:

  – **Test 1**: the region of growth towards the DAF by placing the DAF further away from the Teflon foil

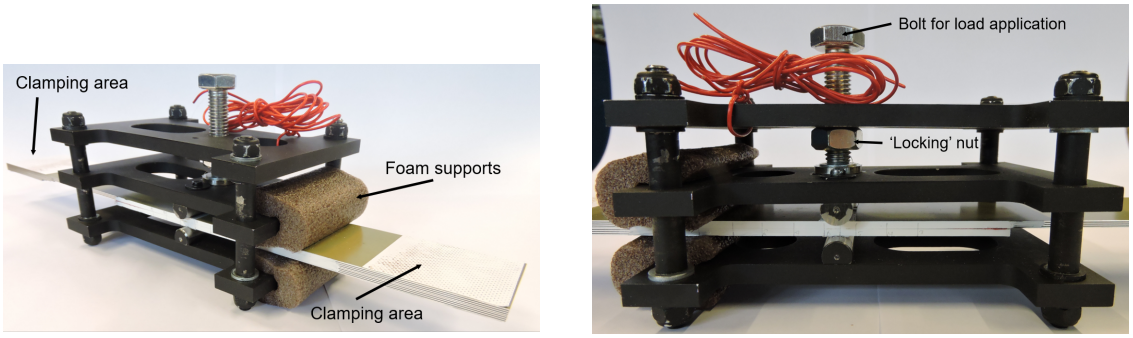

(a) Specimen 4_07_GF_C_19.5 - Angled view (b) Specimen 4_07_GF_C_19.5 - Side view

Figure 4.6: A real life example of a CLS specimen with a CDAF (photo taken after testing).

– **Test 2**: he region of growth after reaching the DAF by placing the DAF as close as possible to the Teflon foil

Combing the test results should, in theory, result in the overall disbond growth behavior curve as shown in fig. 4.7. The CDAF and BDAF were placed at 35 mm and 45 mm from the overlap edge.

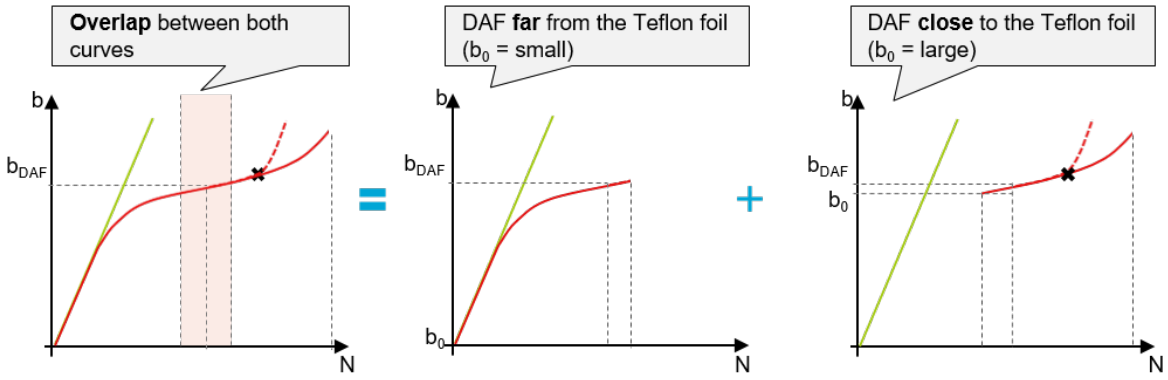

Figure 4.7: An illustration of the disbond growth results of a CLS specimen with a DAF by assembling the results of two separate fatigue tests: disbond growth before and after the DAF.

Prepreg bond line specimens:

- Originally, it was planned to characterize the DAF disbond growth behavior in a single test and by assembly just as discussed for the adhesive bondline specimens. Comparing the single test and assembled curves would identify discrepancies that arise from the assembling procedure and these were to be extrapolated to explain possible observations in the assembled adhesive bond line specimen results. During testing however, it was decided that testing different maximum fatigue loads would yield more valuable information, therefore departing from the original plans. The BDAFs were already placed at different positions according to the original plan, but this serves no specific purpose in the final execution of the experiments. An overview of the DAF positions is given in table 4.5

4.1.2. Specimen Production

With the design of the specimens known, the production process was established which is summarized in fig. 4.8 and explained below. No final quality assurance step was performed due to time constraints.

1. **Glare production**: The plies are cut, assembled, covered in a vacuum bag en then cured in an autoclave with the curing cycle given in fig. 4.9

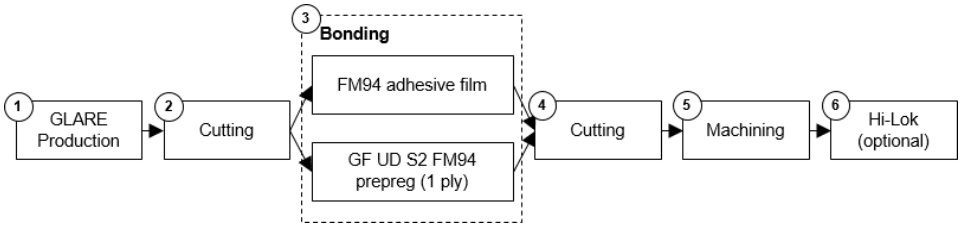

Figure 4.8: The CLS specimen production process.

2. **Cutting**: After the FML has been cured, the panel is sawed into smaller plates as shown in fig. 4.10(a)
3. **Bonding**: The Teflon foil and bond line material are cut on an automated ply cutter before the plates are bonded using the appropriate curing cycle shown in fig. 4.9. The result of the bonding process and the saw tooth shape cutting process is shown in fig. 4.10(b) and fig. 4.11 respectively
4. **Cutting**: After curing, the bonded plate is cut into strips which are slightly wider than the final dimensions of the CLS specimens
5. **Machining**: The strips are machined into their final dimensions for accuracy and smooth edges which will not influence fatigue crack initiation
6. **Hi-Lok (optional)**: The 4.8 mm titanium Hi-Loks are installed by pre-drilling a hole with a 2.4 mm drill and finally to the final diameter of 4.8 mm. It must be noted that a better process would be to drill the hole up to 4.7 mm and to use a precision reamer for the final 4.8 mm diameter. However, such a reamer was not available, moreover the 4.8 mm drill resulted in a very tight fit and was accepted for these testing purposes

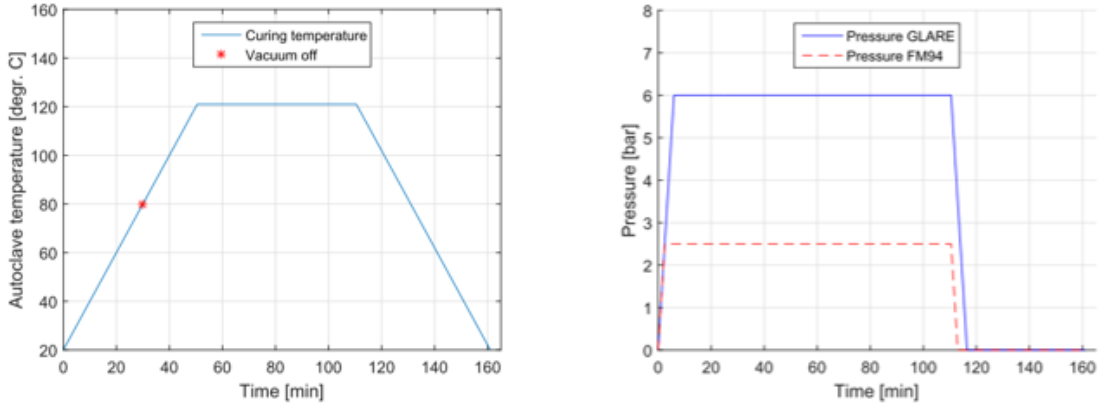

(a) Temperature cycle

(b) Pressure cycle

Figure 4.9: Curing cycles for GLARE and FM94 (from Hanx [7]).

4.1.3. Test setup

After the specimen selection, design and production the test setup has been defined. Fatigue tests have been performed at the Faculty of Aerospace Engineering of the TUDelft on a 60 kN self-built MTS using the appropriate fatigue test parameters. Based on the experimental goals, the disbond length, DGR, disbond area, Disbond Area Growth Rate (DAGR) and the appearance of adherend fatigue damage must be measured.

Fatigue Test Parameters

The maximum fatigue load must be selected such that the disbond growth necessary to characterize the behavior of a DAF can be achieved before the initiation of adherend fatigue damage occurs. This

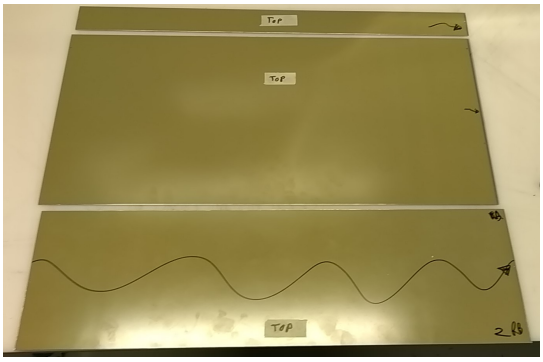

(a) Step 2 results: GLARE plates ready for step 3; bonding.

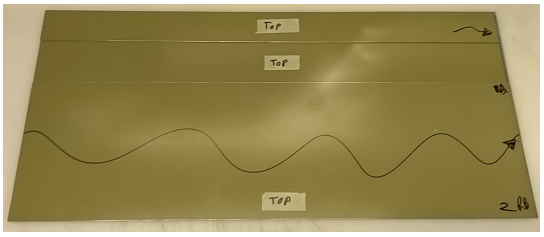

(b) Step 3 results: bonded GLARE plates ready for step 4; cutting.

Figure 4.10: Production process examples of step 2 (cutting) and step 3 (bonding).

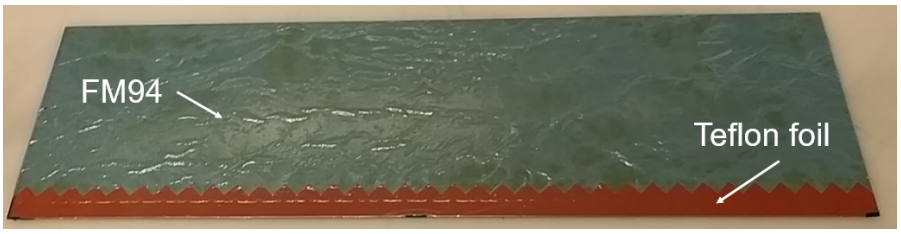

Figure 4.11: Production process example: Teflon foil and bond line material (FM94 adhesive film in this image).

depends on the DGR and the number of load cycles at adherend fatigue damage initiation which increase and decrease respectively with an increase in the maximum load. The issue is that predicting the relative change of both parameters is difficult due to the geometric non-linear nature of a CLS specimen [10]. This problem was solved by experimental testing of the adhesive and prepreg bondline specimens separately which is detailed in appendix C. Only the results are shown here.

All specimens were loaded at a Constant Amplitude (CA) loading at a R-ratio and frequency of 0.1 and 5 Hz respectively similar to Hanx [7].

Adhesive bond line specimens:

- First, a maximum fatigue load of 28 kN is applied to initiate the disbond. Second, when the disbond length on the left and right side has grown beyond the edge of the Teflon foil at 30 mm, the load is lowered to 26 kN for the remainder of the fatigue test

Prepreg bond line specimens:

- The prepreg bonded specimens are loaded at a maximum load of 16, 19.5 and 21 kN without a disbond initiation load step

An overview of the individual specimens and the applied loads is given in table 4.5.

Test Equipment

The first part of the experimental goals requires the measurement of disbond growth over time. To do so, two measurement techniques have been used:

1. Visual inspection will be performed on both sides of the CLS specimen by using cameras to take a photo every 500 load cycles. After testing, the disbond length is obtained from theses images and combined with the corresponding load cycle number the disbond growth and growth rate can be determined

2. DIC cameras will be used to monitor the disbond growth around the BDAF by measuring and analyzing the strain field. As the loads pass from the top to the bottom adherend through the adhesive, a distinctive gradient in the strain field in the top adherend is expected in the direct proximity of the disbond front. Other studies have used DIC cameras in similar applications, but simple thresholding was applied for the strain field analysis [7, 45]. This study will be the first known attempt to use modelling knowledge of the strain field distribution to create an algorithm that can locate the disbond front on a frame-by-frame basis. The DIC cameras cannot be used for the CDAF specimens as the field of view is obstructed by the clamp. However, it is expected that the disbond will propagate with a straight front anyway in the CDAF specimens

The second part of the experimental goals requires knowledge of the location and number of load cycles at adherend fatigue damage initiation. This is achieved by inspection of the images taken from the visual disbond length inspection and DIC cameras (see above). However, some parts of the specimen are outside the field of view of these cameras. Therefore, a third measurement technique is applied:

3. A micro-USB camera will be used to inspect appearance of adherent fatigue damage and its progression every 20,000 cycles at the locations outside the field of view of the cameras. It must be noted that these inspection methods give information of the initial appearance of damages and not the initiation as this could occur inside the laminate which cannot be detected visually

The test setup is illustrated in fig. 4.12 and the real life setup is shown for the CDAF and BDAF specimens in fig. 4.13(a) and fig. 4.13(b) respectively.

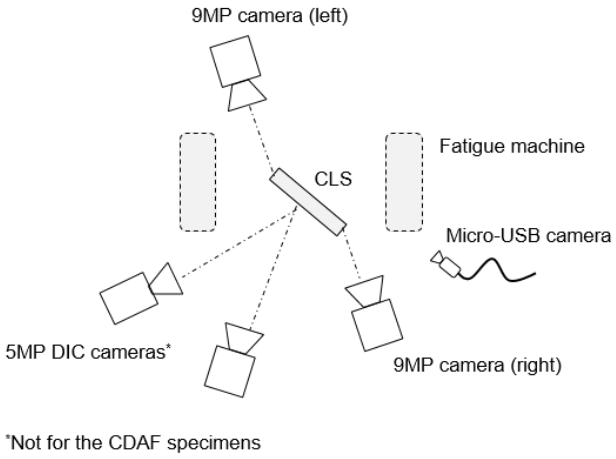

Figure 4.12: Illustration of the test setup.

Test Matrix

The test matrix of the tested specimens is shown below in table 4.5. Note the R-ratio and loading frequency of 0.1 and 5 Hz respectively were the same for all specimens and they are therefore not displayed in the overview.

4.1.4. Data Acquisition and Processing Methods

The three measurement techniques were briefly introduced when discussing the test setup. Together, these measurement techniques generate the five required experimental outputs directly or indirectly by processing of the measured data as shown in fig. 4.14. A detailed overview of the three measurement techniques is given here by expanding on the inputs, outputs and the data processing that is performed.

Disbond Growth and Disbond Growth Rate by Visual Inspection

The goal of the visual inspection using cameras is to measure the disbond length b over time and to use that information to obtain the Disbond Growth Rate db/dN. This is achieved by placing two cameras, each on one side of the specimen, which make an image very 500 cycles from which the disbond length can be measured. The edges are painted white with watered down Tipp-Ex so that the disbond can

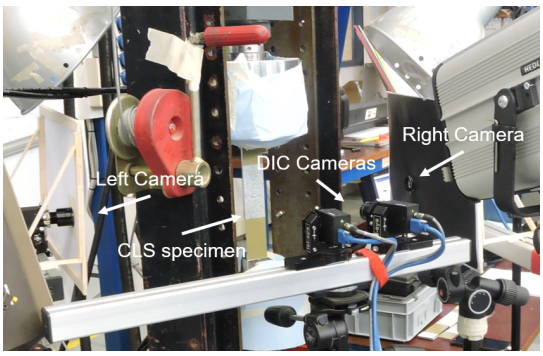

(a) Bolted Disbond Arrest Feature (BDAF) test setup from the DIC perspective.

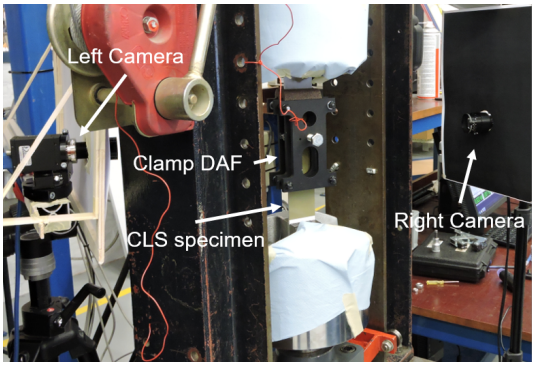

(b) Clamped Disbond Arrest Feature (CDAF) test setup from the frontal perspective.

Figure 4.13: Lab execution of the test setup.

Table 4.5: Test matrix.

Batch	Bondline interface	DAF		Load [kN]		Specimen ID	Static strength	Disbond	
		Type	b_{DAF} [mm]	Initiation	Growth			Length	Area
2	FM 94 adhesive film with a carrier	-	-	-	Static	2_01	X		
		No DAF	-	28	26	2_11		X	X
		CDAF	45	28	26	2_10		X	
			35	28	26	2_09		X	
		BDAF	35	28	26	2_12		X	X
			45	28	26	2_13		X	X
4	Glass Fiber S2 FM94 UD prepreg (1 ply)	No DAF	-	-	16.5	4_08		X	X
		CDAF	55	-	19.5	4_07		X	
		BDAF	40	-	19.5	4_06		X	X
			65	-	21	4_09		X	X
			55	-	16.5	4_10		X	X

Output / Technique	Disbond length (b)	Disbond area (A_b)	Disbond growth rate (db/dN)	Disbond area growth rate (dA_b/dN)	Adherent fatigue damage
Visual inspection (cameras)	Measured directly		Obtained through processing		Measured directly
Strain field (DIC)		Obtained through processing		Obtained through processing	Measured directly
Visual inspection (micro-USB camera)					Measured directly

Figure 4.14: An overview of the experimental data acquisition methods and how they span across the required outputs

be seen more clearly. A secondary goal of these measurements is to provide validation data for the processed disbond area A_b tracking algorithm.

The data processing steps required are shown in fig. 4.15 and consist of two steps:

1. The images are processed using a self developed MATLAB tool where the disbond length is measured based on the pixel length and the pixel size in mm. The corresponding load cycle is derived from the image number and the number of load cycles between each image

2. The disbond length and respective cycle number are used to calculated the DGR by applying the

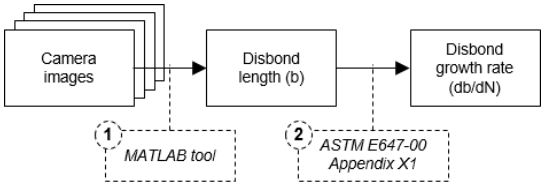

Figure 4.15: Data processing steps - Disbond length and DGR by visual inspection.

Incremental Polynomial Method which is provided by the ASTM Standard E647 [79]. This method deploys a second-order polynomial fit on a $2n+1$ set of successive data points. The derivative of the polynomial fit is used to find the DGR at the center coordinate and then the $2n+1$ frame moves to the next data point. One has to be aware that this results in the loss of $2n$ data points, but this is no problem if lots if data points exist. In this experiment, 3 was used for n

Disbond Area and Disbond Area Growth Rate by Strain Field Data

The goal of the strain field data obtained by the the Digital Image Correlation (DIC) cameras is to find the disbond area A_b over time and to use that information to obtain the Disbond Area Growth Rate (DAGR) dA_b/dN.

DIC is a measuring technique that uses two cameras to track displacements on a surface. Based on the relative difference in displacements in between images, properties such as strain can be calculated. In order to track surface displacements, a speckle pattern must be applied to the surface as shown in fig. 4.16. Generally, the smaller the speckles are, the higher the accuracy becomes. However, speckles that are too small will become very difficult to distinguish. An often applied rule of thumb is that the speckle size should roughly be 3 pixels for an optimal analysis.

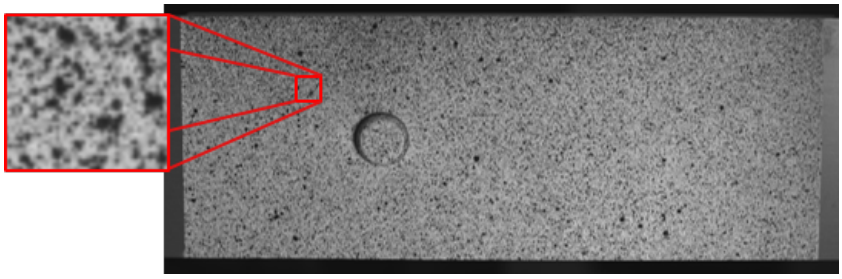

Figure 4.16: Example of a DIC speckle pattern (specimen 2_45)

Images will be taken every 500 load cycles by ramping up the load to the maximum load and sending a signal from the fatigue machine to the DIC camera setup. The load ramp up segments are not included in the load cycle counter.

Before measuring, calibration needs to be performed so that the cameras know their position in space with respect to each other. No calibration was accepted with a larger error than 0.019 [-].

The data processing steps required are shown in fig. 4.17 and consists of three steps:

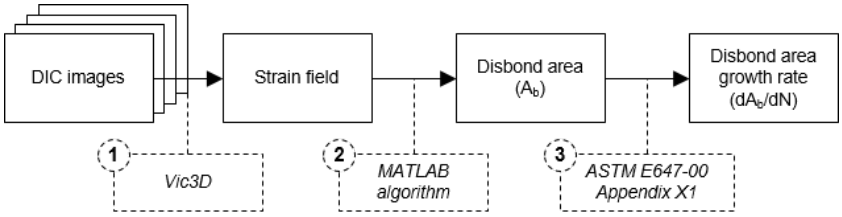

Figure 4.17: Data processing steps - Disbond area and DAGR by strain field data

1. The strain field is obtained from the raw DIC images by using a commercial software called *Vic3D*. To perform the analysis, a subset size and a step size need to be defined. By selecting the subset size, the area of interest is divided into smaller areas, or subsets, which are used to track displacements. The step size determines how many of those subsets in the x and y direction are used to create a single data point. Another important setting is the strain filter, which basically applies an averaging filter to the output. The larger the subset and/or step size becomes, the less data points remain. Therefore, a large subset and step size must be used in conjunction with a small strain filter to avoid averaging out data too much

2. A self developed algorithm processes the strain field images to find the location of the disbond front. The total disbonded area can be found based on the disbond front. The algorithm can locate the disbond front by looking for key characteristics in the strain field that have been shown to correlate directly and consistently with the location of the disbond front. This processing algorithm is detailed in appendix F

3. The DAGR is found by applying the Incremental Polynomial Method which is provided by the ASTM Standard E647 [79] as already discussed

Visual Inspection (micro-USB camera)

The goal off the visual inspection by micro-USB camera is to monitor for adherend fatigue damage on the outside of the CLS specimen in regions outside the field of view of the DIC and disbond length monitoring cameras. Inspection will be performed every 20,000 cycles whilst statically loading the specimen at the maximum fatigue load. These moments of damage observations do not represent actual moment of damage initiations as they can have occurred inside the adherend before being visible on the outside.

4.2. Disbond Growth Model (MATLAB)

Part of the first research objective is to the understand the conditions necessary for arrest and part of the second research objective is to study the relation between the DGR and adherend fatigue damage initiation. A simple, intuitive and robust analytical model could provide the means to study these topics on a high level so that an initial understanding can be created.

To study the conditions necessary for arrest, different SERR footprints have to be analyzed which are not necessarily related to a bolt. The analysis of different and sometimes random SERR footprints cannot be delivered by the existing models [6, 39] as they have the bolted DAF embedded into their solution. It was therefore decided to develop a new analytical disbond growth model.

The aim of this section is to provide the reader with a level of understanding of the developed analytical disbond growth model which is required for the remainder of this report. The numerical implementation is given appendix E and the equations are detailed in the model which can be accessed via the online GitHub repository Git [80]. First, the model scope is discussed in section 4.2.1. Second, a brief summary of the model is given in section 4.2.2 and third is a more detailed discussion of the individual model components in section 4.2.3.

4.2.1. Model Scope

The first step of the model development was to determine the scope so that the complexity could be reduced to a minimum level. The scope of the model is formulated by the model objective, requirements and the governing assumptions.

Model objectives:

1. Provide a simplistic way to implement and study the effect of various DAF configurations on the disbond growth in a FML CLS specimen

2. Provide the ability to perform a preliminary study on the relation between the adhesive DGR and fatigue crack initiation in the aluminum plies

Model requirements:

1. The following inputs must be handled by the model:
   (a) Layup and ply materials of a FML
   (b) Clamped-clamped support boundary conditions based on the fatigue test conditions
   (c) Maximum fatigue load and R-ratio
   (d) Geometry of the CLS specimen
   (e) Aluminum S-N data
   (f) Bond line material disbond growth data (Paris-Law coefficients)
   (g) The effect on the SERR of a DAF
2. The calculation procedures must be able to account for the following aspects:
   (a) Geometric non-linear behavior of the CLS specimen
   (b) MM disbond growth in the bondline interface
   (c) Fatigue accumulation in the aluminum plies under Variable Amplitude (VA) loading
   (d) Varying R-ratio in the aluminum plies along the length of the specimen for the fatigue accumulation calculations
3. The model must give the complete history of the following outputs:
   (a) Bondline DGR
   (b) Disbond length versus load cycle
   (c) Location and cycle number of fatigue crack initiation in the aluminum plies
4. General requirements are:
   (a) The model must be as easy and intuitive as possible

Governing Simplifications:

1. The disbond growth model is reduced to a 1D representation of the CLS specimen
2. The physical DAF is not included into the model which implies a set of sub-assumptions:
   (a) The effect of the DAF is not solved by the model and must be included as an input
   (b) The effect of the DAF on the load distributions and the resulting stress cycles in the FML plies are not included
3. Only fatigue crack initiation in the aluminum plies will be considered out of the various adhered fatigue damage modes based on the research hypothesis
4. Fatigue crack growth in the aluminum plies and its effect on the disbond growth behavior is not included
5. Disbond initiation in the bond line interface is not included
6. Linear Elastic Fracture Mechanics (LEFM) is applied so the model is assumed to be in the linear elastic range
7. No distinction is made between cohesive/adhesive disbond growth

With the scope of the model determined, the model methodology has been developed.

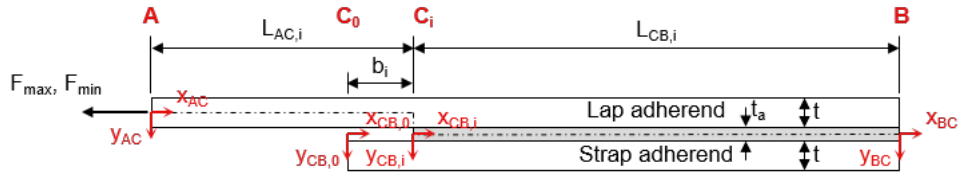

Figure 4.18: The main dimensions and reference frames at disbond increment i used to model the CLS specimen.

4.2.2. A Brief Summary of the Model

The model scope has been formulated which is defined by the model objectives, requirements and the governing assumptions. Based on this scope, the disbond growth model model has been developed.

The 2D representation of CLS specimen on which the model is based is shown in fig. 4.18 with the geometric parameters and relevant reference frames at disbond increment i.

A schematic overview of the model is given in fig. 4.19 highlighting the four model components and their placement in the context of the entire model. The four components are responsible for the following calculations:

1. The FML smeared properties and residual thermal strains (optional) are calculated and the CLS geometry is discretized into the given number of elements
2. The axial load, shear load and bending moment distributions in the lap and strap adherend are calculated at the minimum and maximum load of the fatigue cycle. These are subsequently used to find the strain and stress cycles in the FML plies and the Mode I and Mode II SERR components are calculated
3. The LEFM based MM disbond growth model of Bürger [8] is used to find the DGR which is numerically integrated over the disbond length increment to find the corresponding number of load cycles
4. The stress cycles in the aluminum plies are used to find the local R-ratio's so that the fatigue accumulation can be calculated for the disbond length increment with the aluminum S-N data and the Palmgren–Miner rule

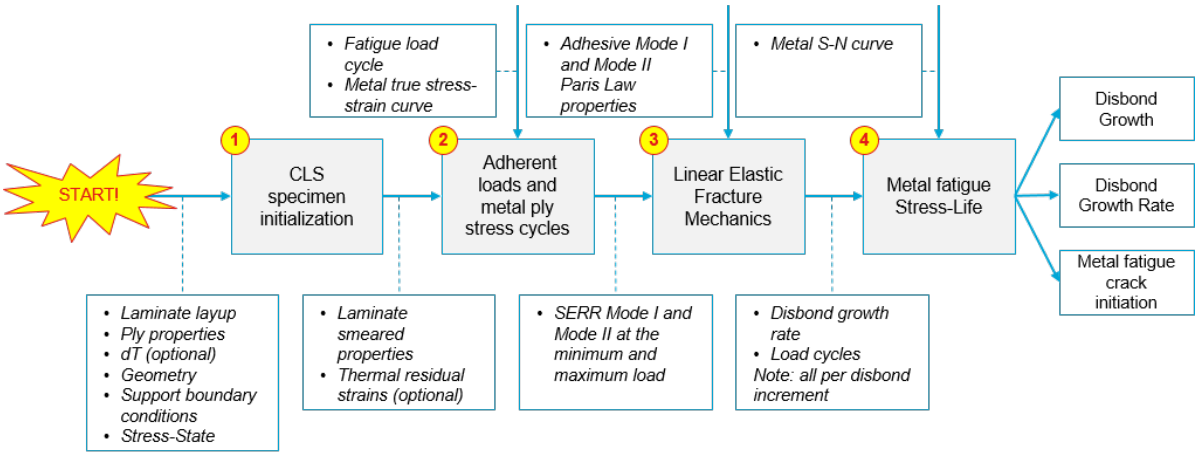

Figure 4.19: The quasi-analytical disbond growth model consists of four main model components.

4.2.3. Model Components Explained

The model summary has shown the general outline of the four model components. A more thorough overview of goal, inputs and calculations of the individual components is given here.

Component 1 - CLS Specimen Initialization

The goal is to find the laminate smeared properties, the laminate residual strains (optionally) and the element coordinates of the discretized adherends.

As input the component takes the FML layup, ply materials, the difference between the curing and application temperature (optionally) and the initial CLS geometry. Only symmetrical and balanced laminates may be entered. Finally, the support boundary conditions (clamped-clamped or roller-roller) and the stress state in the specimen width direction (plane stress or plane strain stress) must be selected.

The smeared laminate properties are found using the Classical Laminate Theory (CLT) which was expanded to include the plane strain condition in the width (or z) direction of the laminate. Optionally, the laminate post curing residual strains are calculated using Tsai and Hanhn [81] as advised by Spronk *et al.* [49]. Finally, the free adherend and overlap region are both discretized to a user defined number of elements.

Component 2 - adherend Loads and Metal Ply Stress Cycles

The goal is to find the axial load, shear load and bending moment distributions in the adherends, the stress cycles in the individual plies and to calculate the Mode I and Mode II SERR components.

As input the component takes the calculated smeared laminate properties, residual strains (optionally) and the adherend element coordinates. Additionally, the user must enter the fatigue load cycle, defined by the maximum load per unit width and R-ratio, and the true-stress strain curve of the metal plies should plasticity be accounted for.

A method developed by Lai *et al.* [73] was used to find the vertical displacements and subsequently the bending moment distribution in free adherend and overlap region. Lai *et al.* [73] derives the solutions for clamped-clamped, roller-roller and clamped-roller support boundary conditions, but these were re-derived by the author as the original equations contained inconsistencies, probably related to typing mistakes. By derivation of the bending moment distribution, the shear load distribution is found.

Lai *et al.* [73] assumes that the overlap region is lumped together whilst in reality the lap and strap adherend deform independently due to the presence of the flexible adhesive interface. No closed-form expression exists for the decoupled adherend load distributions in the overlap region. However, they can readily be found if the load transfer from the lap to the strap adherend along the overlap length is known: the adhesive stresses.

The closed-form solution for the adhesive stresses in a SLJ developed by Goland [82] was used with overlap edge loads from Lai *et al.* [73] as input. The equations were taken from [10] who provide a clear and well explained derivation. By integrating the adhesive stresses over the length of the overlap region, the internal loads at a given section in the lap and strap adherend can be found which are used to find the adherend membrane strain and bending curvature. The membrane strain and curvature are used to find the ply strain and ply stress cycles. It must be said that this solution is geometric linear and actually not valid for the clamped-clamped support boundary conditions. Goland [82] ignores the large deflections of the overlap in the solution of the adhesive stresses and the SLJ is only equivalent to a CLS specimen with roller-roller support boundary conditions. Due to time constraints and in the light of model simplicity, it was decided to to accept these limitations.

The peak stresses in metal plies around the disbond front were found to exceed the aluminum yield and ultimate stress at the tested fatigue loads leading to unrealistic fatigue crack initiation predictions. A simplistic approach was adopted to obtain the metal ply stress directly from the true stress-strain curve based on the strain value. Residual compressive stresses arising from compression by the surrounding elastic material during unloading is not included. Furthermore, material non-linearity is not considered when solving the load and strain distributions of the entire system. This obvious oversimplification can be justified by model requirements of simplicity and providing the means of a preliminary study of the behavior of metal fatigue crack initiation; not to provide accurate predictions.

The SERR Mode I and Mode II components are calculated with the equations derived by Fernlund and Spelt [14] using the J-integral around the contour of the overlap region in a CLS specimen with identical, symmetrical and balanced adherends. These equations showed an excellent fit compared to geometric non-linear FEM results.

Component 3 - Linear Elastic Fracture Mechanics

The goal is to calculate the DGR for a disbond increment and the number of load cycles it requires for the disbond to propagate through an element.

As input the component takes the calculated Mode I and Mode II SERR components and the disbond length increment. As manual input the bondline material fracture parameters are needed from [8] and the SERR Footprint must be entered.

A LEFM Mixed Mode (MM) disbond growth model developed by Bürger [8] was used to calculate the DGR based on the Mode I SERR component, the MR and the bond line material fracture parameters characterizing the resistance to growth in pure Mode I and Mode II loading. The fracture parameters for the adhesive and prepreg bond line material are summarized in table 4.6. The FM94 adhesive parameters were obtained from [8] and the prepreg parameters were found by adjusting and re-fitting the material data from [18] which is detailed in appendix G.

Table 4.6: Adhesive and prepreg bond line material fracture parameters for the MM disbond growth model of Bürger [8] with G_{eq1} in (J/m^2) and b in (m).

Coefficient	Value	Comment
FM94 Adhesive Film		
$C_{0\%}$	$5.27{\cdot}10^{-17}$	Obtained from table 5.1 in [8]
$C_{100\%}$	$2.07{\cdot}10^{-18}$	Obtained from table 5.1 in [8]
$m_{0\%}$	3.78	Obtained from figure 5.11 in [8]
GF UD S2 FM94 prepreg		
$C_{0\%}$	$2.77{\cdot}10^{-16}$	Derived from [18]
$C_{100\%}$	$9.21{\cdot}10^{-20}$	Derived from [18]
$m_{0\%}$	4.95	Derived from [18]

The number of load cycles corresponding to a disbond increment through an element was found by simply dividing the element length by the DGR. This implicitly assumes that the conditions causing disbond growth, the SERR and MR, are constant when growing through an element. In reality, conditions change per load cycle (and even during the load cycle [50]), but modeling per load cycle is computationally very expensive. Furthermore, the CLS specimen has a unique characteristic that the SERR and MR are practically constant over a major portion of the overlap length. Therefore, the error introduced by assuming a constant disbond driving state through an incremental increase in disbond length is expected to be very small in the special case of a CLS specimen.

Component 4 - Metal Fatigue Stress-Life

The goal is to predict the location and number of load cycles at fatigue crack initiation in the metal plies.

As input the component takes the calculated number of load cycles per disbond length increment and the stress cycle in each metal ply. As manual input the metal S-N curves are needed.

A peak stress exists in the metal ply adjacent to the disbond front caused by the tensile load, the bending moment and the stress concentration factor from the stiffness mismatch [46, 47]. During disbond growth, this peak stress moves along the metal ply and the changing CLS specimen geometry alters the stress distributions. All of this leads to variable amplitude loading which must be accounted for to achieve a realistic representation of the metal fatigue crack initiation behavior.

The prediction of fatigue crack initiation is performed using best-fit S-N curves for an unnotched, monolithic 2024-T3 aluminum alloy sheet, longitudinal direction and a bare sheet thickness of 0.090-inch (or 2.286 mm) from page 3-115 in [83]. No S-N curves were found for unnotched monolithic

sheets of 0.4 mm thickness which is used in the FML adherends. However, using the S-N curve of a thicker sheet can be justified as the thickness effect will lead to conservative predictions. The fatigue life prediction at a given R-ratio is calculated by

$$\log N_f = 11.1 - 3.97 \log\left(S_{max}\,(1-R)^{0.56} - 15.8\right) \tag{4.1}$$

Where N_f is the number of cycles until fatigue crack initiation, S_{max} is the maximum stress in KSI and R is the load ratio. In each ply, the load ratio R is calculated locally per element and is used instead of the global R-ratio of the applied load. The Palmgren–Miner Rule is used to account for variable amplitude loading, but one has to be aware that it has been criticized for having many limitations (see for example [40, 52, 84].

4.3. SERR Footprint Model (FEM)

In order to model the ratio by the CDAF the change in the SERR must be known. Furthermore, knowledge of the SERR greatly helps to interpret the experimental disbond growth results. A 2D FEM model has been developed in a commercial software package Abaqus for these purposes which is described here.

Cracked Lap Shear Specimen Model

The model was developed to mimic the CLS specimen design of the adhesive bondline specimens, but the appropriate boundary conditions were applied to the specimen edges instead of modeling the sections clamped by the fatigue testing machine as illustrated in fig. 4.20.

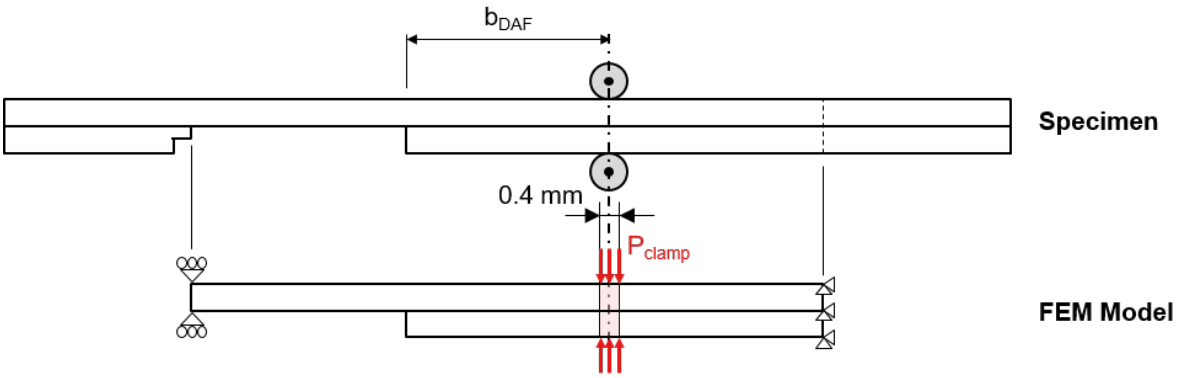

Figure 4.20: Comparison of the test specimen and FEM model geometry.

The FML layup and materials discussed in section 4.1.1 were used and the laminate was modelled by creating partitions with the appropriate ply thickness, material properties and their orientation. Adjacent plies of the same material have been modeled as a single ply with twice the prepreg thickness for computational efficiency. The adhesive material is not modeled, but included as a surface-to-surface interaction.

Geometric non-linearity is selected and CPS4 elements are used. Meshing is performed with an approximate element size of 0.25 and one element is used for the ply thickness. This fine mesh was possible because a 2D model is computationally inexpensive and because it avoids the need for a mesh convergence study.

The contact interaction between the two adherends is a surface-to-surface (standard) contact definition with small sliding and a node-to-surface discretization method. The contact properties "Frictionless" and "Hard" contact were selected for the tangential and normal behavior respectively. The bonded/disbonded regions were modeled by limiting the bonding to a subset of slave nodes. The inbuilt VCCT function was used to obtain the SERR Mode I and Mode II components.

A uniform initial clearance was needed to get the solution to converge together with the automatic stabilization option with the default settings. As general rule, stabilization is allowed if the energy

dissipated (ALLSD) is smaller than 1 to 5% of the total energy in the system (ALLIE), which was confirmed to be the case.

Clamped Disbond Arrest Feature Model

Modeling of the CDAF was simplified to just the clamping pressure to avoid physically modeling the clamp and the complex contact interactions. The clamping pressure is modeled by applying a surface traction force on the lap and strap adherend in the opposite direction as shown in fig. 4.20. Surface traction forces represent a force per unit area that act on a selected area, or in this case, on a 0.4 mm long section. Surface traction forces were selected as their direction of application stays normal to the deformed surface. The length of 0.4 mm was selected somewhat arbitrarily with the only guidance that it must represent the area of applied load from the CDAF.

A major shortcoming of using surface traction forces is that the areas where the pressure is applied can slide relative to each other. In reality, the stiffness of the CDAF will make sure that the clamping pressures on the opposite surfaces are always aligned with each other which is not the case in the current model.

5

Results

In order to establish the potential and weaknesses of bolts as Disbond Arrest Features (DAF) in bonded Fibre Metal Laminate (FML) joints, a three component solution methodology has been developed. These components are: (1) the Cracked Lap Shear (CLS) fatigue experiments, (2) the Strain Energy Release Rate (SERR) Footprint Model and (3) the Disbond Growth Model, all of which are thoroughly discussed in the previous chapter.

All components have been executed and the results of the fatigue CLS experiments are discussed in this chapter. The SERR Footprint Model and Disbond Growth Model results will be discussed in chapter 6 and chapter 8 respectively as they form an integrate part of the analysis. Only the verification of both models is detailed in this chapter.

First, the results of the CLS experiments are presented followed by the verification of the SERR Footprint Model and the Disbond Growth Model.

5.1. Cracked Lap Shear Experiments

Fatigue experiments have been performed using CLS specimens with FML adherends that are bonded with an adhesive or prepreg bond line material to analyze the arresting behavior of two different DAF configurations: the Clamped Disbond Arrest Feature (CDAF) and the Bolted Disbond Arrest Feature (BDAF). The data points that have been measured are the disbond length, Disbond Growth Rate (DGR), disbond area, Disbond Area Growth Rate (DAGR) and the location and load cycle of the detected adherend fatigue damages.

Three measuring techniques have been used to obtain the aforementioned data points. First, visual inspection using camera's to measure the disbond length. Second, Digital Image Correlation (DIC) camera's to measure the strain field which will be used to find the disbond area. Third, a micro-USB camera has been used for the detection of fatigue damages.

The results of the CLS fatigue experiments that are presented here are: the disbond length, disbond area and the load cycle number and location of the detected adherend fatigue damages. The processed DGR and DAGR are summarized and analyzed in chapter 7.

A schematic overview of the nomenclature and the measurement definition of disbond length used throughout this section is given in fig. 5.1.

5.1.1. Disbond Length

The disbond length is measured from photos of the specimen edges taken at known load cycle intervals and by post-processing as discussed in section 4.1.4. The average disbond length, b_{ave}, equals the average of the measured left b_L and right b_R disbond length and their definition is illustrated in fig. 5.1. Post processing of the images was performed until the adherend fatigue damage had grown to a level

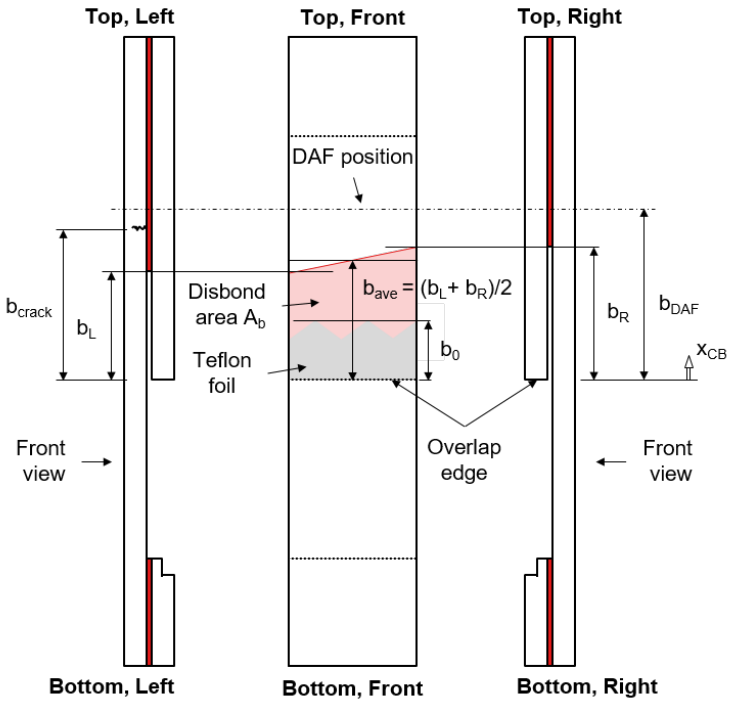

Figure 5.1: Nomenclature and the disbond length and area definition for all CLS specimens.

that the obtained disbond length was deemed as unusable.

Processing the images proved to be difficult and problematic at some points which will be discussed first before presenting the disbond length results of the adhesive bond line and prepreg specimens in the mentioned order.

Difficulties Associated with Visual Inspection of the Disbond Front

An example of the post processing step to obtain the disbond length is given in fig. 5.2. Often, locating the disbond front is very difficult due to the Mode II dominated opening of the disbond tip. This problem is even bigger in the region around the DAF where Mode I is restricted by the clamping force of the DAF. The accuracy of this method is therefore limited, but deemed good enough for the purposes of this research.

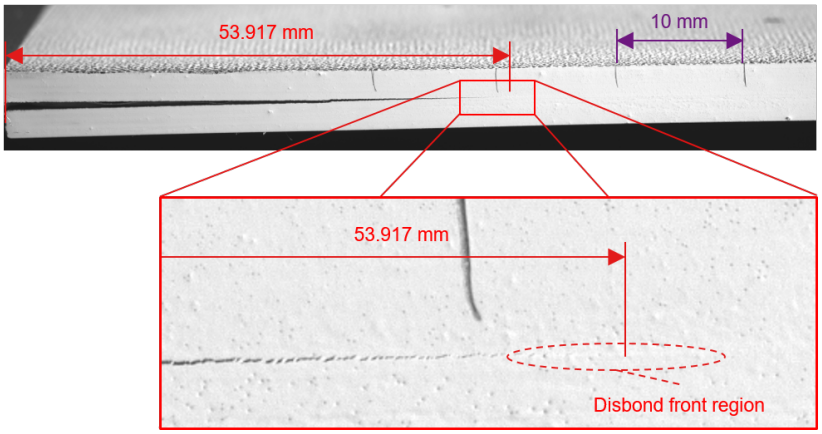

Figure 5.2: Example of a post processing step to obtain the disbond length - specimen 04_08.

Adhesive Bondline Specimens

Five specimens with an adhesive bondline material have been tested. The configurations and loading programs of these specimens are detailed in section 4.1.1 and section 4.1.3 and will not be further discussed here. Images have been taken every 500 cycles, but processing has been done for every 1000 cycles to limited the work load. The average disbond length of the specimens with a CDAF and BDAF placed at 35 mm and 45 mm are compared to the specimen without a DAF in fig. 5.3(a) and fig. 5.3(b) respectively.

The left and right disbond length do not increase equally and in all but one specimen b_R was always larger than b_L. The only exception is specimen 2_09 which was positioned the other way around to see if the observed behavior was related to the fatigue testing machine. This time however, b_L was outgrowing b_R indicating that the behavior might be specimen related. Initially, it was thought the saw tooth shaped Teflon foil, depicted in fig. 5.2, creating an uneven initial b_L and b_R because it has not been centered with the specimens, but no consistent correlation could be found. The root cause was not further investigated as there was no negative impact on the results and the following analysis.

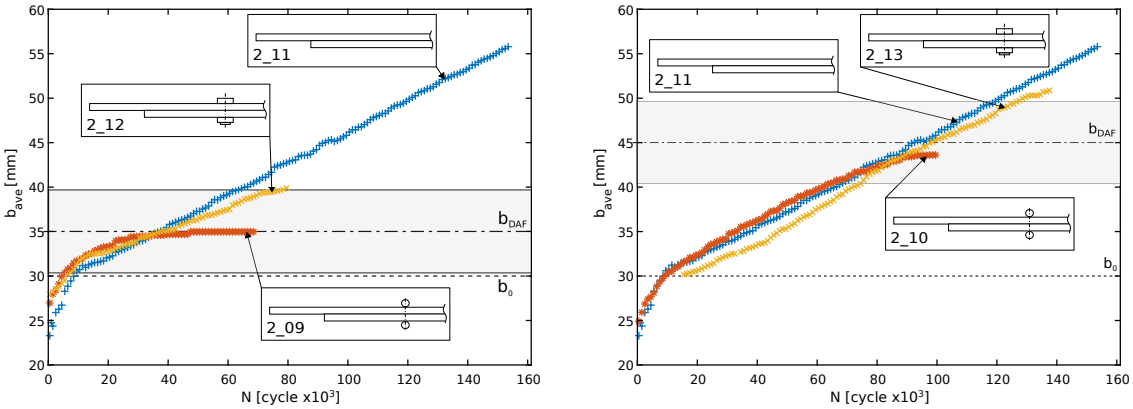

(a) F_{max} = 26 kN and b_{DAF} = 35 mm: (1) No DAF - 2_11, (2) CDAF - 2_09 and (3) BDAF - 2_10.

(b) F_{max} = 26 kN and b_{DAF} = 45 mm: (1) No DAF - 2_11, (2) CDAF - 2_10 and (3) BDAF - 2_13.

Figure 5.3: Average disbond length - Adhesive bond line specimens.

There are three distinct regions that can be recognized in the disbond growth results;

- **Region 1** has a steeper slope from the higher maximum fatigue load of 28 kN for initiating the disbond. The load was lowered to 26 kN once the left and right disbond front had surpassed the Teflon foil at 30 mm so the transition point is not the same for all specimens
- **Region 2** is not affected by the DAF and all specimens show a similar and constant DGR which is in agreement with the expected behavior of a CLS specimen. This region is more difficult to detect with the DAFs placed at 35 mm (or 5 mm from the Teflon foil)
- **Region 3** is where the DAF retards the disbond growth which is different for the CDAF and the BDAF;
  - The CDAF seems to have fully arrested the disbond growth in both specimens in front of the centerline of the CDAF
  - The BDAF does not seem to have arrested the disbond growth in either of the specimens; only the result of the BDAF placed at 35 mm show a recognizable change in the slope of the curve. It is not possible to know whether full arrest would eventually be achieved due initiation and growth of adherend fatigue damages (see section 5.1.3)

The assembly of the disbond length results in the region before and beyond the DAF as proposed in fig. 4.7 can not be performed due to the lack of results in the region behind the DAF. This part of the methodology is therefore cancelled for the remainder of the research.

Several hypotheses can be created based on these results. First, the CDAF has fully arrested the disbond growth in both specimens. Second, the BDAF specimens have not shown a significant disbond growth retardation and it is unknown if this could have been achieved. Third, disbond growth has only occurred in the region of influence of the CDAF and BDAF when placed at 35 mm. These hypotheses will be further investigated in chapter 7 and chapter 8.

Prepreg Bondline Specimens

Five specimens with a GF UD S2 FM94 prepreg material as bondline have been tested. These specimens were designed in an attempt to avoid the high loads required to generate disbond growth in the adhesively bonded specimens. The configurations and loading programs of these specimens is detailed in section 4.1.1 and section 4.1.3 and will not be further discussed here.

The average disbond length results are shown in fig. 5.4(a), fig. 5.4(b), fig. 5.4(c) and fig. 5.4(d) including the left and right disbond length bounds. The results are shown individually because the specimens are tested at different maximum fatigue loads and have different DAF positions; they are not compatible for a single chart. The cycle increment for processing the disbond length images varies per specimen due to the higher number of load cycles. To save processing time, images were processed every 500-1000 load cycles in the region before the DAF, but this was reduced to 10.000-50.000 for the slow growth phase once the disbond had grown beyond the DAF.

Several observations can be made based on the same three regions observed in the adhesive bond line specimens;

1. **Region 1** does not exist for the prepreg bond line specimens because no disbond initiation load has been applied

2. **Region 2** exists in the results of all specimens and also shows a constant DGR similar to the adhesive bond line specimens

3. **Region 3** exists in the results of all specimens, but there is a difference between the CDAF and BDAF;

   (a) The CDAF appears to have fully arrested the disbond growth for a limited number of cycles just behind the center line of the CDAF before disbond growth starts to pick up again. After a while, the DGR starts to increase more rapidly

   (b) The BDAF has significantly reduced the disbond growth in all specimens. Loaded at 21 kN, the results in fig. 5.4(b) show an arrest that kicks in later compared to the specimen loaded at 19.5 kN in fig. 5.4(c). Generally, the maximum arresting effect is achieved behind the BDAF centerline

A special note is given on the results of the specimen 4_07 as disbond growth rapidly increases after a long period of slow growth. A fatigue crack in aluminum ply was detected roughly round the time of the sudden increase which points into the direction of a relation between both events. These events will be analyzed separately for specimen 4_07 in section 7.3.2.

5.1.2. Disbond Shape and Area

The disbond shape and area have been obtained by processing the strain field measurements from the DIC camera's using a self developed software program described in appendix F. The DIC cameras were set to take an image at regular intervals and the displacements are calculated by comparing the image with a reference image as described in section 4.1.4. The reference image was taken of each specimen in an unloaded state and during testing the images were taken at the maximum fatigue load. During data processing, the software program localizes the disbond front by looking for the position in the strain field associated with the disbond front. The disbond front is then extrapolated to the edges of the overlap and the area is calculated which is plotted against the corresponding load cycle number. The algorithm is further detailed appendix F.

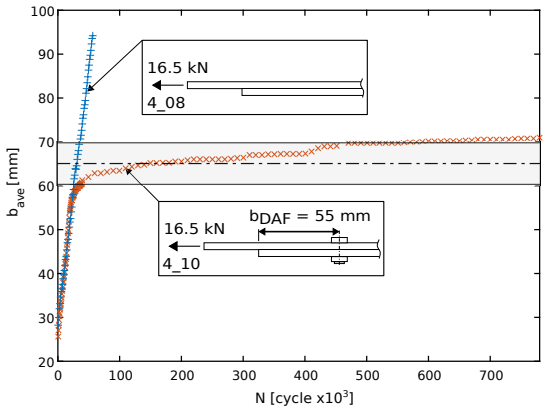

(a) F_{max} = 16.5 kN and b_{DAF} = 55 mm: (1) No DAF - 4_08 and (2) BDAF - 4_10).

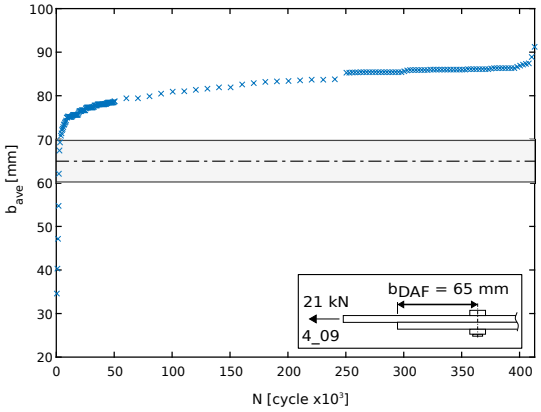

(b) F_{max} = 21 kN and b_{DAF} = 65 mm: BDAF - 4_09.

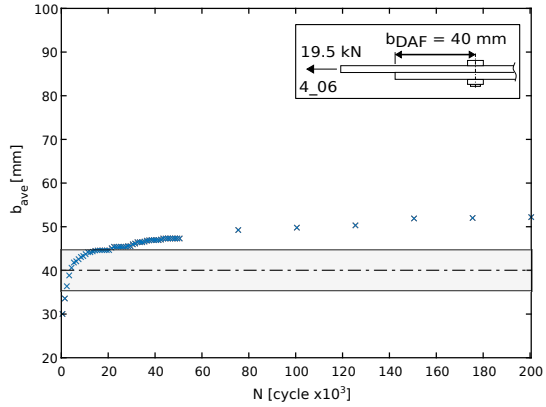

(c) F_{max} = 19.5 kN and b_{DAF} = 40 mm: BDAF - 4_06.

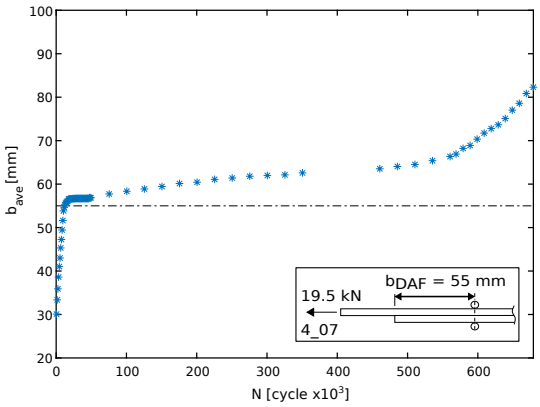

(d) F_{max} = 19.5 kN and b_{DAF} = 55 mm: CDAF - 4_07.

Figure 5.4: Average disbond length - Prepreg bonded line specimens.

Disbond Shape

An example of the raw Digital Image Correlation results plotted using MATLAB and the processed disbond area is shown in 5.5. The disbond area clearly shows the disbond growing around the BDAF in a 'V' shape that is in agreement with observations from [2, 3, 6]. Comparing the disbonded region with the disbond length obtained by visual inspection in appendix F proved the accuracy this new technique.

A significant amount of noise was observed in the DIC data which can be attributed to various sources such as changes in light, the speckle pattern, the calibration etc. A Gaussian filter was applied with a kernel size of 3 as a low pass filter to smooth the data. Using such a filter creates the issue that important data might get lost, but the general trend of a curve remains relatively unchanged (assuming a 'reasonable' sized filter). As the current application only needs the shape of the strain field and not the exact results, this restriction on the data accuracy caused by the filter is no problem.

The disbond area is defined by both the area and the shape. As illustrated in fig. 5.6, two disbonded regions can have the same area, but a different shape which both result in completely different stress distributions. To capture and present the shape of the disbond region parallel to the area, the aspect ratio A_e is introduced as illustrated in fig. 5.6 which is calculated by eq. (5.1);

$$A_e = \frac{A_b}{\left(\frac{b_{max,L}+b_{max,R}}{2}\right)W} \tag{5.1}$$

Where A_e is dimensionless aspect ratio, A_b is the disbond area, $b_{max,L}$ and $b_{max,R}$ are the maximum disbond length of the left and right quadrants respectively and W is the overlap width. The ratio A_e

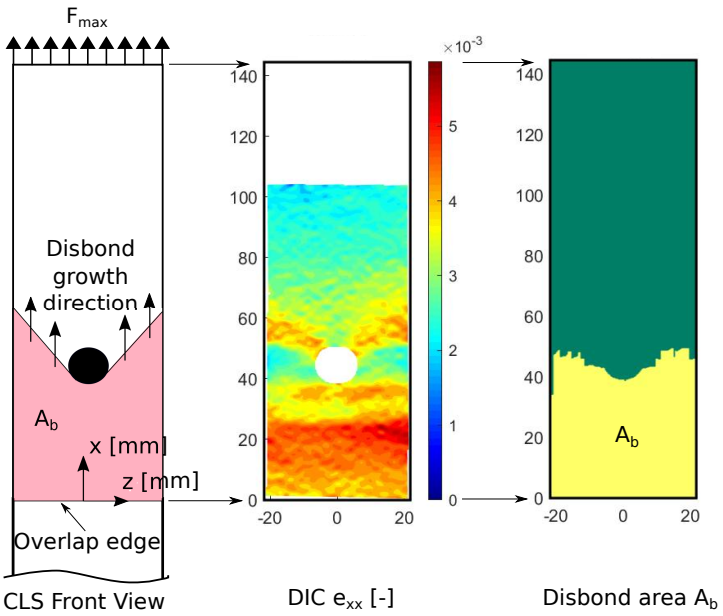

Figure 5.5: Example of the disbonded area as identified by the DIC processing algorithm at N = 124.5 kcycle - specimen 2_13.

quantifies the stretch of the disbond front and equals 1 for a rectangular disbond region with a perfectly straight disbond front and approaches 0 for very stretched shapes.

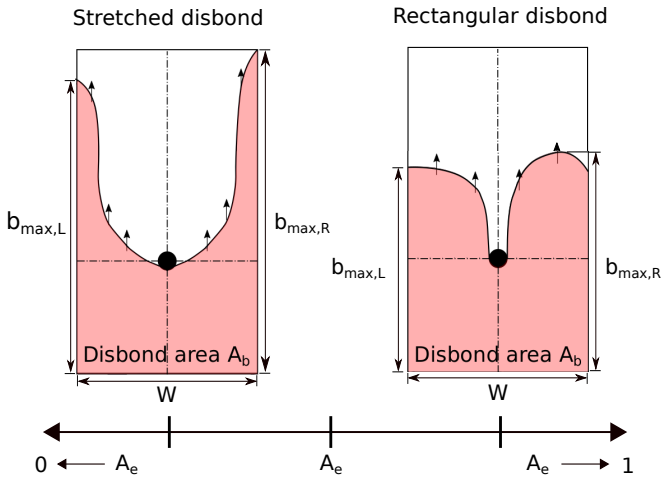

Figure 5.6: Illustration of the aspect ratio A_e of two different disbond shapes, but with the same area A_b.

Disbond Area - Adhesive Bondline Specimens

The disbond area and aspect ratio of the adhesive bond line specimens without and with a BDAF are plotted in fig. 5.7(a) and fig. 5.7(b) respectively against the load cycle number. A change in slope of the A_b curves signals that disbond growth retardation did occur along the disbond front which contradicts the hypothesis based on the disbond length results. The aspect ratio of the BDAF results starts to decrease at the load cycle of the change in the disbond area indicating the disbond front growing around the BDAF therefore taking a more stretched shape.

Disbond Area - Prepreg Bondline Specimens

The disbond area and aspect ratio of the prepreg bond line specimens in fig. 5.7(a) and fig. 5.7(b). The DIC data was too noisy to calculate the aspect ratio and specimen 4_06 could not be processed at all. The lower loads decreased the severity of the strain field making it more difficult to accurately

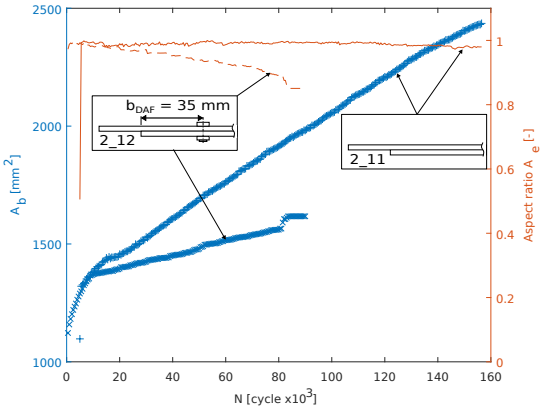

(a) F_{max} = 26 kN and b_{DAF} = 35 mm: (1) No DAF - 2_11 and (2) BDAF - 2_12.

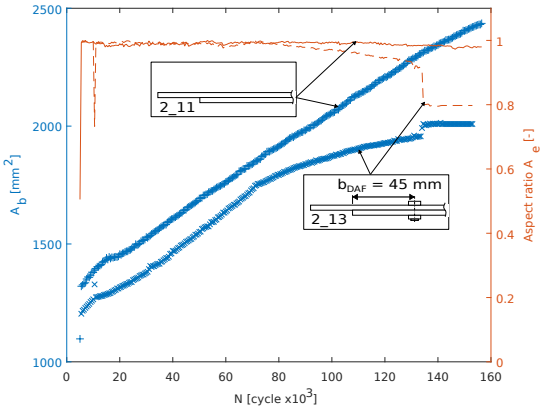

(b) F_{max} = 26 kN and b_{DAF} = 45 mm: (1) No DAF - 2_11 and (2) BDAF - 2_13.

Figure 5.7: Disbond area - Adhesive bond line specimens.

locate the disbond front when the BDAF started to influence the strain field.

Both plots show a remarkable retardation to almost no growth for both BDAF specimens which agrees with the observations based on the disbond growth results.

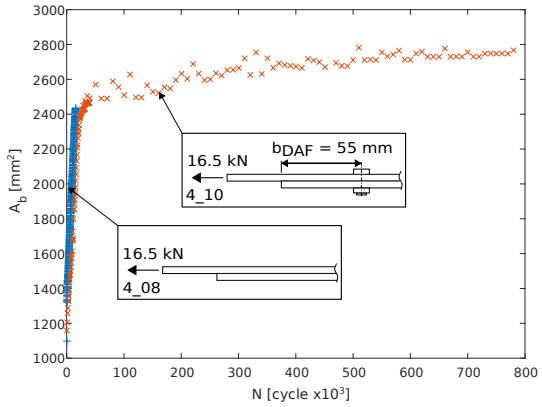

(a) F_{max} = 16.5 kN and b_{DAF} = 55 mm: (1) No DAF - 4_08 and (2) BDAF - 4_10).

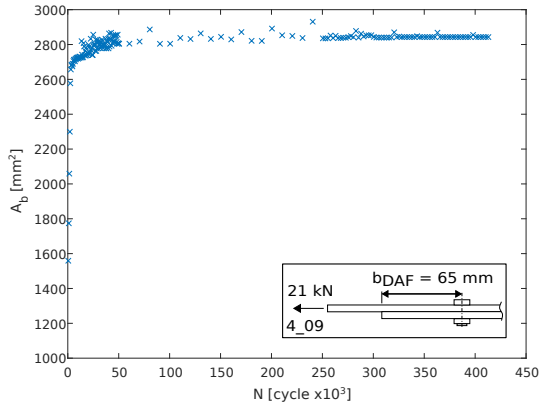

(b) F_{max} = 21 kN and b_{DAF} = 65 mm: (1) BDAF - 4_09.

Figure 5.8: Disbond area - Prepreg bond line specimens.

5.1.3. Adherend Fatigue Damage Observations

The adherends have been inspected for fatigue damages by analyzing the images taken by the visual disbond length inspection camera's, the DIC camera's and by using a micro-USB camera at 20.000 cycle inspection intervals during the fatigue tests. The load cycle number was treated as load cycle at which the damage was visually detectable. An overview of the typical fatigue damage modes, their location and load cycle number of an adhesive bond line specimen with a CDAF and BDAF is shown in fig. 5.9 and fig. 5.10 respectively.

Bolted Disbond Arrest Feature

Figure 5.9 visualizes the results of specimen 2_13. All the initial fatigue cracks appear in the lap adherend in the aluminum ply adjacent to the adhesive interface around the BDAF location on the right side first followed by the left side. The earlier detection on the right probably caused because the right disbond outgrows the left as discussed earlier. A delamination between the cracked aluminum ply and the adjacent prepreg ply initiates at the crack location which propagates rapidly whilst the disbond

front does not seem grow. Shortly after, fatigue cracks start to appear all over the specimen and the fatigue test was stopped to avoid the destruction of valuable information.

Similar behavior was observed in the prepreg specimens except that the fatigue crack at the BDAF would jump upwards through the laminate without initiating a delamination or re-starting the disbond growth. This phenomenon is analyzed in detail in section 7.3.1.

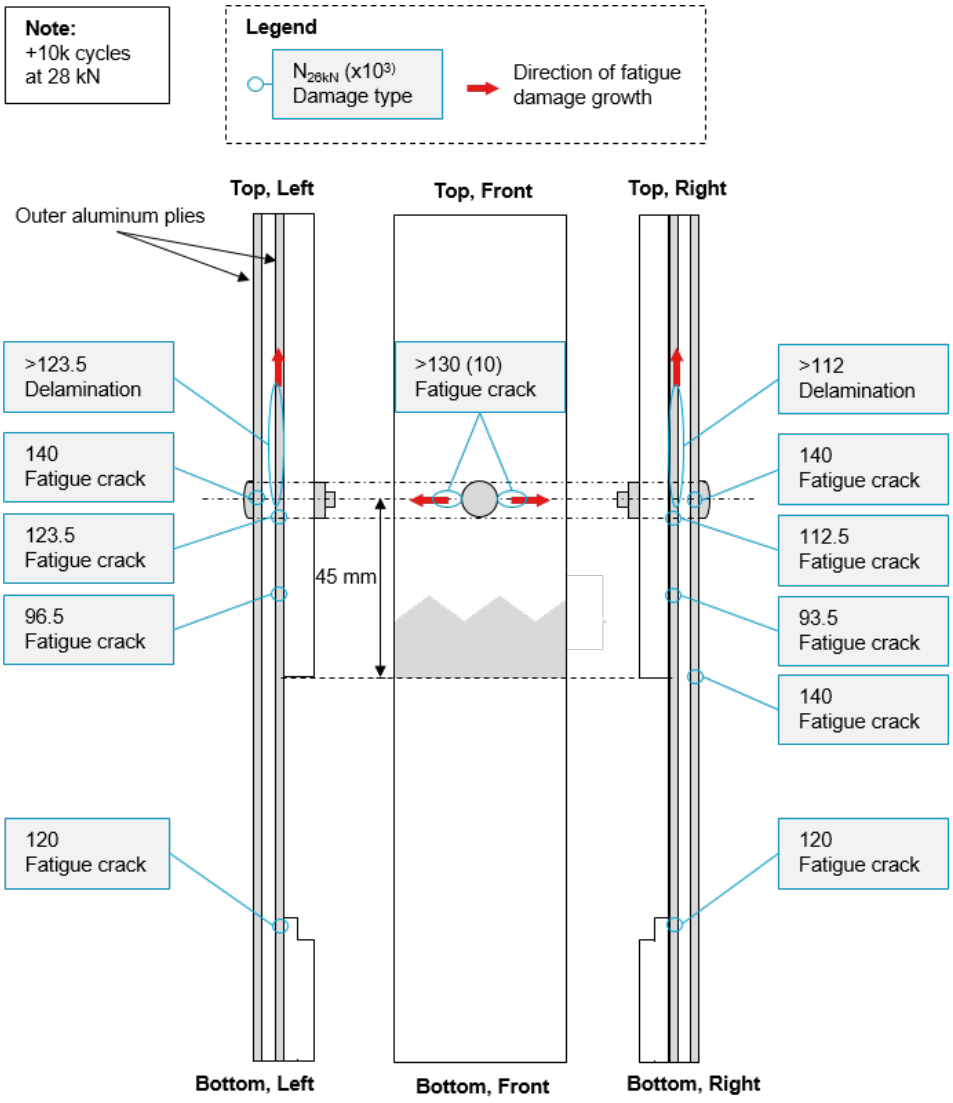

Figure 5.9: Typical adherend fatigue damage mode, locations and the load cycle (x10^3) of detection in an adhesive bondline specimen with a BDAF - specimen 2_13. Note: a maximum fatigue load of 28 kN has been applied for 10,000 cycles for disbond initiation.

Clamped Disbond Arrest Feature

Figure 5.10 visualizes the results of specimen 2_13. Again, the initial fatigue cracks appear in the lap adherend in the aluminum ply adjacent to the adhesive interface around the CDAF location. A fatigue crack is detected on the right side first probably because by the disbond on the right side was outgrowing the left side as discussed earlier. A delamination already starts to grow on the right side originating from the fatigue crack before a fatigue crack is detected on the left side. The test was stopped due to the closing of the faculty before a delamination was detected on the left side as well.

In the prepreg specimen with the CDAF, specimen 4_7, a fatigue crack appears around the CDAF location in the same period as the sudden acceleration of disbond growth. This might be an indication

there can be a relation between the change in disbond growth arrest and the initiation of adherend fatigue damage. This will be further analyzed in section 7.3.2.

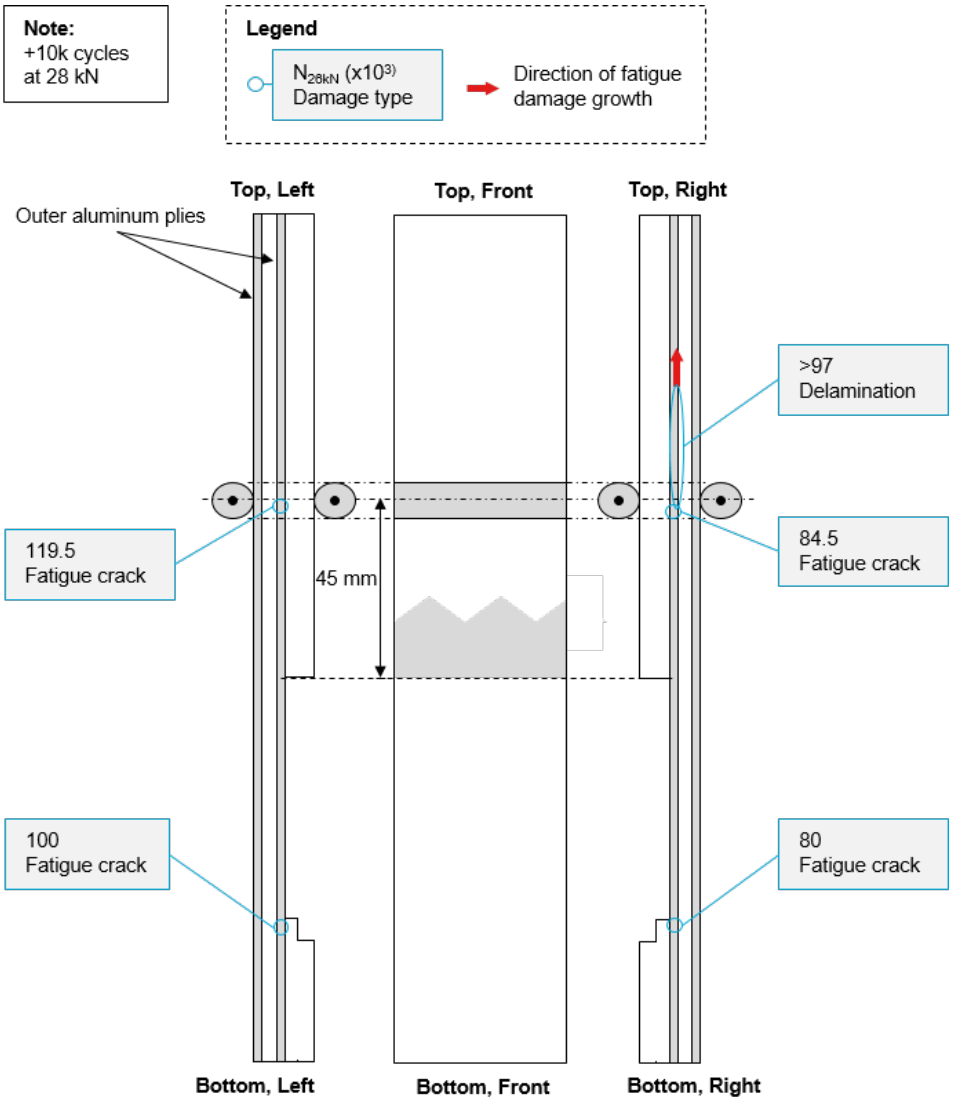

Figure 5.10: Typical adherend fatigue damage modes, locations and the load cycle (x10³) of detection in an adhesive bondline specimen with a CDAF - specimen 2_10. Note: a maximum fatigue load of 28 kN has been applied for 10,000 cycles for disbond initiation.

Summary of the Detected Fatigue Cracks

The fatigue crack of the aluminum ply in the lap adherend adjacent to the bond line represent all the initial adherend fatigue damages. An overview of the the location and load cycle of detection of the fatigue cracks in this ply is given in table 5.1 and table 5.2 for the adhesive and prepreg bond line specimens respectively. The fatigue cracks near the bonded tap are not included as they result from the peak stresses surrounding the support boundary conditions and they were found not to impose an influence on the disbond growth results. No results could be obtained for specimen 4_10 due to unexpected focus problems of the cameras.

An interesting observation is that in the adhesive bond line specimens the fatigue crack coincides with the disbond front position in specimens with a CDAF, but not in any of the specimens with a BDAF. Based on this observations it can already be hypothesized that the disbond front is indeed capable of initiating a fatigue crack. This hypothesis will be further analyzed in chapter 6 and chapter 7.

Table 5.1: Summary of the location and load cycle of the detected aluminum ply fatigue cracks on the left and right side of the adhesive bond line specimens.

Specimen ID	DAF Configuration		Load cycles at 28 kN	Left			Right		
	Type	b_{DAF} [mm]		Load cycles at 26 kN	b_{crack} [mm]	b [mm]	Load cycles at 26 kN	b_{crack} [mm]	b [mm]
2_11	-	-	15,000	107,500	32.24	47.04	93,500	32.19	50.75
2_09	CDAF	35	7,000	54,500	34.48	35.64	60,500	34.29	34.28
2_12	BDAF	35	10,000	70,500	33.68	39.14	68,500	33.58	40.74
2_10	CDAF	45	10,000	119,500	44.36	44.88	84,000	44.26	44.56
2_13 (1/2)	BDAF	45	10,000	96,500	30.70	47.38	93,500	31.90	44.62
2_13 (2/2)	BDAF	45	10,000	123,500	43.08	49.73	112,500	38.24	50.09

Table 5.2: Summary of the location and load cycle of the detected aluminum ply fatigue cracks on the left and right side of the prepreg bond line specimens.

Specimen ID	DAF Configuration		Maximum load [kN]	Left			Right		
	Type	b_{DAF} [mm]		Load cycles at 26 kN	b_{crack} [mm]	b [mm]	Load cycles at 26 kN	b_{crack} [mm]	b [mm]
4_08	-	-	16.5	-	-	-	-	-	-
4_10	BDAF	55	16.5	-	-	-	-	-	-
4_06	BDAF	40	19.5	201,000	39.24	51.85	175,500	38.67	54.02
4_09	BDAF	65	21	400,000	65.79	85.45	370,000	66.94	89.17
4_07	CDAF	55	19.5	603,500	54.56	81.58	-	-	-

5.2. Verification

A high level verification of the SERR Footprint Model and the Disbond Growth Model has been performed of the most important calculated outputs to ensure their correctness. Both models are thoroughly explained in section 4.2 and section 4.3 respectively. The SERR Footprint Model predicts the effect of the CDAF on the SERR so the SERR calculations will have to be verified. The Disbond Growth Model predicts the disbond growth and the location and load cycle of fatigue crack initiation for a given DAF configuration. These calculations rely heavily on the SERR and ply stress cycles so both these outputs will have to be verfied.

Additionally, analyzing the SERR and strain distributions provides a very powerful opportunity to deepen the understanding of the driving forces for disbond growth and the fatigue crack initiation behavior; both of which are key aspects of the research objectives.

The verification of both models will be performed in three steps;

1. The calculated SERR of the SERR Footprint Model is verified using results from the literature without a DAF. No reference solutions were found including a DAF so this verification cannot be performed
2. The verified SERR calculations of the SERR Footprint Model are used to verify the SERR calculated by the Disbond Growth Model
3. The calculations of the strain cycle in top and bottom aluminum ply of the lap adherend is verified using the SERR Footprint Model. This step assumes a verified calculation of the strain cycles by the SERR Footprint Model

The verification of the Strain Energy Release Rate Footprint Model is discussed first followed by the Disbond Growth Model.

5.2.1. SERR Footprint Model (FEM)

Verification data for the SERR calculations were obtained from Johnson [15] where various institutes have provided the SERR and Mode Ratio (MR) calculations at a range of disbond lengths of a CLS specimen with identical adherends. Only the results of Dattagure et al. and Everett have been selected

because both provide a geometric non-linear 2D FEM solution for the CLS specimen with identical adherends. The result of the comparison are shown here and the reader is referred to [15] for the model inputs and descriptions of the solutions proposed by Dattagure et al. and Everett. No results were available for clamped-clamped support boundary conditions; only roller-roller.

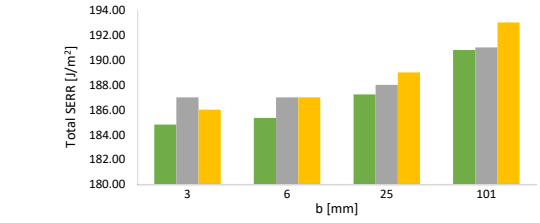

SERR Footprint Model	184.81	185.35	187.23	190.80
B. Dattaguru et al.	187	187	188	191
R. A. Everett	186	187	189	193

(a) Total SERR G

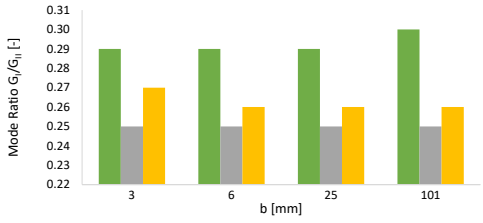

SERR Footprint Model	0.29	0.29	0.29	0.30
B. Dattaguru et al.	0.25	0.25	0.25	0.25
R. A. Everett	0.27	0.26	0.26	0.26

(b) Mode Ratio G_I/G_{II}

Figure 5.11: SERR Footprint Model verification - SERR and MR calculations.

The total SERR and the MR, defined at $MR = G_I/G_{II}$, results are compared in fig. 5.11(a) and fig. 5.11(b) respectively at the disbond positions of 3, 6, 25 and 101 mm measured from the overlap edge. The comparison show that there is a good match between the total SERR results, but the SERR Footprint Model consistently over predicts G_I/G_{II}. This implies that the Mode I component is larger than the reference results.

It is not clear what causes the difference in the values of G_I/G_{II}. All three solutions deploy the VCCT and a mesh refinement in the SERR Footprint Model did not solve the issue. Additionally, it is difficult to say which of the solutions truly is correct. It was decided to accept the differences given the need for a simplistic modeling approach to study the general trends; not to provide accurate predictions. Another uncertainty is that no verification could be performed for the clamped-clamped support boundary conditions which will be applied during fatigue testing.

5.2.2. Disbond Growth Model (MATLAB)

The SERR Footprint Model will be used here to verify the SERR calculations of the Disbond Growth Model. Additionally, the SERR Footprint Model is used to verify the strain field calculations.

Strain Energy Release rate

The SERR has been calculated using the batch 2 geometry from table 4.1, the selected GLARE 2A-4/3-0.4 grade layup and the ply material properties from table 4.2 and table 4.3. Plane stress has been assumed in the width direction of the CLS specimen and clamped-clamped support boundary conditions have been applied. The SERR as a function of disbond length calculated by the SERR Footprint Model and the Disbond Growth Model are shown in fig. 5.12(a) and fig. 5.12(b) for a maximum fatigue load of 2.6 kN and 30 kN respectively.

A very good match exists between both models for all SERR components at F_{max} = 2.6 kN. At F_{max} = 30 kN however, the SERR Footprint Model shows a higher Mode I and a lower Mode II component which was also observed when the calculated G_I/G_{II} was higher compared to the reference solutions from [15]. These differences were not further investigated and the SERR calculations by the Disbond Growth Model were accepted.

Two interesting observations can be made regarding the SERR distributions. First, the Mode I and Mode II component are constant for a significant portion of the disbond length for F_{max} = 30 kN which is in agreement with the expected behavior of the CLS specimen. Secondly, at 2.6 kN the constant SERR conditions do not exist because the geometric non-linearity has a lower effect which is needed to achieve the constant SERR conditions.

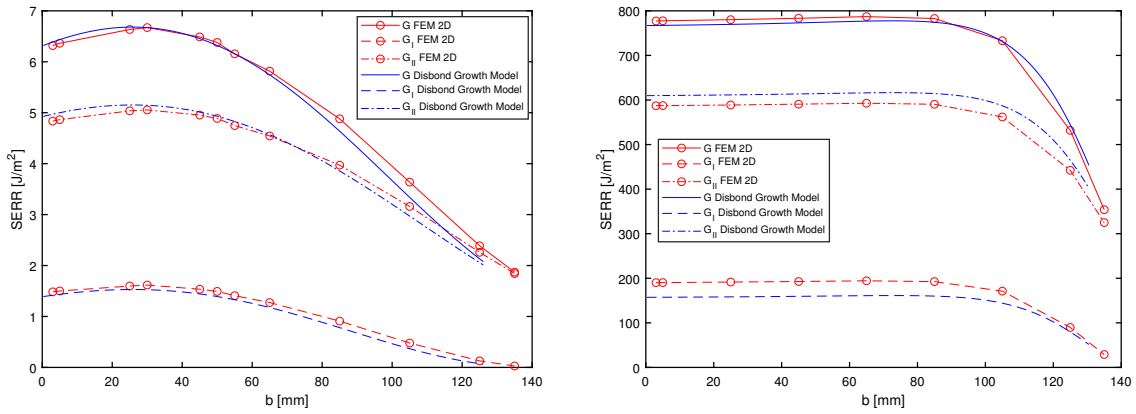

(a) Maximum fatigue load F_{max} = 2.6 kN

(b) Maximum fatigue load F_{max} = 30 kN

Figure 5.12: Disbond Growth Model verification - SERR Mode I G_I, Mode II G_{II} and total G components.

Strain Field

The strain fields in the top and bottom ply of the lap adherend are calculated using the same inputs as the verification of the SERR calculations and no residual strains are included. The results are shown in fig. 5.13(a) and fig. 5.13(b) for a maximum fatigue load of 2.6 kN and 30 kN respectively. There is a very good match between the results of both models for the top and bottom ply in the free adherend section. The SERR Footprint Model shows a higher peak strain value in the bottom ply, but this is likely due to the stress singularity near the stiffness step around the overlap edge.

The models do not match in the overlap region because the load transfer from the lap to the strap adherend in the Disbond Growth Model is calculated using the adhesive stress solution of [82]. It was discussed in section 4.2.3 that [82] ignores the geometric non-linearity in the overlap region and that it is only valid for a CLS specimen with roller-roller support boundary conditions. The curve of both models has a more similar shape F_{max} = 2.6 kN as the geometric non-linear effect is low at these loads.

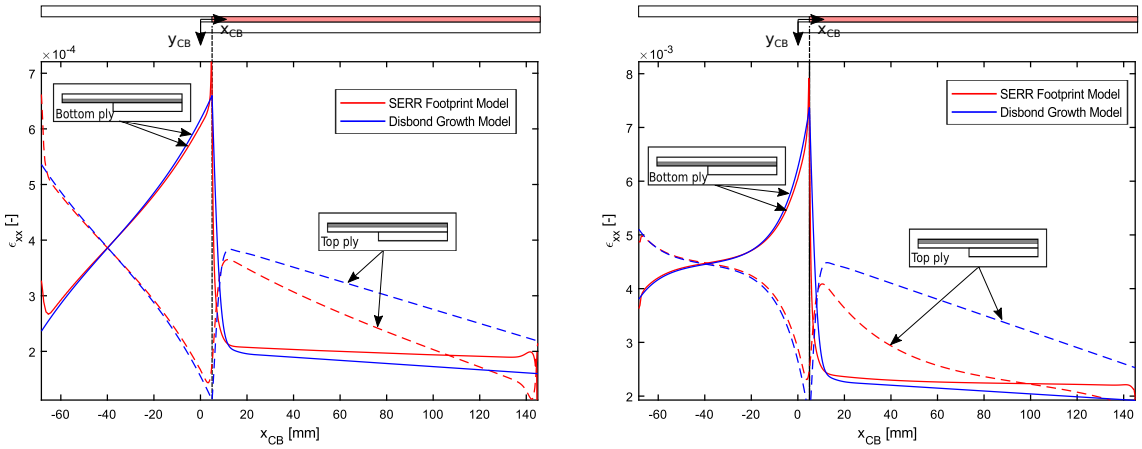

(a) Maximum fatigue load F_{max} = 2.6 kN

(b) Maximum fatigue load F_{max} = 30 kN

Figure 5.13: Disbond Growth Model verification - Strain field calculations in the top and bottom ply of the lap adherend.

Summarized, the SERR calculations by the SERR Footprint have been verified, although only for roller-roller support boundary conditions and there is a constant over and under prediction of the Mode I and Mode II SERR components respectively. Furthermore, the SERR calculations of the disbond growth model show a very good match with the SERR Footprint Model. The strain distributions in the top and bottom ply of the lap adherend show a very good and a poor match between both models in the free adherend section and overlap region respectively.

6

SERR Footprint of a Clamp as Disbond Arrest Feature

The literature review showed that the Status-Quo agrees that the reduction of Mode I is the main driver for achieving the arrest of disbond growth [2, 3, 5, 6]. In reality however, the isolated effect of Mode I reduction is not known as disbond growth arrest has only been investigated using bolted Disbond Arrest Features (DAF) which influence both Mode I and Mode II. To fill this knowledge gap, a Clamped Disbond Arrest Feature (CDAF) has been developed and produced with the aim to study the isolated effect of Mode I reduction on disbond growth. The effect of the CDAF on the Strain Energy Release Rate (SERR), referred to in this report as the SERR footprint, must be known to confirm the isolated effect of Mode I reduction and to ensure a correct interpretation of the experimental results. Also, the SERR footprint will be provided as an input to the disbond growth model.

This chapter details the analysis of the CDAF SERR footprint. To be more specific; it will be investigated if the SERR footprint of the CDAF is depended on the maximum fatigue load first and on the applied clamping pressure of the CDAF second. The findings from both analyses will be used to derive a mathematical expression for the CDAF SERR footprint. Finally, a final synthesis of the chapter is given. Before discussing the analysis topics, the model inputs will be summarized.

6.1. Model Inputs

The 2D FEM model detailed in section 4.3 was used with the batch 2 specimen geometry and the FML layup and ply materials given in section 4.1.1 as input. The CDAF was placed at b_{DAF} = 50 mm and clamped-clamped support boundary conditions were applied.

The tensile load F_{max} was varied between at 28 kN, 26 kN, 22 kN and 2.6 kN based on the planned fatigue load cycles for testing the adhesive bondline specimens. Only the minimum tensile load of 2.6 kN is evaluated as little difference in the behavior is expected at low loads.

The clamping pressure P_{clamp} was varied between 0 MPa, 10 MPa and 100 MPa. 0 MPa represents the absence of the CDAF, 100 MPa matches the pressure exerted by the Hi-Lok fastener head of the BDAF (see appendix D) and 10 MPa was selected as an intermediate step.

6.2. Effect of the Clamping Pressure

Figure 6.1 shows the SERR as a function of disbond length at a varying clamping pressure and a constant tensile load. Only the results of F_{max} = 26 kN are shown here as the results were similar for all analyzed loads.

Based on fig. 6.1, several observations can be made;

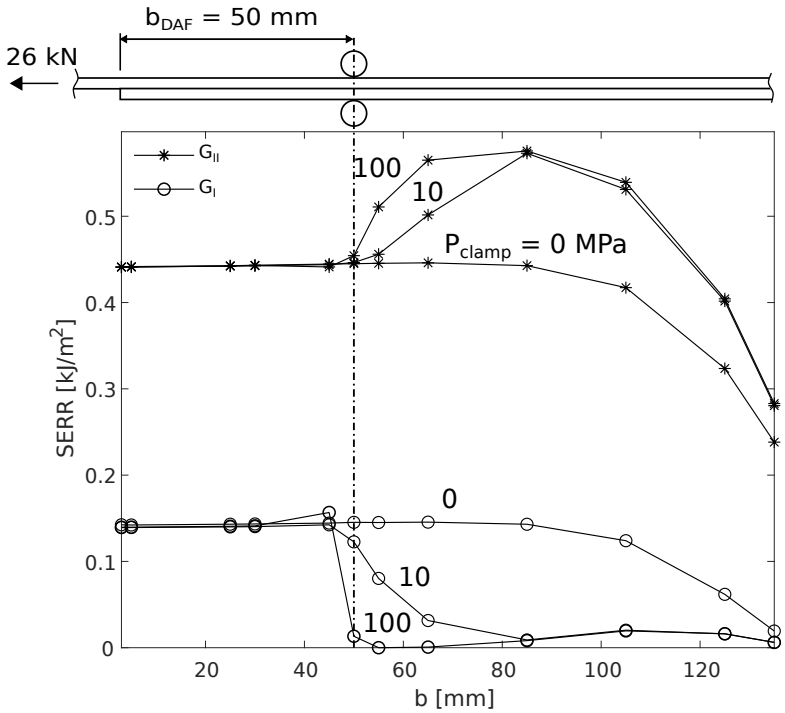

Figure 6.1: The effect of the clamping pressure P_{clamp} on the SERR as a function of disbond length with a maximum fatigue load F_{max} of 26 kN. Note: P_{clamp} is illustrated in fig. 4.20.

- Mode I is reduced and the level of reduction increases with a higher clamping pressure resulting in a complete Mode I elimination at P_{clamp} = 100 MPa
- Mode II is increased and the level of increase is proportional to the clamping pressure
- The reduction of Mode I starts just before the CDAF position and has steeper slope compared to the Mode II increase which starts roughly at the CDAF location
- The Mode I and Mode II values at P_{clamp} = 100 MPa and P_{clamp} = 10 MPa seem to converge after the 80 mark
- Mode I experiences a slight increase just in front of the CDAF before its starts to decrease and the effect seems to be proportional to the applied clamping pressure

The observed increase of Mode II is important because it is opposite to the intended arresting behavior of a DAF and has never been reported in the literature. It also questions the suitability of the CDAF to purely represent an isolated Mode I effect. Luckily, this only seems to be an issue in the region after the CDAF as the region before the CDAF only shows to affect Mode I. However, it is important to be aware of this effect when evaluating the experimental DGR results.

Mode II is thought to be increased by the additional relative sliding at the disbond front that is created when the disbonded portion of the strap adherent is compressed against the lap adherent once the disbond has passed the CDAF. In reality, this additional sliding movement is resisted by friction loads between the disbonded surfaces and by the friction loads between the CDAF and the adherent surfaces. As both are not included into the current FEM model, it is expected that the increase of Mode II will be smaller in reality, but this was not further investigated.

The increased magnitude and gradient of the Mode I and Mode II effect at a higher clamping pressure is related to the increased internal bending moments in the adherents at the location of the disbond front. Also, as the disbond grows beyond the CDAF, the internal bending moments around the disbond front increase resulting in a larger reduction and increase of Mode I and Mode II respectively.

The observed convergence of Mode I and Mode II after the 80 mark is believed to be an effect of the support boundary conditions.

The increase in mode I in front of the CDAF cannot be explained. Initially it was thought to be a meshing issue, but mesh refinement did not solve the issue. It was decided to not further pursue the root cause and to accept the behavior as an uncertainty.

6.3. Effect of the Maximum Fatigue Load

It has been determined that the effect of the CDAF on the SERR depends on the clamping pressure. A convenient way to visualize the effect of the CDAF is to calculate the reduction in SERR provided by the CDAF and normalize it by the SERR expected without a CDAF using eq. (6.1);

$$G_{\%}(b) = \frac{G(b) - G_{CDAF}(b)}{G(b)} \tag{6.1}$$

where $G_{\%}(b)$ is the SERR footprint, $G(b)$ and $G_{CDAF}(b)$ are the SERR as a function of the disbond length b without and with a CDAF respectively. Note that G in this equation does not represent the total SERR like it commonly does in the literature, but the total Mode I or Mode II SERR component.

The resulting SERR footprints are shown in fig. 6.2 as a function of disbond length at different maximum fatigue loads and a single clamping pressure of P_{clamp} = 100 MPa. Only the results of P_{clamp} = 100 MPa are shown because similar behavior was observed for P_{clamp} = 10 MPa. Also, P_{clamp} = 100 MPa is representative for the clamping pressure applied by the CDAF during fatigue testing (see appendix D).

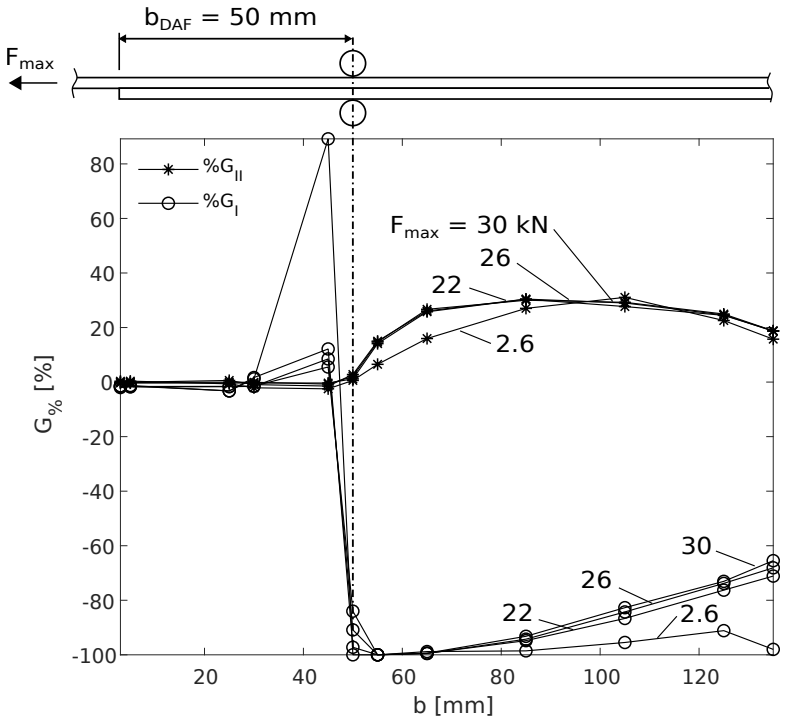

Figure 6.2: The effect of the maximum fatigue load F_{max} on the SERR footprint for Mode I $G_{\%,I}$ and Mode II $G_{\%,II}$ as a function of disbond length at a clamping pressure P_{clamp} of 100 MPa. Note: P_{clamp} is illustrated in fig. 4.20.

Based on fig. 6.2, the following observations can be made regarding the effect of the maximum fatigue load on the SERR footprint of the CDAF;

- The SERR footprint is largely independent of the maximum fatigue load at in the range of 22-28 kN
- The lowest load of 2.6 kN shows a more effective elimination of Mode I, a smaller and percentile increase of Mode II and larger percentile increase of Mode I in front of the CDAF

The difference in the effect at a maximum fatigue load of 2.6 kN and the range of 22-30 kN could be related to the geometric non-linear behavior of the CLS specimen which is known to stabilize at higher loads [85]. This was not further investigated as a general expression for the SERR footprint based on the 22-30 kN maximum fatigue load range will lead to only minor discrepancies when calculating the SERR of the CDAF at the minimum fatigue loads.

6.4. Formulation of the SERR Footprint

It has been concluded that the SERR at a fixed clamping pressure is fairly independent of the maximum fatigue load. Therefore, the SERR as a function of disbond length b under the influence of a CDAF G_{CDAF} at a fixed P_{clamp} can be found simply by;

$$G_{CDAF}(b) = G(b)\left(1 + G_{\%}(b)\right) \tag{6.2}$$

where G_{DAF} is the total Mode I or Mode II SERR component without a DAF and $G_{\%}(b)$ is the SERR footprint at a given clamping pressure from eq. (6.1).

6.5. Synthesis and Hypothesis Evaluation

The analysis of the current section aimed to provide an understanding of the effect of the CDAF on the SERR and to formulate the SERR footprint which is to be used as an input for the disbond growth predictions. By synthesizing the analysis, the following is concluded:

1. It has been shown that in front of the CDAF an isolated Mode I reduction exists, but beyond the CDAF the effect is a mix of Mode I reduction and Mode II increase
2. The SERR footprint is heavily dependent on the applied clamping pressure
3. Mode I is completely eliminated at a clamping pressure of 100 MPa
4. The SERR footprint is independent of the maximum fatigue load in the range of 22-30 kN at a fixed clamping pressure
5. A normalized expression of the SERR footprint has been derived which is given by eq. (6.2)

There are two important limitations to the current analysis. First, friction is not included which has been named by other studies as the second most import mechanism for arresting quasi static growth [2]. Second, the 2D analysis cannot account for the Mode III SERR component which has been demonstrated to exist near the specimen edges [3].

7

Cracked Lap Shear Experimental Analysis

To generate the information required to achieve the research objective detailed in section 3.2, fatigue experiments have been performed using Cracked Lap Shear (CLS) specimens with a Clamped Disbond Arrest Feature (CDAF) and a Bolted Disbond Arrest Feature (BDAF). The results of these experiments have been presented in section 5.1 and include the disbond length, disbond area, disbond shape and the location of the detected fatigue cracks combined with the load cycle number at the crack appearance. This chapter will further analyze these results to contribute to the research objective.

First, the conditions necessary for arrest will be studied. This is done by analyzing the experimental Disbond Growth Rate (DGR) results of the CDAF specimens to study the effectiveness of reducing Mode I. Additionally, a qualitative assessment of the relevance of reducing Mode II will be given. Second, the conditions provided by a BDAF for arrest are evaluated using the calculated DGR and Disbond Area Growth Rate (DAGR) results of the BDAF specimens. Third, all specimens are used to study if adherend fatigue damages can be responsible for re-starting the growth of an arrested disbond. Fourth, the CDAF specimens are analyzed to see if an arrested disbond can initiate a fatigue crack. Fifth, a discussion is given on the limited ability to extrapolate the analysis of this chapter, which is based on the CLS specimen, to a realistic structural bonded joint. Finally, the chapter is synthesized and the hypotheses evaluated.

7.1. Conditions Necessary for Arrest

The disbond length results of the specimens with a CDAF have given a first indication that the arrest of disbond growth was achieved in the direct proximity of the CDAF centerline. Furthermore, analysis of the CDAF SERR Footprint has confirmed that, in theory and when friction is ignored, an isolated Mode I effect exists in front of the CDAF centerline. Combined, these observations give a first indication that Mode I reduction is a very effective driver for the arrest of disbond growth. However, the DGR must be calculated and evaluated to confirm the that arrest has occurred. This will be done in the first part of the analysis for both the adhesive and prepreg bond line specimens.

Although Mode I is the focus of the experimental analysis of the conditions necessary for arrest, Mode II cannot be ignored. Therefore, a qualitative assessment will be given on the contribution of Mode II reduction to the arrest of disbond growth in the second part of the analysis.

7.1.1. Mode I

The average DGR, $(db/dN)_{ave}$, has been calculated with the average disbond length results from section 5.1.1 and the calculation procedure discussed in section 4.1.4.

Adhesive Bond Line Specimens

The original disbond length results of the adhesive bond line specimens were adjusted before processing. First, the data points corresponding to a maximum fatigue load of 28 kN were removed. Second, the sampling rate was reduced from 1000 to a 2000 cycles per data point to average out the measurement noise.

The results of the specimens without and with the CDAF have been plotted in fig. 7.1 against the disbond position centered around the CDAF. Based on fig. 7.1, the following observations can be made:

- Specimen 2_11 continues a constant DGR trend
- Specimen 2_09 and 2_10 clearly show an aggressive decrease of the DGR with respect to specimen 2_11 and both curves end in what seems to be a vertical assymptote in front of the CDAF
- The disbond growth in specimen 2_09 seems to only have occurred in the region of influence of the CDAF
- Specimen 2_09 shows a single data point with a very high DGR value

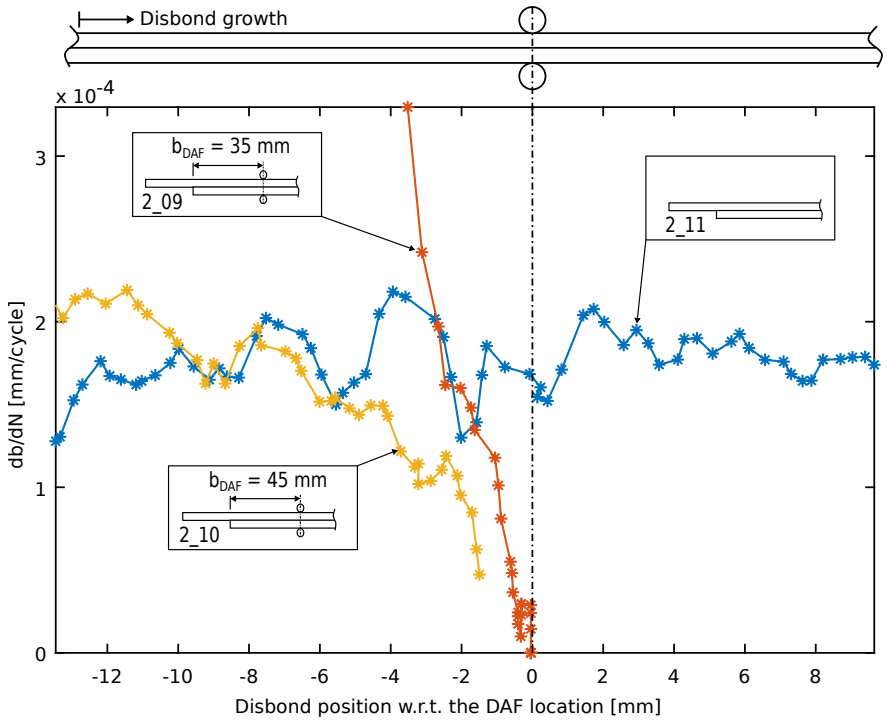

Figure 7.1: Average DGR $(db/dN)_{ave}$ results of the adhesive bond line CDAF specimens: (1) F_{max} = 26 kN, no DAF - 2_11, (2) F_{max} = 26 kN, CDAF, b_{DAF} = 35 mm - 2_09 and (3) F_{max} = 26 kN, CDAF, b_{DAF} = 45 mm - 2_10.

The single peak value in the results of specimen 2_09 cannot be fully explained. One could argue that the disbond initiation loading step at 28 kN could have caused micro cracking ahead of the disbond front therefore lowering its resistance to disbond growth, but this cannot be measured nor confirmed.

The constant DGR without a CDAF is in agreement with the expected behavior of the CLS specimen. The rapid decrease of the DGR and the vertical assymptote confirm the hypothesis that disbond growth has been arrested. It is not possible however, to say how long the arrest would have existed due to the early failure of the adherends in fatigue. The question that remains is what portion of this arrest can be attributed to the effect of eliminating Mode I and not Mode II. This question will be addressed with a qualitative analysis in section 7.1.2.

Prepreg Bond Line Specimens

The DGR results of the specimen with a CDAF is shown in fig. 7.2. No result of specimen without a DAF is included as this was not available for this particular load level. Based on fig. 7.2, the following observations can be made:

- Arrest occurs just behind the CDAF centerline which is indicated by the vertical drop of the DGR
- After a period of full arrest, disbond growth continues at a low and constant DGR
- After a period of growth at a constant DGR, disbond growth starts to accelerate more rapidly

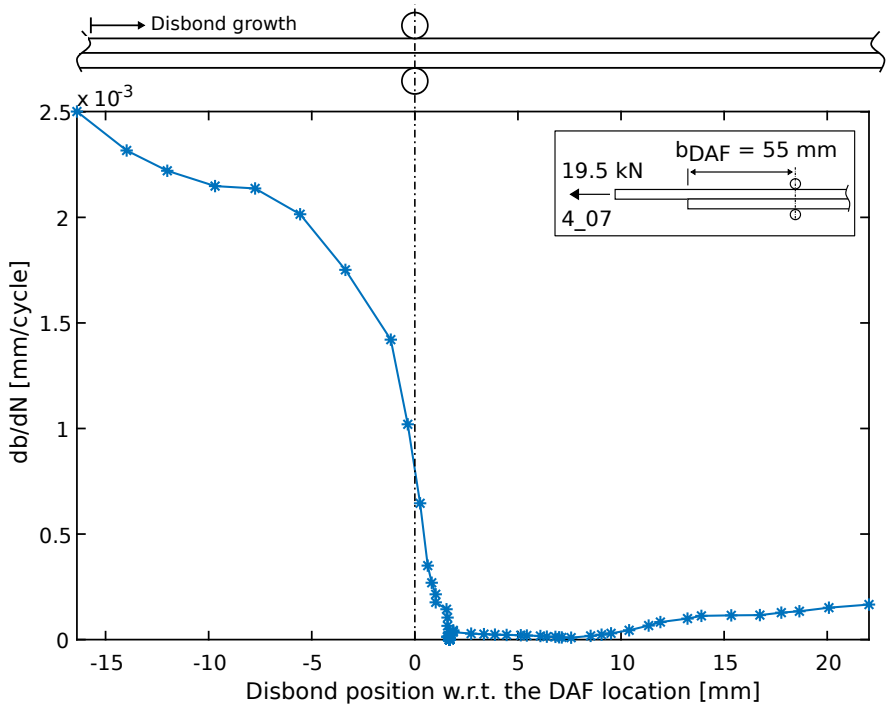

Figure 7.2: Average DGR $(db/dN)_{ave}$ results of the prepreg bond line specimens with a CDAF: (1) F_{max} = 19.5 kN, CDAF, b_{DAF} = 55 mm - 4_07.

The aggressive decrease of the DGR to zero confirms the hypothesis that the disbond growth has been arrested although this time the arrest has only been temporarily.

Understanding the re-start of the disbond growth is important because it highlights a change in the SERR conditions. Additionally, the sudden, more rapid increase of the DGR is undesirable from a damage tolerance perspective and might indicate the need for an inclusion of Mode II reduction. Three mechanisms are considered as possible root causes for the sudden increase of the DGR:

1. The reduction of Mode II by friction between the disbond surfaces can be significant [2, 6]. However, the surface roughness will decrease over time by the cyclic sliding of both adherends. This could create a sudden increase in Mode II leading to an increase in the DGR
2. The analysis of the CDAF SERR Footprint in chapter 6 indicated that Mode II is increased behind the CDAF which could lead to higher DGRs
3. A fatigue crack has been observed in the aluminum ply on the right side of the specimen (see table 5.2) in the same period that the DGR starts to increase

The third mechanism is in line with the hypothesis that adherend fatigue damage has a reversing effect on the arresting behavior, but it will be confirmed in section 7.3.2 that this was not the case. The first and second mechanism are both related to the role of Mode II and will be discussed next in section 7.1.2.

7.1.2. Mode II

The CDAF SERR Footprint has shown that Mode I is eliminated underneath the clamp resulting in pure Mode II disbond growth beyond the CDAF. That directly implies that full arrest can only exist if Mode II is reduced. Another option is that Mode II is lower than the Mode II threshold below which no disbond growth occurs in the bond line material; if it exists.

It was not possible to confirm that such a lower threshold exists in the FM94 adhesive film as no documentation was found in the literature. It is also not possible to confirm that the threshold does not exist. This is because the value of the SERR fracture parameter $G_{eq,1}$ at the CDAF location lies outside the Mode II fracture data of the FM94 adhesive in [8]. Experimental fatigue tests will have to be performed to see if the threshold really exists, but that is outside the scope of this research.

Friction has been called the second most important driver for arrest in static [2] and fatigue [6] disbond growth. Furthermore, [39] observed both experimentally and numerically that an interaction exists between the friction and clamping load of a BDAF that locks the disbond front into its place underneath the fastener head. This interaction however, was not further investigated and remains ill-understood.

Concluding, the arrest during pure Mode II growth implies a reduction of Mode II and/or the existence of a lower fatigue threshold in the bond line material. Both theories could not be confirmed nor eliminated, but they do give a strong indication that Mode II cannot be ignored when evaluating the CDAF results.

7.2. Conditions Provided by a Bolt as DAF

The disbond length results of the adhesive bond line BDAF specimens resulted in the hypothesis that little to no retardation had occurred which was contradicted by the disbond area results. Both the disbond length and area results of the prepreg bond line specimens showed a drastic retardation of disbond growth. Similar to the CDAF however, the DGR must be analyzed to confirm the level of disbond growth retardation/arrest. This will be done for the adhesive and prepreg bond line specimens in the first part of this analysis.

The second part of the analysis will assess the DAGR because the disbond length alone cannot describe the disbonded region growing around the BDAF. Only the DAGR of the adhesive bond line specimens will be analyzed and not the prepreg bond line specimens. The disbond length, area and DGR results are convincing enough to confirm the level of retardation in the prepreg bond line specimens, but this will be discussed throughout the section.

The third part of the analysis is a qualitative assessment of the conditions for arrest provided by a BDAF using the CDAF as a benchmark.

7.2.1. Disbond Growth Rate

The DGR of the adhesive and prepreg bond line specimens has been calculated using the disbond length results summarized in section 5.1.1 and the procedure described in section 4.1.4.

Adhesive Bond Line Specimens

Before processing, the same adjustments were made to the disbond length results as was done with the CDAF. The data points corresponding to F_{max} = 28 kN have been removed and a sampling rate of 2000 cycles per data point was used.

The results are shown in fig. 7.3(a) and a lower DGR can be seen for both specimens although this is more difficult to observe for specimen 2_13 due to the noise. Furthermore, when placed at 35 mm, disbond growth only seems to have occurred in the region of influence of the BDAF similar to the analysis of the CDAF. Based on the earlier experience with the disbond length and area results, it is expected that the DAGR analysis in section 7.2.2 will be more conclusive about the level of retardation that has occurred.

Prepreg Bond Line Specimens

The DGR results of the prepreg bond line specimens with a BDAF are shown in fig. 7.3(b). It can be confirmed that very slow growth has been achieved at all load levels and that the maximum arrest occurs behind the centerline of the BDAF. Arrest will occur further away from the CDAF centerline with an increasing loads. The arresting behavior will be discussed in more detail in section 7.2.3.

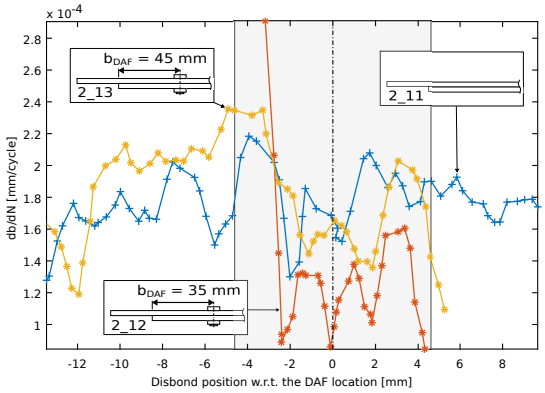

(a) Adhesive bond line specimens: (1) F_{max} = 26 kN, no DAF - 2_11, (2) F_{max} = 26 kN, BDAF, b_{DAF} = 35 mm - 2_12 and (3) F_{max} = 26 kN, BDAF, b_{DAF} = 45 mm - 2_13.

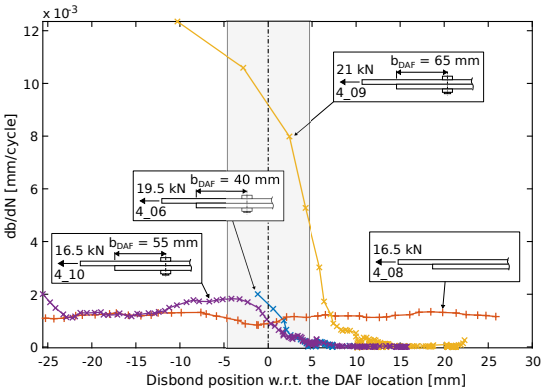

(b) Prepreg bond line specimens: (1) F_{max} = 16.5 kN, no DAF - 4_08, (2) F_{max} = 16.5 kN, BDAF, b_{DAF} = 40 mm - 4_10, (3) F_{max} = 19.5 kN, BDAF, b_{DAF} = 55 mm - 4_06 and (4) F_{max} = 21 kN, BDAF, b_{DAF} = 65 kN - 4_09.

Figure 7.3: Average DGR $(db/dN)_{ave}$ results of the BDAF specimens.

7.2.2. Disbond Area Growth Rate

Based on the disbond length, area and DGR of the adhesive bondline specimens with a BDAF, the level of disbond growth retardation is not conclusive. Therefore, the DAGR has been calculated using the same procedure and sampling rate as the DGR results and are plotted in fig. 7.4(a) and fig. 7.4(b) for the BDAF placed at 35 and 45 mm respectively.

The results show that when placed at 35 mm, the BDAF has resulted in a consistently lower DAGR which is in line with earlier speculations that disbond growth has only occurred in the region of influence of the BDAF. Placed at 45 mm, a gradual, but significant decrease in the DAGR is observed which gives the first strong indication that disbond growth retardation did occur. The local peak DAGR value in the results of both DAF positions is related to noise in the DIC processing algorithm.

Based on the combined analysis of the disbond length, area, DGR and DAGR it is concluded that retardation of the disbond growth has occurred at both positions of the BDAF, but that its complete behavior cannot be studied due to the early onset of adherend fatigue damage initiation.

7.2.3. Evaluation of the Conditions Provided by a Bolt as DAF

It has been demonstrated that Mode I elimination is extremely effective in arresting disbond growth. It is therefore interesting to assess the ability of a BDAF to eliminate Mode I and to what extend it relies on the reduction of Mode II. Such an assessment is performed here on qualitative level by comparing the conditions provided for arrest by a BDAF to those provided by a CDAF. Originally it was planned to create a 3D FEM model to study the BDAF SERR footprint, but this was not finished due to time constraints.

A comparison of the DGR result of the prepreg bond line specimens with a CDAF and BDAF, both loaded at F_{max} = 19.5 kN, is shown in fig. 7.5(a). Two key differences are highlighted. For the BDAF, the maximum arrest exists further away from the DAF centerline and the transition to the region of 'slow growth' is much more gradual. These differences are directly related to the conditions provided for arrest by the CDAF and BDAF as will be explained.

Consider the disbond front spanning across the width of the CLS specimen as has been illustrated in

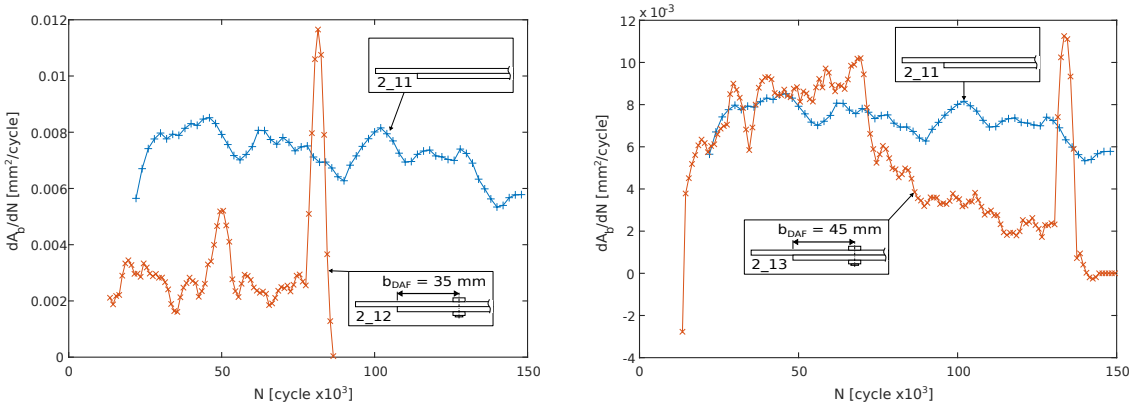

(a) F_{max} = 26 kN and b_{DAF} = 35 mm: (1) No DAF - 2_11 and (2) BDAF - 2_12.

(b) F_{max} = 26 kN and b_{DAF} = 45 mm: (1) No DAF - 2_11 and (2) BDAF - 2_13.

Figure 7.4: DAGR (dA_b/dN) results of the adhesive bond line specimens with and without a BDAF.

fig. 7.5(b). The CDAF creates a continuous Mode I elimination by the clamping load. This results in an abrupt transition from a MM to a pure Mode II disbond growth along the width of the disbond front. In contrast, the discrete clamping pressure of the BDAF will create a Mode I reduction that decreases in magnitude towards the specimen edges along the disbond front in the x_{BDAF} direction. As a result, the disbond growth retardation varies and is higher in the center of the disbond front, but lower near the edges resulting in the 'V' shaped growth around the BDAF.

After surpassing the BDAF, arrest of the outer regions of the disbond front can only occur by further reducing Mode I and/or Mode II. The CDAF SERR footprint analysis demonstrated that the Mode I reduction by a clamping pressure increases as the disbond grows beyond the CDAF position, but it is unknown if a bolt would behave the same. Mode II reduction by bolt shear engagement has been found to increase as the disbond grows beyond the BDAF due to the increased relative sliding of the adherends [2, 6]. Assuming both mechanisms to be true, the increase of their effect with an increase of disbond length would explain the gradual transition to the slow growth region observed in fig. 7.5(a).

Relying on the reduction of Mode II might pose a few problems. First, the fatigue loads are not always high enough to achieve the bolt engagement needed for arrest, especially if a radial clearance exists [6]. Second, friction is very difficult and unreliable to predict and the surface roughness can decrease over time. It is therefore important in the future to understand to what extent the arrest of disbond growth is reliant on the reduction of Mode II and how it can be provided. The relative effectiveness and importance of reducing Mode I and Mode II will be further investigated in section 8.3.1 and section 8.3.2.

Based on these findings it is carefully hypothesized that a bolt as DAF is not effective in extending the Mode I elimination outwards and that Mode II reduction might be needed. However, without a numerical SERR footprint analysis it is not possible to draw any firm conclusion.

7.3. Effect of Adherend Fatigue Damage on Growth Arrest

It has been hypothesized in section 3.2 that the initiation of adherend fatigue damages will re-start the growth of a disbond that has been arrested by a DAF. To evaluate this hypothesis, the adherends were visually inspected for fatigue damages using a micro-USB camera and by analyzing the images taken to measure the disbond length. The results, presented in section 5.1.3, must be analyzed for the type for damage modes and their relation to any changes in the disbond growth behavior. The prepreg bond line specimen with a CDAF, specimen 4_7, will be analyzed separately. This is because it is the only specimen that showed a sudden increase of the DGR after a long period of steady disbond growth retardation.

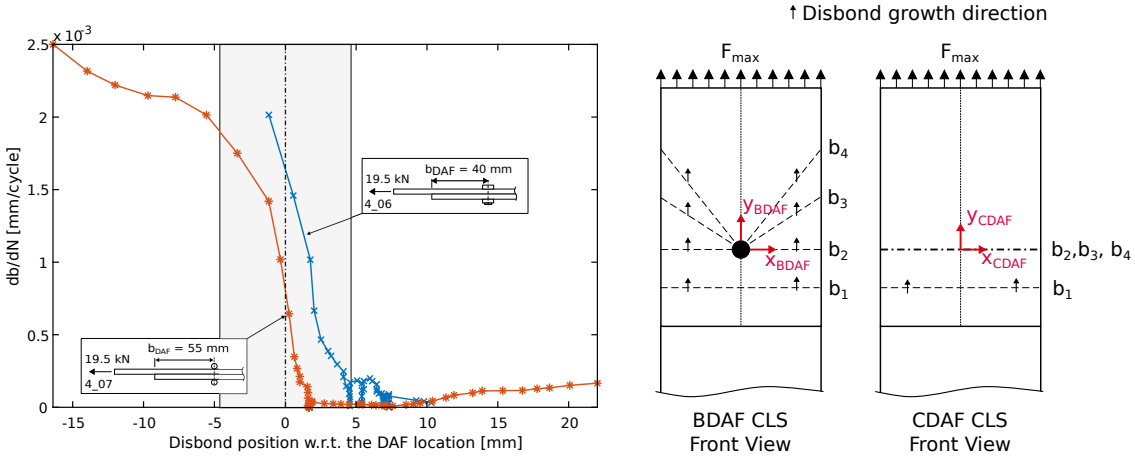

(a) Average DGR $(db/dN)_{ave}$ results: (1) F_{max} = 16.5 kN, CDAF, b_{DAF} = 55 mm - 4_06 and (2) F_{max} = 16.5 kN, BDAF, b_{DAF} = 40 mm - 4_07.

(b) Illustration of the disbond front development.

Figure 7.5: Comparison between the disbond growth behavior of a BDAF and a CDAF in a prepreg bond line specimen.

7.3.1. Observed Fatigue Damage Modes and DGR Response

The results have shown differences between the adhesive and the prepreg bond line specimens which will be highlighted in a timeline of the adherend fatigue damage observations.

Adhesive Bond Line Specimens

The timeline of adhesive bondline specimen with a CDAF placed at 45 mm from the overlap edge is shown in fig. 7.6. Only this timeline is discussed as the behavior is generally the same for all adhesive bondline specimens with a CDAF and BDAF.
The timeline is comprised of the following events:

1. The disbond front reaches the DAF location;
   (a) In case of the BDAF the disbond keeps growing around the BDAF, but the center of the disbond is arrested
   (b) In case of the CDAF the disbond is arrested along the entire disbond front at the location the CDAF
2. A fatigue crack appears in the aluminum ply adjacent to the adhesive bondline of the lap adherend in the direct proximity of the DAF;
   (a) In case of the BDAF the disbond front is far beyond the BDAF location and the crack seems to originate from the bolt hole
   (b) In case of the CDAF the location of the fatigue crack coincides with the disbond front
3. A delamination is initiated at the fatigue crack location between the cracked aluminum ply and the adjacent glass fiber prepreg layer shortly after the fatigue crack has grown through the width of the ply
4. The delamination quickly starts to propagate whilst the disbond remains arrested. This behavior is similar to the observations made during the fatigue testing of bonded FML patched repairs by [44]

These results are the opposite of hypothesis 4 from section 3.2 which states that the initiation of adherend fatigue damage will re-start the initially arrested disbond growth. Instead, after crack initiation, the disbond remains arrested and jumps into the FML adherend as a delamination.

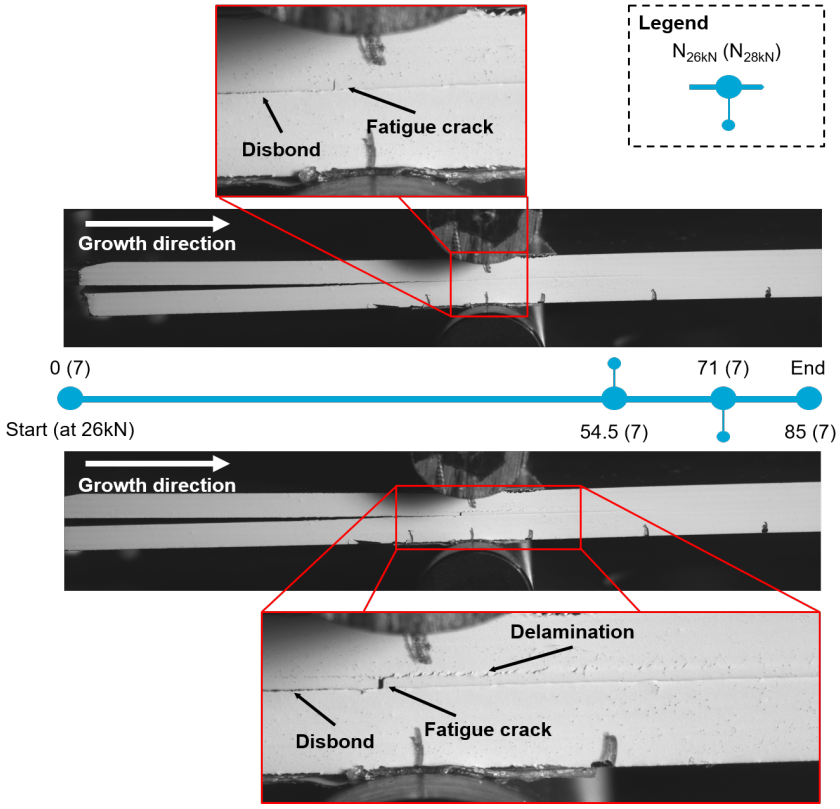

Figure 7.6: The load cycle N (in thousands) timeline of an adhesive bondline specimen with a CDAF tested at a maximum fatigue load of 26 kN - specimen 2_09. Note: a maximum fatigue load load of 28 kN has been applied for 7,000 cycles first to initiate a disbond.

The shift of criticality from disbond to delamination growth once the aluminum ply has been cracked through the width can be explained by the resistance to damage growth and the SERR of both material interfaces. The prepreg/aluminum ply interface has a much lower resistance to disbond growth than the adhesive/aluminum ply interface. As a result, criticality of the disbond can only remain if the SERR in the prepreg/aluminum ply interface is significantly lower. In contrast, the Mode I component is expected to increase due to the added hinging effect visualized in fig. 7.7. This fill force the criticality to the delamination, but no further analysis was performed to confirm this statement.

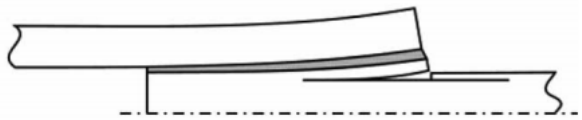

Figure 7.7: Hinging effect after a ply failure in a double-lap joint (from Banea and da Silva [11]).

Prepreg Bond Line Specimens

A timeline of the adherend fatigue damage development of a specimen with a BDAF placed at 65 mm is shown in fig. 7.8 which is representative for all BDAF specimens. The single specimen with a CDAF will be discussed separately in section 7.3.2.

The timeline consists of the following events:

1. The disbond keeps growing around the BDAF, but the center of the disbond is arrested
2. A fatigue crack appears in the lap adherend in the aluminum ply adjacent to the adhesive bondline in the direct proximity of the DAF

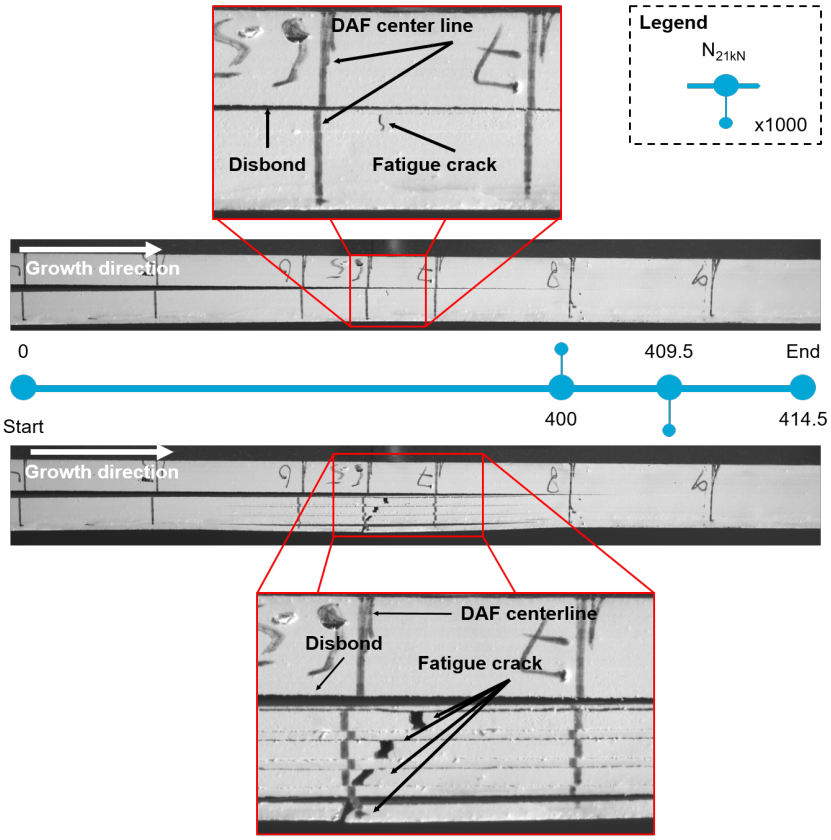

Figure 7.8: The load cycle N (in thousands) timeline of a prepreg bondline specimen with a BDAF tested at a maximum fatigue load of 21 kN - specimen 4_09.

3. The disbond does not re-start to grow, but unlike the adhesive bondline specimens, no delamination is initiated that shows any significant growth

4. Instead, the fatigue cracks jump upwards through all the aluminum plies

All bonded interfaces are made using the same materials therefore having the same resistance to disbond growth. It appears that the BDAF maintains a sufficient SERR in both interfaces that retains the arrest of the disbond whilst not propagating a delamination at the tested maximum fatigue loads of 17.5 kN, 19.5 kN and 21 kN.

A Critical Note on the Presented Analysis

It is stressed that the observed behavior is a response to a fully cracked ply which cannot be extrapolated to the response of a fatigue crack in a ply that retains load carrying capabilities. The narrow width of the specimen creates a free edge effect during the growth of the fatigue crack causing a rapid and complete cracking of the aluminum ply.

The current analysis suggest that disbond growth is not re-started after the initiation of a fatigue crack. Rather, a delamination will propagate if it has a lower resistance to disbond growth compared to the bond line interface. These results do not describe the response to a fatigue crack in a regular structural bonded joint due to aforementioned reasons.

7.3.2. Specimen 4_07

The prepreg bondline specimen with the CDAF is investigated separately because an increase of the DGR was observed at a load cycle number which roughly coincides with a detected aluminum fatigue crack.

The average DGR is plotted against the number of load cycles in Figure 7.9 showing that the fatigue crack is observed after the increase of the DGR. Possibly the crack has initiated a significant time period before it was observed. However, the crack is observed far behind the disbond front (see table 5.2) so it is questionable whether the crack could have influenced the DGR. More likely is that the reduction of friction played a role as discussed in section 7.1.2, but this remains undecided.

Based on these results, no relation can be found between the initiation and growth of adherend fatigue damages and a change in the arrest of disbond growth.

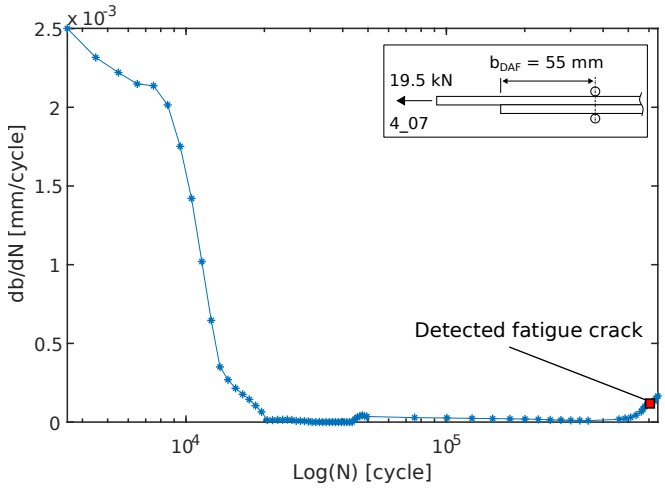

Figure 7.9: Mapping of the initial adherend fatigue damage observation load cycle number onto the DGR history.

7.4. Disbond Front as Fatigue Crack Initiator

One of the research hypothesis states that a slow growing disbond front can lead to the initiation of a fatigue crack. The adherend fatigue damage observations of the adhesive bond line specimen with a CDAF suggested that this indeed can be true. However, before this can be stated with more certainty, two topics must be addressed. First is the question if the peak stress associated with the disbond front is indeed capable of initiating a fatigue crack. Second is the question if the DGR plays a significant role in this fatigue crack initiation mechanism. To answer these questions, the fatigue crack observations of the adhesive bond line specimens will be visualized and further analyzed here. The trends were consistent across the adhesive and prepreg bond line specimens so the prepreg bond line specimens will not be shown.

7.4.1. Effect of the Disbond Front

The load cycle number and location of the first observed fatigue cracks relative to the DAF and disbond front position from table 5.1 have been visualized in fig. 7.10(a) and fig. 7.11(b). The fatigue crack location and corresponding disbond front position are given by a diamond and square marker respectively and the results of both the left and right side are shown. Based on fig. 7.10(a) and fig. 7.11(b), the following observations can me made:

1. Without a DAF, the fatigue crack appears around the initial disbond length b_0 of 30 mm
2. With a CDAF, the behavior is consistent across both positions;
   (a) The CDAF results in the earliest detected fatigue cracks
   (b) The location of the fatigue crack coincides with the disbond front and the CDAF location
3. With a BDAF, the behavior is different across both positions;
   (a) Placed at 35 mm, the fatigue crack location coincides with the DAF location, but not with the disbond front

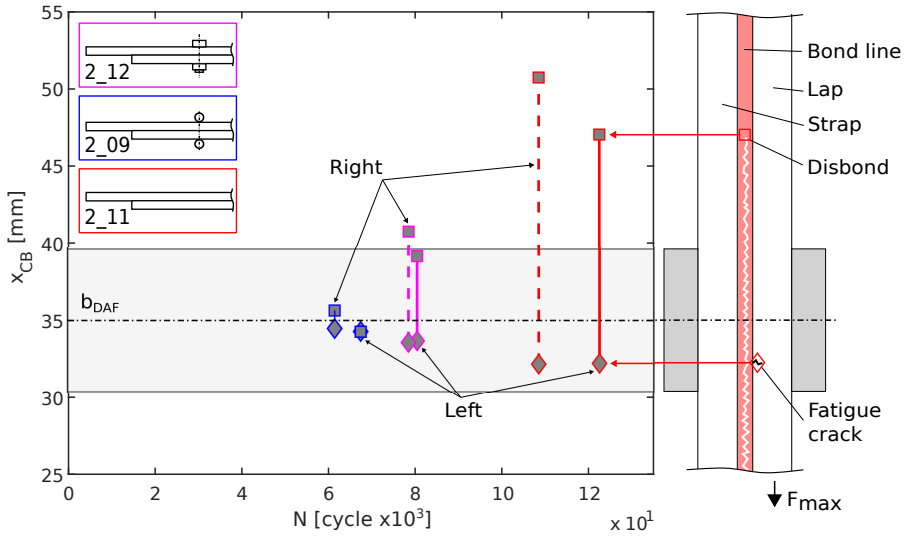

(a) Specimens with b_{DAF} = 35 mm (specimen left and right side).

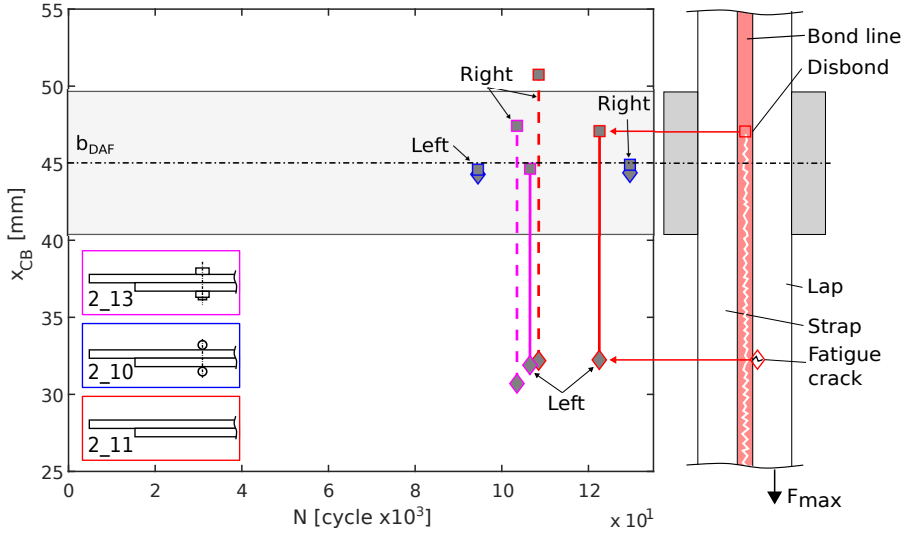

(b) Specimens with b_{DAF} = 45 mm (specimen left and right side).

Figure 7.10: A visualization of the first fatigue crack detected on both sides of the specimen; load cycle number and the position of the crack relative to the DAF and the disbond front - Adhesive bond line specimens.

(b) Placed at 45 mm, the observed behavior is comparable to the behavior without a DAF

It is demonstrated that the fatigue crack location consistently coincides with the disbond front in the specimens with a CDAF. The behavior of both BDAF specimens is interesting for two reasons. First, fatigue cracks with a BDAF are detected later compared to a CDAF which was not expected given the bolt hole stress concentration. Second, the presence of the BDAF placed at 45 mm has not led to an earlier observation of a fatigue crack compared to the specimen without a DAF. This will be further investigated next.

7.4.2. Effect of the Disbond Growth Rate

To understand the relation between the DGR and the observed fatigue cracks, a visualization is needed. This is achieved by combining fig. 7.10(a) and fig. 7.10(b) with the disbond growth results as shown in fig. 7.11(a) and fig. 7.11(b). Note that only the right side results are shown to promote clarity of the information. Also, the second fatigue crack that was detected in specimen 2_13 has been included.

The CDAF results consistently show that the fatigue crack observation near the disbond front is pre-

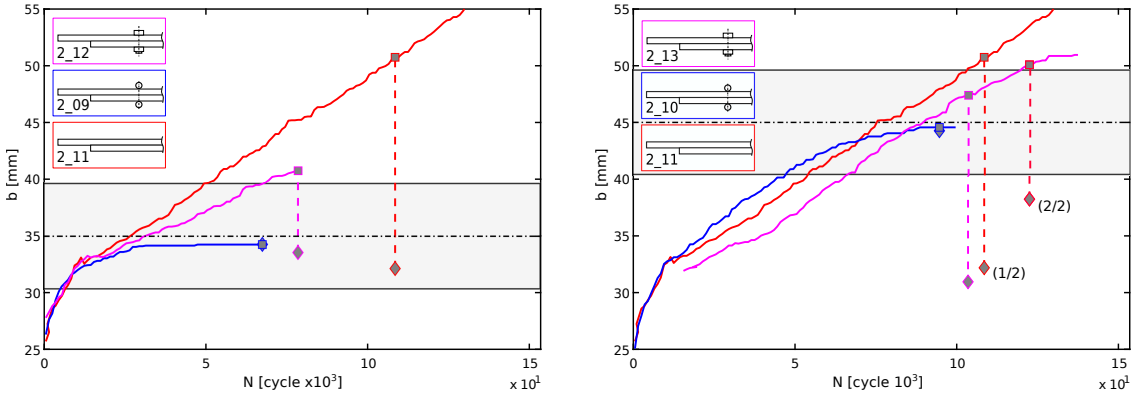

(a) Specimens with b_{DAF} = 35 mm (specimen right side only).

(b) Specimens with b_{DAF} = 45 mm (specimen right side only).

Figure 7.11: A visualization of the first fatigue crack detected on right side of the specimen: load cycle number and the position of the crack relative to the DAF and the disbond front combined with the disbond length results - Adhesive bond line specimens.

ceded by a complete arrest of the disbond growth. It is therefore tempting to conclude that the relation between the arrested disbond front and the observed fatigue crack is causal. However, fatigue crack initiation can also occur by fretting of the disbonded surfaces [52] or by the physical presence of the CDAF. Fretting is excluded as the relative sliding can only have been minor given that arrest occurred in front of the CDAF. The clamping load of the CDAF is applied out-of-plane and only rotational movements of the clamp could contribute to the in-plane stresses, but these are restricted by the foam supports (see section 4.1.1). It is therefore expected the clamp contribution to the in-plane stresses has been minor. It must be admitted that no stress analysis was performed for confirmation as this was deemed not necessary.

Based on these arguments, the hypothesis is confirmed that an arrested disbond front can lead to the initiation of fatigue cracks.

The delayed crack detection of the BDAF compared to the CDAF can be explained by the location of fatigue crack initiation and the delay until its detection. The fatigue crack is expected to have initiated at the fastener hole for two reasons. First, it was demonstrated in section 5.1.2 that arrest only occurs around the location of the BDAF making it the only region exposed to the peak stress associated with the disbond front for a longer amount of time. Second, the bolt hole stress concentration will amplify the peak stress around the arrested disbond front making the bolt hole the critical location for fatigue. The crack growth period until the edge of the specimen is reached creates a delay between fatigue crack initiation and detection. Unlike with the CDAF, the crack tip is not continuously exposed to the peak stresses associated with the arrested disbond front because the disbond has grown around the BDAF. It is therefore thought that the delay between crack initiation and detection is higher for the BDAF compared to the CDAF.

The behavior of the CDAF placed at 45 mm is caused by the fatigue life of the CLS specimen being reached before the crack that initiated around the fastener hole can be detected. This is supported by the observation that the a second fatigue crack is detected a little while later that originates from the fastener hole.

7.5. Expanding the results: From Cracked Lap Shear Specimen to a Bonded Structural Joint

The current research is bounded by the limitations of the Cracked Lap Shear (CLS) specimen. As a result, the analysis of the experimental results presented in this chapter cannot directly be extrapolated to any bonded structural joint. These discrepancies will be highlighted here to create awareness, but no solutions are proposed.

The Single Lap Joint (SLJ) is a commonly used type of bonded structural joint [10] which is depicted in fig. 7.12 together with the CLS specimen. Also illustrated in fig. 7.12 are the typical damage modes associated with a Bolted Disbond Arrest Feature (BDAF) in a CLS specimen and a SLJ [7]. There are two important differences regarding the typical damage modes between both bonded joints;

1. Disbond growth direction
    - In the CLS specimen the disbond grows in a single direction parallel to the loading direction
    - In the SLJ the disbond grows orthogonal to the loading direction
2. Fatigue crack growth direction
    - Fatigue cracks in the aluminum plies grow orthogonal to the loading and the disbond growth direction in a CLS specimen. Combined with the free-edge-effect, the fatigue crack grows rapidly through the width of the aluminum ply leading to loss of the load carrying capability
    - In the SLJ the crack grows in the same direction as the disbond and not necessary orthogonal to the loading direction. Additionally, the aluminum ply retains its load carrying capability once a fatigue crack has initiated and starts to grow. In this case the load is being transferred through (1) the cracked ply and (2) through the adjacent glass fiber prepreg ply. The latter is called fiber bridging which creates a delamination between the cracked aluminum ply and the adjacent prepreg interface

Considering these differences, only two observations can be extrapolated to a structural bonded joint. First, Mode I reduction is a very effective driver for disbond growth arrest. Second, an arrested disbond front can initiate a fatigue crack. All other observations are solely applicable to the CLS specimen.

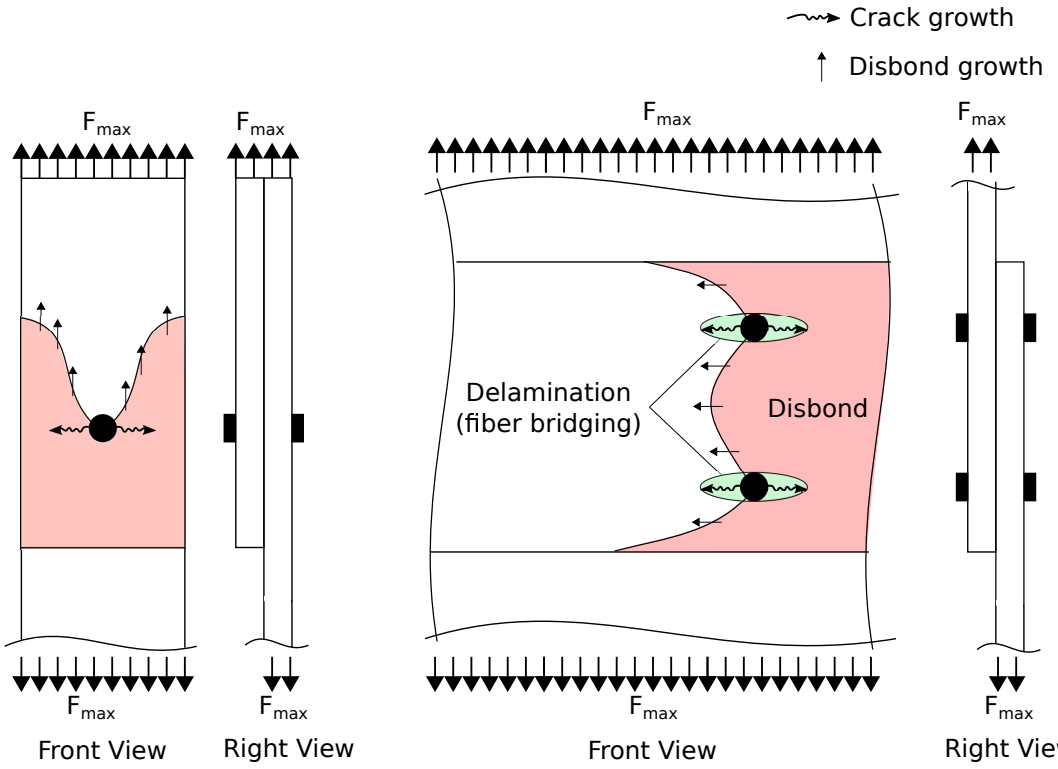

Figure 7.12: Comparison of disbond, delamination and fatigue crack growth in CLS specimen (left) and a typical bonded SLJ (right) with a BDAF.

7.6. Synthesis and Hypothesis Evaluation

The analysis of the current section aimed to experimentally investigate the conditions necessary for arrest, the conditions provided for arrest by a BDAF, the effect of adherend fatigue damages on disbond growth that has been arrested and whether an arrested disbond front can lead to the initiation of fatigue cracks. By synthesizing the analysis, the five research hypotheses are evaluated;

- **Hypothesis 1**: The disbond length and DGR results of the adhesive and prepreg bond line specimens have confirmed that a full arrest has been achieved by the CDAF. Additionally, the SERR footprint analysis has demonstrated that only the reduction of Mode I exists in the same region where the arrest of disbond growth occurs. This suggests that Mode I reduction is a very effective driver for the arrest of disbond growth. The relative contribution to the achieved arrest of disbond growth by the reduction of Mode II through friction is unknown
- **Hypothesis 2**: Disbond growth arrest in the prepreg bond line CDAF specimen occurred only momentarily and was followed by a period of slow and steady disbond growth. This indicates that Mode II reduction may still be needed, even after a complete elimination of Mode I
- **Hypothesis 3**: Mode I reduction is thought to decrease when moving away from the BDAF towards the specimen edges. The reduction of Mode II by bolt shear engagement is expected to increase as the disbond grows further beyond the BDAF. No firm conclusion can be drawn based on the presented analysis because the SERR footprint of the BDAF was not studied
- **Hypothesis 4**: Fatigue crack initiation did not re-start disbond growth. Instead, a delamination is initiated that quickly propagates if the delamination interface has a lower resistance to disbond growth compared to the bond line interface. If both interfaces are identical, no propagation of delamination occurs and the fatigue crack jumps upwards through the adherend
- **Hypothesis 5**: Based on the results of the adhesive bond line CDAF specimens it is concluded that an arrested disbond can lead to the initiation of a fatigue crack

8

Disbond Growth Model Analysis

So far, the analysis of the conditions necessary for the arrest of disbond growth has demonstrated that the reduction of Mode I is very effective. However, the analysis has only been empirical and limited to the test parameters. The Disbond Growth model will be used in this chapter to further study the conditions necessary for arrest. This is done by modeling the effect of the Clamped Disbond Arrest Feature (CDAF) over a wide range of maximum fatigue loads. Also, the arresting capability of Mode I and mode II reduction is modeled and compared. A validation of the Disbond Growth Rate (DGR) and disbond length predictions with and without a Clamped Disbond Arrest Feature (CDAF) will be presented first.

Analysis of the experimental results has indicated that an arrested disbond front can initiate fatigue cracks in the adjacent aluminum ply. The second part of the analysis utilizes the Disbond Growth Model to analyze the effect of the disbond front and the Disbond Growth Rate (DGR) in this fatigue crack initiation procedure. A validation of the fatigue crack initiation predictions with and without a Clamped Disbond Arrest Feature (CDAF) is given first.

8.1. Model Inputs

Depending on the specimen, the batch 2 or 4 specimen geometries from table 4.1 were used, the FML layup and ply material properties were taken from section 4.1.1, the adhesive or prepreg bond line material fracture parameters from table 4.6 and the load parameters from table 4.5. Plane stress is assumed in the width direction and clamped-clamped support boundary conditions are applied. The SERR Footprint from fig. 6.2 corresponding to a tensile load of 26 kN and a clamping pressure of 100 MPa is used. The prepreg bondline specimens are loaded at different maximum fatigue loads, but it has been demonstrated in section 6.3 that the SERR footprint is largely independent of the tensile load so no major discrepancies are expected. The residual strains are calculated with a temperature difference of $dT = T_{cure} - T_{application} = 121^{\circ}C - 21^{\circ}C = 100^{\circ}C$.

Two adjustments have been made to the SERR footprint before being implemented into the model. First, the data points beyond the 80 mm mark have been removed as they are influenced by the support boundary conditions. Second, the bondline coordinates have been shifted by 50 mm to centre the SERR footprint around the CDAF. Values in between the SERR footprint data points are calculated using linear interpolation and disbond lengths outside the data range are assumed not to have been influenced by the CDAF.

8.2. Validation of the Disbond Growth Rate Predictions

A validation of the DGR predictions of both the adhesive and prepreg bond line specimens with and without a CDAF was performed to study the capabilities and limitations of the model when representing the real life disbond growth behavior. This knowledge is required to guarantee a justifiable and correct interpretation of the model analysis.

8.2.1. Without a Disbond Arrest Feature

The predicted and experimental DGR results of the prepreg (4_08) and adhesive (2_11) bond line specimen are shown in fig. 8.1(a) and fig. 8.1(b) respectively.

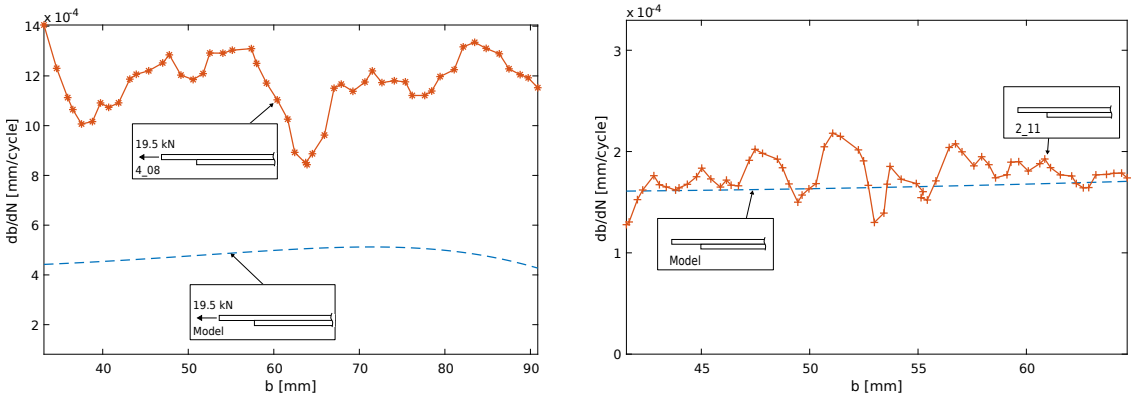

(a) Prepreg bond line: (1) F_{max} = 19.5 kN - 4_08 and (2) F_{max} = 19.5 kN - Model

(b) Adhesive bond line: (1) F_{max} = 26 kN - 2_11 and (2) F_{max} = 26 kN - Model

Figure 8.1: Predicted and experimental average DGR results without a DAF.

Prepreg Bond Line Specimen

The model predictions and experimental results show a similar and constant trend in the DGR result, but the model is consistently unconservative. The discrepancies can be related to several factors. First, the high value of the exponential fracture parameter shown in table 4.6 results in a high sensitivity to and amplification of errors in the SERR calculations. Second, the calculations of the fracture parameters contain several deficiencies which are discussed in appendix G. Third, the model assumes identical, symmetrical and balanced FML adherends and the bond line is neglected in the beam stiffness calculations. These assumptions are not valid for the prepreg material as bond line due to the higher stiffness.

Overall, the error seems to be constant so the predicted trends using the prepreg material should be correct, just the actual values are not realistic.

Adhesive Bond Line Specimen

The model predictions and experimental results match very well except for the fluctuations in the experimental results, but these can be attributed to measurement uncertainties as discussed in section 5.1.1. The lower fracture parameter exponent of the adhesive material makes the predictions much more robust against errors in the SERR calculations and the fracture parameters have been obtained through a rigorous procedure by [8]. Also interesting is that the match between the averaged experimental DGR and the model predictions along the centerline show that the CLS specimen is very robust in providing constant disbond growth driving forces across the width of the disbond front.

8.2.2. Clamped Disbond Arrest Feature

The predicted and experimental DGR results of the adhesive (2_09, 2_10) and prepreg (4_07) bond line specimens are shown in fig. 8.2 and fig. 8.3 respectively.

Adhesive Bond Line Specimens

The predicted and experimental results match quite well except for a few differences. First, the predicted curve seems to be concave where the experimental curves are convex. This is probably because only two data points with a linear interpolation are used to describe the decrease of Mode I in front of the CDAF (see section 6.4). Second, the model fails to predict a complete arrest probably by neglecting the Mode II related mechanisms discussed in section 7.1.2. These are the lower Mode II SERR fatigue threshold of the bond line material and the disbond front locking mechanism caused by an interaction of friction and the applied clamping load at the DAF location. Third, the predicted increase in Mode I in front of the CDAF, observed in section 6.2, is not recognized in the experimental results and remains

an ill understood mechanism.

The predicted region of arrest matches well with the experimental results. The observation made in section 7.1.1 that disbond growth of specimen 2_09 only occurred in the region of influence of the CDAF seems correct. The post CDAF region can not be validated due to a lack of experimental data.

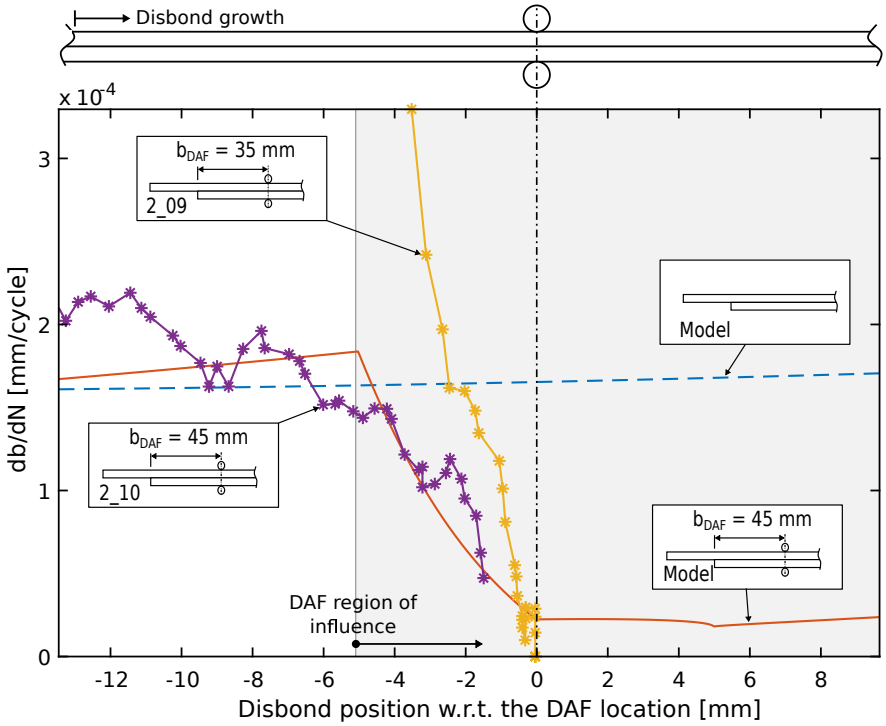

Figure 8.2: Adhesive bond line: predicted and experimental DGR results with a CDAF (specimens 2_09 and 2_10).

Prepreg Bondline Specimen

The predicted and experimental results match quite well in front and after the CDAF, but to a lesser extent compared to the adhesive bond line specimens. These differences are related to those already discussed when comparing the result without a CDAF. A nice result is that the sharp transition from Mode I to Mode II disbond growth at the CDAF location predicted by the model matches the experimental results.

8.3. Conditions Necessary for Arrest

The experimental results have shown that a CDAF can arrest disbond growth, but this has only been tested at a limited range of maximum fatigue loads. The question remains whether a pure Mode I effect is enough at all load levels. Also, the relative effect of reducing Mode I and Mode II must be known before a statement can be made that Mode I reduction is the main driver of arrest. These two topics are covered in this section by using the validated predicting capabilities of the disbond growth model.

8.3.1. Effect of the Maximum Fatigue Load on the Arrest by a Clamp as Disbond Arrest Feature

The adhesive bond line specimen with a CDAF is modeled using the inputs from section 8.1 except that the CDAF is now placed at 55 mm from the overlap edge. The maximum fatigue load F_{max} has been varied between 20-30 kN. The DGR and disbond length results are shown in fig. 8.4(a) and fig. 8.4(b) respectively.

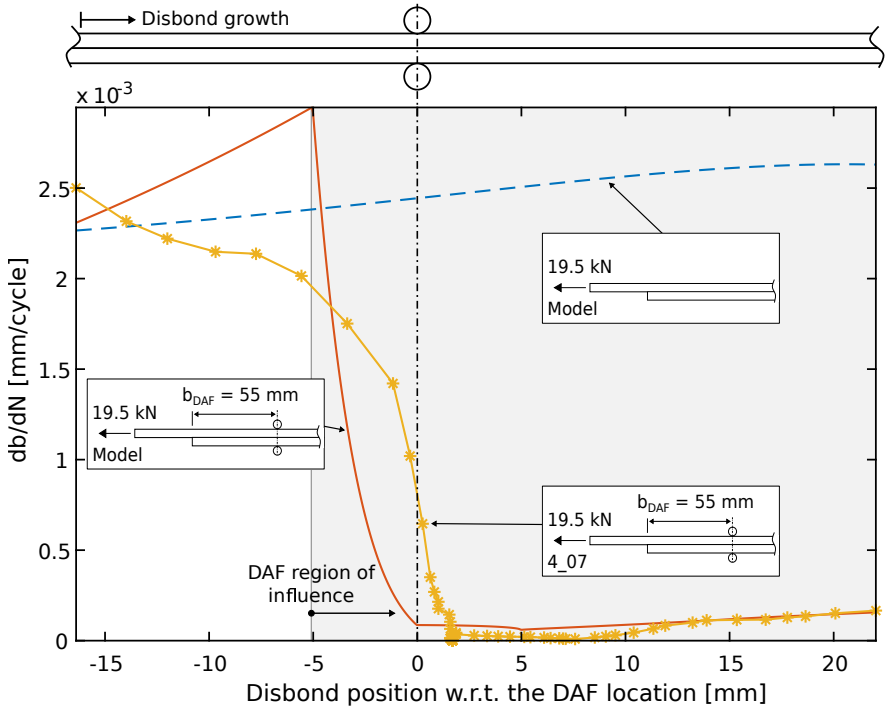

Figure 8.3: Prepreg bond line: predicted and experimental DGR results with a CDAF (specimen 4_07)

Figure 8.4(a) shows that the Mode I elimination by the CDAF remains a very effective arresting mechanism at higher loads. However, the pure Mode II DGR behind the CDAF displays an exponential growth with an increase of F_{max}. The remaining Mode II growth becomes even more apparent in fig. 8.4(b) where the effect on the disbond length of the CDAF rapidly decreases with a increase in F_{max}.

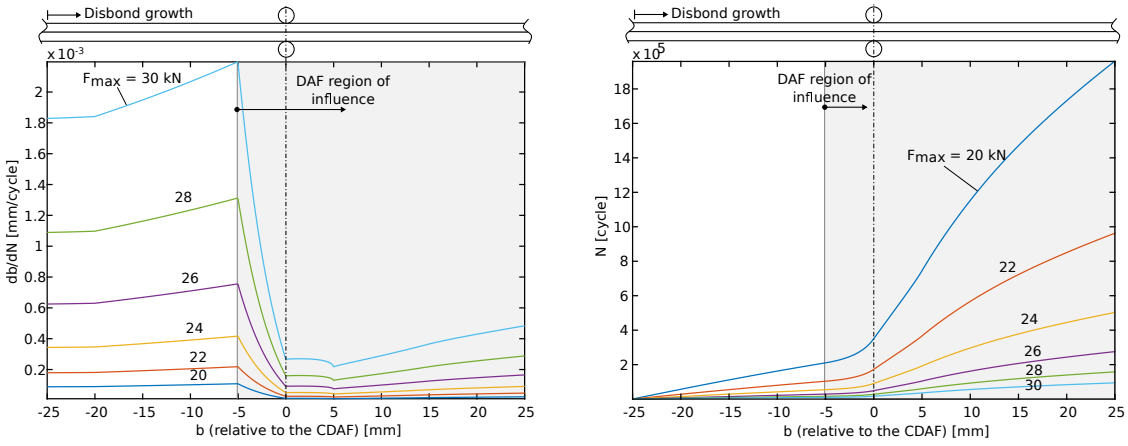

(a) Disbond Growth Rate (DGR).

(b) Disbond length.

Figure 8.4: Effect of F_{max} on the arrest of disbond growth by a CDAF in the adhesive bond line specimen with b_{DAF} = 55 mm.

The key message of both plots is that the elimination of Mode I is extremely effective for arrest, but the push to a pure Mode II disbond growth inherently implies the consideration of Mode II reduction at elevated fatigue loads. The need for Mode II reduction becomes even higher if a full arrest is required by design and if this full arrest relies on staying below the adhesive Mode II fatigue threshold. The role of Mode II relative to Mode I will be further analyzed in section 8.3.2.

A note of caution is given that the results must be interpreted knowing that the predicted growth beyond the CDAF has only been validated for the prepreg and not the adhesive bond line specimen.

8.3.2. A Critical Evaluation of Mode I and Mode II as Drivers for Arrest

So far, experimental and modeling analysis have proven that Mode I reduction is very effective in arresting disbond growth, but its effect compared to Mode II has not been studied. It is probably reasonable and sufficient to say that Mode I will be more effective solely based on the lower resistance to Mode I damage growth of an adhesive. However, because it has been shown that a need for Mode II reduction arises at elevated fatigue loads, it is interesting to express this difference in a tangible comparison of disbond growth arrest.

This analysis presents a comparison in arrest of a similar total reduction in Mode I and Mode II using the adhesive bond line specimen and the inputs from section 8.1. A theoretical SERR Footprint has been defined separately for Mode I and Mode II that results in approximately the same total reduction:

$$G_{\%} = \begin{cases} 0, & \text{if } -5 \geq b \\ \frac{-\alpha}{5}(b+5), & \text{if } -5 \leq b \leq 0 \\ -\alpha, & \text{if } 0 \leq b \end{cases} \tag{8.1}$$

Where $G_{\%}$ is the SERR footprint for Mode I $G_{\%,I}$ or Mode II $G_{\%,II}$, b is the disbond front position with respect to the DAF position and α is the maximum reduction of the the Mode I or Mode II component. α is 100% and 25% for the pure Mode I and Mode II SERR footprints respectively. A reduction of 25% was used for Mode II as the G_I equals roughly 4 times G_{II}.

The arresting effect on the DGR and disbond growth of both SERR footprints was calculated at a load range of 22 kN to 28 kN and has been plotted in fig. 8.5(a) and fig. 8.5(b) respectively. The DGR results confirm that Mode I is much more effective compared to mode II. The difference is even more striking when comparing the arrest of disbond growth.

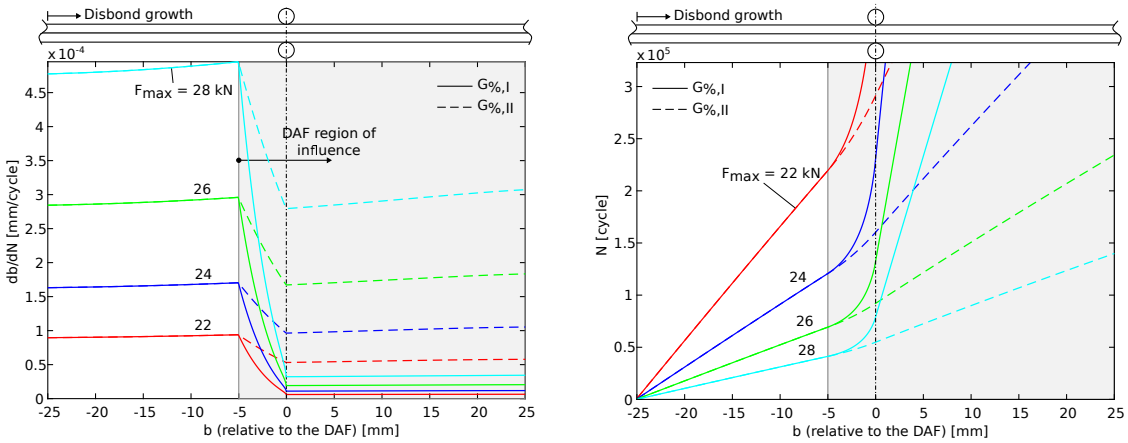

(a) Disbond Growth Rate (DGR)

(b) Disbond growth

Figure 8.5: Effect of F_{max} on the arrest by Mode I and Mode II in the adhesive bond line specimen with DAF placed at 55 mm from the overlap edge.

The relevance of Mode II reduction is dictated by the joint design, the bond line material, the load cases and the arresting requirements. The proportion of the arrest of disbond growth that can be contributed by the reduction of Mode I becomes small when the initial joint design has mostly eliminated Mode I. The lower Mode II fatigue threshold (if it exists) and the general resistance to Mode II damage growth of an adhesive material dictate the damage growth resulting from the joint design and the applied loads. Ultimately, the resulting damage growth must be compared with the arresting requirements to determine whether Mode I reduction is sufficient or, if more arrest is needed, Mode II reduction should be included.

Based on the presented comparison, it can be concluded that Mode I is indeed the main driver for arrest, but Mode II should be considered at elevated loads for previously discussed reasons.

8.4. Validation of the Fatigue Crack Initiation Predictions

A validation of the fatigue crack initiation predictions of the adhesive bond line specimens with and without a CDAF was performed to study the capabilities and limitations of the model when representing the real life fatigue crack initiation behavior. Before the validation is presented it is important to reiterate that the fatigue crack initiation component of the model was developed with the aim to predict the general trends of fatigue crack initiation in relation to the DGR, not an accurate load cycle number (see section 4.2.3).

The experimental crack detection results from table 5.1 are compared to the model predictions in table 8.1. The model predictions and experimental results of specimen 2_11 show a very good match in the fatigue crack location, but an over prediction of the initiation load cycle therefore making the model unconservative. Also, the model is not capable of calculating the location or the number of load cycles at fatigue crack initiation for the specimens with a CDAF. The incorrect calculations of the disbond front are directly related to the miscalculation of the load cycle. Both issues are mainly related to the inability of the model to correctly account for aluminum plasticity. Running the model with maximum fatigue loads where the aluminum yield stress is not exceeded did result in the correct fatigue crack location predictions relative to the CDAF.

Table 8.1: Predicted and experimental fatigue crack detection load cycle and position relative to the disbond front. Note: residual strains are calculated using $dT = -100^{\circ}C$.

Specimen ID	DAF type	DAF position [mm]	Data source	N_{28kN} [cycle]	N_{total} [cycle]	b_{crack} [mm]	b [mm]
2_11	No DAF	-	Experimental	15,000	108,500	32.19	50.75
			Model	0	359,477	31.46	91.43
			Error %	**100.0%**	**-231.3%**	**2.3%**	**-80.2%**
2_09	CDAF	35	Experimental	7,000	61,500	34.48	35.64
			Model	0	290,006	31.35	39.39
			Error %	**100.0%**	**-371.6%**	**9.1%**	**-10.5%**
2_10	CDAF	45	Experimental	10,000	99,500	44.36	44.88
			Model	0	311,331	30.03	48.72
			Error %	**100.0%**	**-212.9%**	**32.3%**	**-8.6%**

Another major shortcoming of the Disbond Growth Model is that the stress alteration caused by the CDAF, or any DAF for that matter, is not accounted for (see section 4.2.1); the model solves for the adherend stresses as if there is no DAF. Based on the predicted strain distribution in fig. 5.12 one might expect that this influence only starts at the region of the DAF. However, the SERR footprint study in section 8.2 has shown that the Mode I region of influence, governed by a change in the internal bending moments of the adherends which affect the stress distributions, starts some distance before the CDAF position. As a result, it is hypothesized that the predicted peak stress is not valid anymore in the region of influence of the DAF.

It is concluded that the model can predict the general trend of fatigue crack initiation in relation to the DGR if the aluminum yield stress is not exceeded, but not the load cycle number.

8.5. Disbond Front as Fatigue Crack Initiator

Experimental testing has shown that an arrested disbond front is capable of initiating a fatigue crack in the adjacent aluminum ply. It has also been shown that such a fatigue crack can lead to a rapid growing delamination or the restart of disbond growth [7] although it was not possible to confirm the latter in this research. Taking these two findings into consideration, the question arises whether full arrest is really desirable, or if slow growth would lead to a longer fatigue life prolongation by delaying the initiation of the critical fatigue cracks. To answer this question, the disbond growth model is used to study the fatigue damage accumulation in relation to the disbond front and the DGR.

For this analysis it was decided to use the adhesive bond line specimens, but to artificially weaken the material by multiplying the coefficients $C_{0\%}$ and $C_{100\%}$ by four. It was found for the adhesive bond line material that the loads necessary to achieve a minimum level of disbond growth resulted in the aluminum yield stress being exceeded. In contrast, the DGR of the prepreg bond line material was so high that it was not possible to study fatigue crack initiation in relation to the disbond front. Artificially weakening the adhesive bond line material enables the analysis on a conceptual level, but it is emphasized that this is a theoretical exercise and not based on true material data.

8.5.1. Effect of the Disbond Front

Discussed in section 2.3.2 is that the peak stress in the adherend adjacent to the disbond front results from (1) the applied tensile load, (2) secondary bending and (3) a stress concentration caused by the stiffness step. The disbond growth model only accounts for the first two factors, but was verified in section 5.2 to predict the strain field and concentration quite accurately. To better understand the effect of this stress concentration on the fatigue behavior a visualization is needed.

The value of the Palmgren–Miner Rule, the Miner Index, of the fatigue critical ply has been calculated at different load cycles with an applied fatigue load of 19.5 kN and with the CDAF placed at 55 mm from the overlap edge. The results are plotted in fig. 8.6 together with the corresponding disbond front position which is indicated by the square marker. According to PM, fatigue initiation has occurred once the value of 1 has been exceeded.

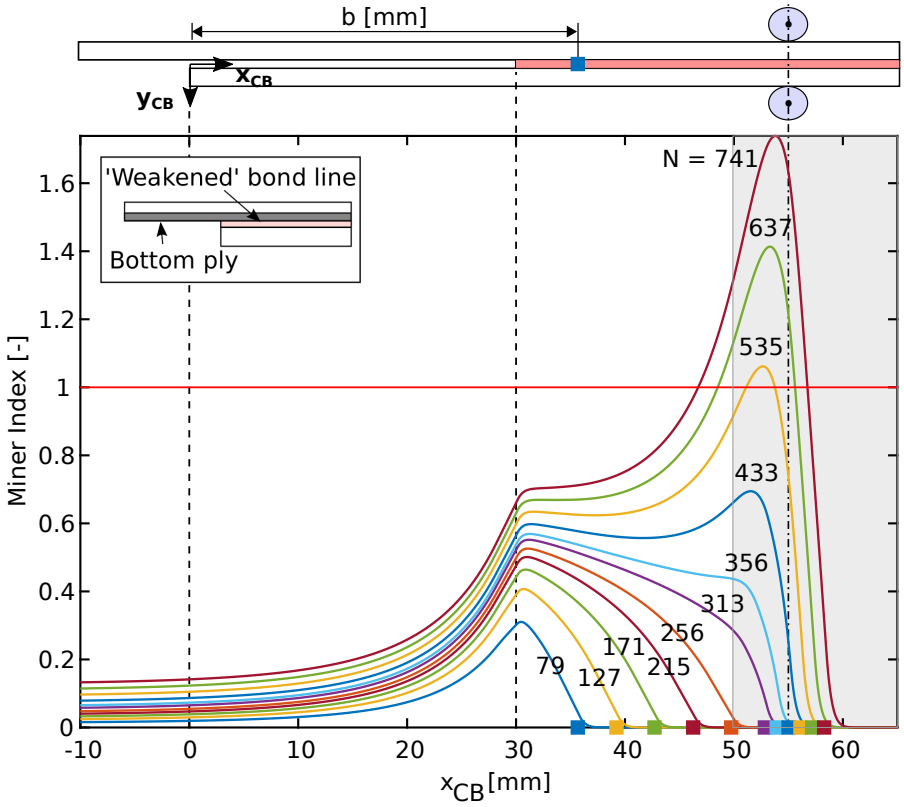

Figure 8.6: Miner Index at load cycle N including the disbond front position of the artificially weakened bond line specimen with F_{max} = 19.5 kN and a CDAF placed at 55 mm from the overlap edge.

Figure 8.6 shows a steady fatigue accumulation in the region of a constant DGR leading up to the CDAF. As the disbond progresses, two gradients become apparent in the Miner Index curves: a steep curve adjacent to the disbond front which corresponds to the peak stress and a shallower curve in the wake of the disbond front which correspond to the stress field plateau observed in fig. 5.13. The decreasing DGR around the CDAF drastically increases the rate of fatigue accumulation around the disbond front resulting from the associated stress concentration.

Summarized, it has been visualized that the peak stress associated with the disbond front has a significant effect on the fatigue accumulation which is drastically accelerated when the DGR is reduced. Aditionally, the model predictions confirm that the fatigue crack initiation will occur directly or far behind the disbond front, depending on the DGR. Based on this behavior it is interesting to see if a higher DGR leads to a longer life to crack initiation and therefore a longer arrest of disbond growth.

8.5.2. Effect of Disbond Growth Rate

Experimental and modeling analysis have demonstrated that fatigue crack initiation is directly related to a stress concentration associated with the disbond front and the DGR. The problem of full arrest is the time that the same section of the aluminum ply around the disbond front gets exposed to the stress concentration. Ensuring a certain level of disbond growth instead of a full arrest might mitigate the fatigue crack initiation by the disbond front therefore achieving an increased fatigue life prolongation by the DAF.

The number of load cycles at fatigue crack initiation and the fatigue crack location relative to the CDAF and disbond front for different DGRs is visualized in fig. 8.7 in a similar way as the visualization of the experimental results in fig. 7.11(a) and fig. 7.11(b). The variation in the DGR has been created by reducing the Mode I component of CDAF SERR footprint $G_{\%,I}$ in steps of 10%. For this analysis, the effect of the CDAF on Mode II, as shown in section 6.2, is ignored and set to zero.

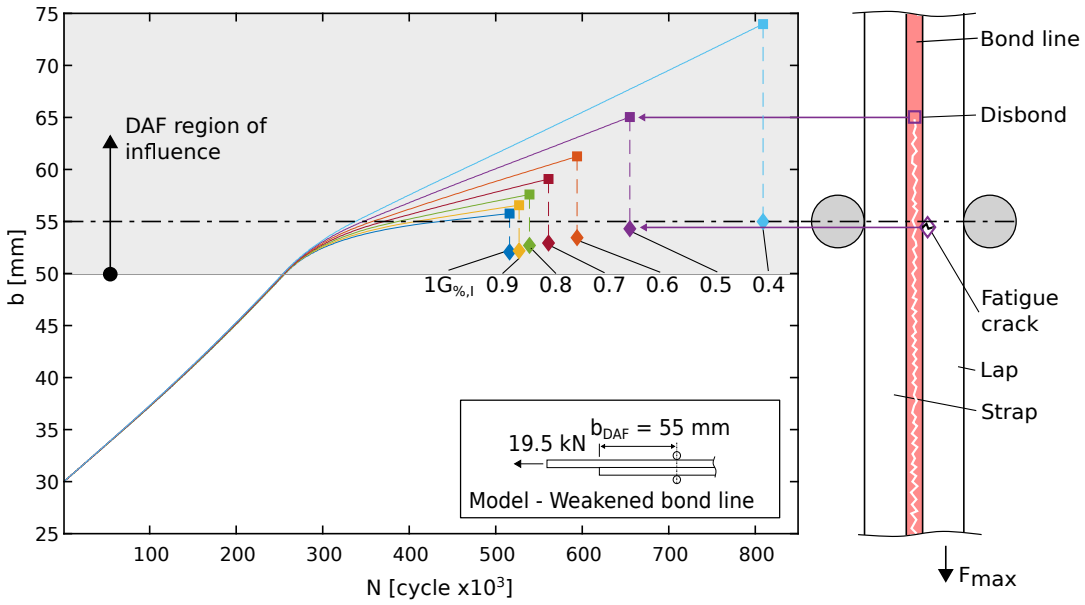

Figure 8.7: Effect of decreasing the Mode I reduction, $G_{\%,I}$, on the number of load cycles at fatigue crack initiation and the crack location relative to the disbond front. The effect of the CDAF SERR footprint on Mode II, $G_{\%,II}$, has been set to zero.

The results show that reducing the arrest of disbond growth can indeed lead to postponement of the fatigue crack initiation, but at the cost of an increase in disbond length. Also, the crack location remains roughly at the location of the CDAF which is related to the higher strain field plateau in the wake of the disbond front (see section 5.2.1). It has been shown in section 7.1.1 that full arrest of disbond growth has been achieved which is currently not captured in the model due to the reasons mentioned in section 8.2.2. The postponement of fatigue crack initiation would be even more significant when comparing to the life until fatigue crack initiation with a fully arrested disbond.

These results have to be viewed in the context of the limitations of the model discussed in section 4.3 and section 8.4. First, in the current analysis, fatigue crack initiations are predicted in the wake of the CDAF whilst it has been determined in section 8.4 that the model cannot correctly predict the stress field in the region of influence of a DAF. Second, the analysis has only been performed for a CDAF configuration and not a BDAF configuration. With a BDAF, the higher strain plateau in the far wake of the disbond front (see section 5.2.2), would be exposed to the stress concentration of the bolt hole if

the disbond has surpassed the BDAF. Given the very low strain values directly in front on the BDAF (see section 5.2.2), it might be more favourable to arrest the disbond growth in front of the BDAF compared to a steady, but continued disbond growth beyond the BDAF.

A final note is given on the design strategy of mitigating/postponing fatigue crack initiation by tailoring the DGR. Given the demonstrated detrimental effect of lower DGRs on the number of load cycles until fatigue crack initiation, it seems daring to design the fatigue strength and corresponding inspection program based on a lower DGR threshold. If the DGR would somehow be lower than predicted, the number of cycles until fatigue crack initiation is likely much lower than expected. Given the current uncertainties and lack of understanding of MM disbond growth, especially under the influence of a DAF, it is doubted by the author whether this is a viable design approach. This is even more true when considering the conventional scatter associated with fatigue crack initiation calculations.

8.6. Synthesis and Hypothesis Evaluation

The analysis of the current section aimed to deploy the Disbond Growth Model to study the conditions necessary for arrest and to understand how disbond growth arrest/retardation can lead to fatigue crack initiation. By synthesizing the analysis, the five research hypotheses are evaluated;

- **Hypothesis 1**: It has been confirmed that Mode I reduction is the main driver for arresting disbond growth. Modeling the effect of the CDAF on the DGR and disbond length at a range of maximum fatigue loads confirmed its continued effectiveness. Furthermore, a comparison between the effect of a similar reduction in Mode I and Mode II demonstrated the superior effectiveness of Mode I
- **Hypothesis 2**: The reduction of Mode II must be considered at elevated loads based on the joint design, the fatigue loads, the bond line material and the disbond growth arrest requirements. It has been demonstrated that even if Mode I is eliminated, the existing Mode II can result in significant DGR as the maximum fatigue load increases. This is especially true if disbond growth arrest is depends on staying below the lower Mode II fatigue threshold of the bond line material (if it exists)
- **Hypothesis 3**: Not covered in this chapter
- **Hypothesis 4**: Not covered in this chapter
- **Hypothesis 5**: The peak stress associated with the disbond front has been demonstrated to be related to the fatigue crack initiation. Also, adjusting the DGR can delay the number of load cycles until fatigue crack initiation, but at the expense of the total disbond length. This is not recommended though for design practice due to the uncertainties with the prediction of the lower DGR threshold and the scatter associated with fatigue crack initiation calculations

9

Conclusions and Recommendations

The aim of this research was to establish the disbond growth arresting potential and possible weaknesses of bolted Disbond Arrest Features (DAF) in bonded Fibre Metal Laminate (FML) joints by model simulations and experimental assessment of the arresting mechanisms and their relation to adherend fatigue damage modes. More specific, this research has studied (1) the conditions necessary for the arrest of disbond growth, (2) the conditions provided by a bolt as DAF, (3) the effect of adherend fatigue damage on the arrest of disbond growth and (4) whether a slow growing disbond front can initiate a fatigue crack.

This chapter presents the most important conclusions and recommendations based on the work detailed in this report. In this chapter the terms Mode I, Mode II and Mode III refer to the Strain Energy Release Rate (SERR) unless stated otherwise.

9.1. Conclusions

This section presents the conclusions of this research. The reader is reminded that the conclusion presented here are based on the Cracked Lap Shear (CLS) specimen which can not always be extrapolated to a real bonded structural joint. These differences will be highlighted in section 9.2.

Conditions necessary for arrest

- The reduction of Mode I is the most effective and therefore the most important driver for disbond growth retardation/arrest
- The reduction of Mode II, although less effective than Mode I, can be necessary to achieve the target disbond growth retardation/arrest depending on the joint design, load levels and the resistance to disbond growth characteristics of the bond line

Conditions provided by a bolt as DAF

- The reduction of Mode I is highest in the direct proximity of the bolt, but diminished along the disbond front towards the specimen free edges

Effect of adherend fatigue damage on the arrest of disbond growth

- The initiation of a fatigue crack in the aluminum ply adjacent to the bond line interface has not re-started the growth of an arrested disbond
- It has consistently been observed that a fatigue crack results in a rapidly propagating delamination if the delamination interface has a lower resistance to disbond growth compared to the bond line interface. If both interfaces are identical, the fatigue crack jumps upwards through the adherend instead of initiating a propagating delamination

Disbond front as fatigue crack initiator

- The peak stress associated with a disbond front can initiate a fatigue crack in the adjacent aluminum ply or metal adherend during disbond growth retardation/arrest
- Fatigue crack initiation can, in theory, be postponed by increasing the Disbond Growth Rate (DGR), but at the expense of a longer disbond length

Aggregation of the research objective

1. The arresting potential of a bolt as DAF has been demonstrated, but a bolt is likely not effective in spreading the main driver for disbond growth arrest/retardation; Mode I reduction
2. The weakness of a bolt as DAF in a bonded FML joint is that an arrested disbond front and the bolt hole stress concentration amplify the initiation of fatigue cracks in the aluminum plies. Those fatigue cracks have consistently been the most critical failure mode instead of disbond growth in the specimens with an adhesive bond line

Besides the conclusions regarding the research objective, conclusions are drawn about the solution methodology that has been developed:

- A quasi-analytical model of the FML CLS specimen has been developed, verified and validated. It can be used to predict the disbond growth and the location and number of load cycles of fatigue crack initiation with a Clamped Disbond Arrest Feature (CDAF)
- A novel clamping fixture, the CDAF, has been developed and successfully used in the first known fatigue experiments where the effect on disbond growth of Mode I reduction is tested in isolation
- A Digital Image Correlation (DIC) processing algorithm has been developed that leverages knowledge of the strain field to automatically locate the disbond front. It has successfully been used as an in-situ, Non Destructive Inspection (NDI) technique for obtaining the disbond area, shape and growth rate
- Testing with a prepreg bond line to represent a 'weakened' adhesive so that testing can be done at realistic fatigue loads has demonstrated to be a useful alternative to an adhesive for testing the arresting behavior of a DAF

9.2. Limitations and Recommendations for Future Work

This sections highlights the limitations and recommendations of the this research.

9.2.1. Limitations

The limitations provided here are accompanied by a recommendation when the effort involved is expected to be minor. Future research opportunities are proposed if the limitation requires a shift of the current paradigm in the assessment and design of bolted DAFs in bonded joints.

- Cracked Lap Shear (CLS) specimen
  - Deploying the CLS specimen for fatigue testing is a two edge-sword. On the one hand it provides stable and controllable conditions needed to study the disbond growth arresting behavior of a DAF. On the other hand it is not representative for the conditions seen in a real bonded structural joint. To give an example: the effect of adherend fatigue damage initiation and growth on the arrested state of a disbond could not be properly studied since the free edge effect leads to a rapid and complete crack of the entire aluminum ply. Another example is the disbond growth direction which is incorrect. Currently no standardized test specimen exists that closely resembles the geometry, boundary conditions and loading of a typical bonded joint to test the arrest of disbond growth
  - Research opportunity: develop a novel test specimen that resembles the geometry, boundary conditions and loading of a typical bonded joint that is capable of (1) studying the disbond growth arresting behavior and (2) the fatigue crack initiation and growth period and its effect on the arrest of disbond growth

- Adhesive bond line material
  - The high resistance to Mode II damage growth of the FM94 adhesive material made it impossible to generate enough disbond growth under realistic circumstances to characterize the arresting behavior of a DAF before fatigue failure of the adherends. This is a fundamental problem linked to the philosophy of the DAF: arresting capabilities must be demonstrated due to a lack of confidence in the quality of a bond line; not because of its sound resistance to damage growth. Therefore, from an experimental and design perspective, it makes more sense to study DAFs in a weakened bond line. However, this requires a controllable and repeatable weakening process which currently does not exist
  - Research opportunity: initial testing in this research with a prepreg to represent a 'weakened' bond line showed promising results. However, it is expected that the presence of the fibers will result in a different behavior compared to an adhesive, but it is unknown to what degree. Future research is needed to assess the capability of a prepreg to resemble an adhesive bond line before this approach can be adopted
  - Research opportunity: the development of a controllable and repeatable process to weaken the bond line of any adhesive would be a very powerful and flexible solution
- SERR Footprint Model of the Bolted Disbond Arrest Feature (BDAF)
  - A major limitation of the current research is that the effect on the SERR by a BDAF could not be studied. A 3D model of a CLS specimen with a BDAF was planned, but could not be finished due to time constraints. The absence of this model made it impossible to draw firm conclusions about the conditions provided by a BDAF. Moreover, knowledge of the effect on the SERR can be leveraged to determine high impact design improvements
  - Research opportunity: create a 3D SERR Footprint Model of the BDAF so that the reduction of Mode I, Mode II and Mode III can be studied
- Ignoring friction
  - The current numerical analysis of the CDAF SERR footprint ignores the effect of friction. However, this research and other studies [2, 6] suggest that friction might play a significant role in creating the final push to disbond growth arrest once Mode I has been eliminated. Furthermore, [39] states that an unknown interaction between the friction and clamping force might exist that locks a disbond front in its place. An arrested disbond front is the worst-case-scenario for the initiation of fatigue cracks in the aluminum plies so all mechanisms that might cause arrest must be understood
  - Recommendation: study the effect of a friction by including a friction penalty in the surface contact definition of the SERR Footprint Model and include into the Disbond Growth Model
- Ignoring the lower Mode II fatigue threshold of the bond line material (if it exists)
  - A lower fatigue Mode II fatigue threshold of the SERR fracture parameter might exist below which no disbond growth occurs. The literature is not conclusive on the definition of this lower fatigue threshold and whether it even exists. However, the risk of unknowingly arresting a disbond with the associated negative impact on fatigue crack initiation demands a level of understanding or proof of its irrelevance
  - Recommendation: perform a characterization of the Mode II Paris-Law type curve in the lower SERR range to see if a fatigue threshold can be identified and include the result in the Disbond Growth Model if relevant
- Fatigue crack initiation model
  - The current state of the fatigue crack initiation predictions in the Disbond Growth Model is over simplified; the physical presence of the DAF and plasticity are ignored. Including material non-linear behavior will be very complex and is not needed if the model is used at low enough load levels. The physical presence of the BDAF is included in the analytical model from Cheung [32], but only static disbond growth is considered and the overlap region

is assumed to be lumped together. However, a high level check indicated the possibility of extracting the adherend displacement functions of [32] into the current Disbond Growth Model so that the physical presence of the BDAF can be accounted for

  - Research opportunity: merge the analytical model of Cheung [32] with the current Disbond Growth Model to generate disbond growth and fatigue crack initiation predictive capabilities including the physical presence of the BDAF

Other, more general limitations include the loading conditions (e.g.: uni-directional, R-ratio, frequency, etc.), environmental conditions (e.g.: temperature, moisture ingression, etc), FML layup and the bolt type which were not varied and studied for their effect in this research (see appendix A). All of these parameters are part of future research, but the topics discussed above are viewed of more priority.

9.2.2. Recommendations

Based on the findings of this research, the following recommendations are given:

- To arrest or not to arrest? That is the question!
  - It is recommended to open the debate whether the design approach of a bolted DAF in bonded FML joints should assume the highest possible DGR or a full arrest. Adopting the highest possible DGR is conservative for the predicted disbond area, but unconservative for the number of load cycles until fatigue crack initiation. The safest solution would be to use the maximum possible DGR for the disbond growth predictions and a full arrest for the fatigue crack initiation calculations. However, this results in an over designed joint
- Improve the number of load cycles until fatigue crack initiation in the FML adherends
  - It is recommended to investigate how the fatigue crack initiation behavior of a bolted DAF in a bonded FML joint can be improved. This research only investigated if the initiation of fatigue cracks can be postponed by decreasing the amount of cycles that a single section of the adherend is exposed to the stress concentration associated with the disbond front. Alternatively, the fatigue crack initiation behavior can be improved by reducing the peak stresses or by making sure that the bolt hole stress concentration is not exposed to the highest stresses
- Investigate ways to improve the reduction of Mode I generated by a BDAF
  - It is recommended to investigate how the effect on Mode I by a bolted DAF can be increased and more effectively spread over a wider area. A beneficial, indirect effect is that the reduction of Mode I will also locally reduce the effect of secondary bending which decreases the peak stress associated with the disbond front
- Study the effect of various grid patterns to place the BDAFs
  - Is is recommended to investigate the effect of different grid patters to place BDAFs on the arrest of disbond growth and the initiation of adherend fatigue damages

A

Development of the Overarching Solution Methodology

To achieve the research objective, a three component solution methodology has been developed in three steps. First, the research objective is bounded to a scope that can be can be achieved with a reasonable level of depth in the given amount of time. Second, the envisioned output of the research is formulated and third is the development of the methodology components. This chapter provides an overview and the outcome of all three steps.

A.1. Research Scope

Bounding of the research objective was performed by making several decisions regarding the specimen type, bolt parameters, the specimen geometry and the disbond growth model.

Specimen type:

- The biggest constraint on the scope of the research is imposed by the decision to perform the analysis on a coupon level with the CLS specimen. Utilizing the CLS has the following limitations;
  1. Only a single axial load is applied in the length direction
  2. Disbond growth is simplified to a single direction which is parallel to the applied load
  3. The SERR and Mode Ratio (MR) in the CLS specimen are constant over a major portion of the disbond length resulting in a constant Disbond Growth Rate (DGR)

Bolt parameters:

- The same bolt will be used for the BDAF that was used by Hanx [7]; a 4.8 mm titanium Hi-Lok bolt
- The arresting behavior of a single and not multiple bolts is tested

Specimen geometry:

- The CLS specimen will be made using identical Fibre Metal Laminate (FML) adherents with a balanced and symmetrical laminate layup
- Only a single geometry and GLARE grade will be tested

Loading parameters:

- The effect of the R-ratio, loading frequency, Variable Amplitude (VA) loading and environmental conditions will not be considered

Disbond Growth Model:

- The model is simplified to a 1D representation of the problem
- Adherent fatigue crack growth period is not included

A.2. The Envisioned Research Output

Now that the research objective, questions and hypotheses been defined, the envisioned research output is formulated which will be used as a guideline for the design of the solution methodology. It was discussed in section 2.1 that the functionality of a DAF is to restrict the Mode I, Mode II and Mode III SERR components to reduce the DGR so that disbond growth retardation or arrest can be achieved as depicted fig. A.1.

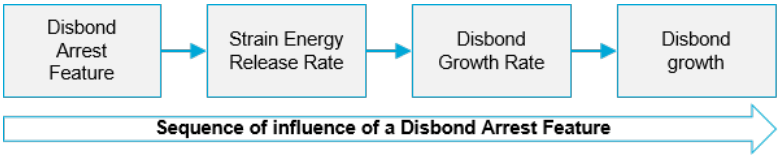

Figure A.1: The sequence of influence on disbond growth of a DAF.

Naturally, the SERR, DGR and disbond growth lie at the basis of studying the arresting behavior of a DAF. As the SERR can not be experimentally obtained, two output are proposed based on the DGR and disbond growth behavior with a DAF in a FML CLS specimen in fig. A.2(a) and fig. A.2(b) respectively. Combined, both outputs present a visual encapsulation of the research objective.

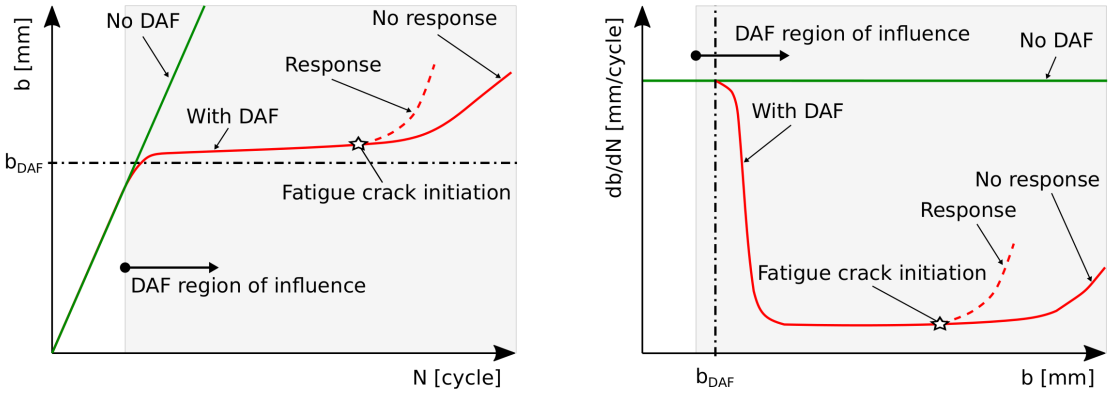

(a) Output 1: Disbond growth.

(b) Output 2: Disbond Growth Rate (DGR).

Figure A.2: Envisioned output based on a FML CLS specimen with a DAF.

Output 1 Disbond growth in a FML CLS specimen with a DAF and adherend fatigue damage initiation

- The 1D disbond growth in a FML CLS specimen with and without a DAF is visualized in fig. A.2(a) by plotting the disbond length b versus the number of load cycles N. The DAF is positioned at b_{DAF}. The constant DGR of a CLS specimen without a DAF allows for the evaluation of the arresting capability of a DAF. By mapping the moment of adherend fatigue damage initiation onto the results, it can be studied if it leads to the re-start and/or acceleration of the arrested disbond growth

Output 2 DGR in a FML CLS specimen with a DAF and adherend fatigue damage initiation

- The 1D DGR in a FML CLS specimen with and without a DAF is visualized in fig. A.2(b) by plotting the DGR db/dN versus the disbond length b with respect to the DAF position; so $b_{DAF} = 0$. The disbond length is centered around the DAF so that the results of different DAF positions can be aggregated. The DGR is an important output because it represents a more direct measure of the effect of a DAF compared to the disbond length

Both figures here represent the arresting behavior in 1D, but in reality the behavior should be represented in 2D as the disbond front grows around the DAF. Therefore, similar figures will have to be created using the disbond area combined with some sort of description of the disbond shape. This will

be further discussed in section 4.1.

Creating both two outputs both by experimental analysis and numerical simulation should generate the practical insights of the arresting mechanisms and their theoretical understanding. Although the SERR is not explicitly shown as a research output, it is an inherent part of the process to generate the two proposed figures by modeling and therefore also included in this research.

A.3. A Brief Summary of the Solution Methodology Components

Now that the research objective, scope and envisioned output is known, the solution methodology is developed which aims to deliver the required information and analysis methods. A summarized overview of the goals and working principles of three components is given here to provide the reader with a high level understanding. A thorough discussion of the components is given in section 4.1, section 4.2 and section 4.3.

Figure A.3, gives an overview of the three solution methodology components and how they span the entire research landscape defined by the research sub objectives and scope.

Objective / Method	1. Effectiveness of bolted DAFs		2. Weaknesses of bolted DAFs in bonded FMLs	
	1.1. Conditions necessary for arrest	1.2. Conditions provided by a bolt	2.1. Effect of adherent fatigue damage	2.2. Adherent fatigue initiation mechanisms
1a. CLS Experiments (Bolt DAF)		• Experimental evaluation of the arresting capability of a bolt as DAF	• Mapping of FML fatigue damage onto the disbond growth results	• Contribution of the bolt to the initiation of adherent fatigue damage
1b. CLS Experiments (Clamp DAF)	• Experimental evaluation of Mode I reduction as the main driver for arrest		• Mapping of FML fatigue damage onto the disbond growth results	• Experimental evaluation if a disbond front can initiate adherent fatigue damage
2. Disbond Growth Model (MATLAB)	• Disbond growth predictions of the Clamp DAF • Effect of Mode I and Mode II on arrest			• Model analysis of the relation between DGR and aluminum fatigue crack initiation
3. SERR Footprint Model (FEM)	**Model (2D):** • SERR analysis of the Clamp DAF	**Model (3D):** • SERR Footprint of the Bolted DAF • Note: not finished this research		

Figure A.3: An overview of the solution methodology components and how they span across the various research topics.

Component 1 CLS experiments

- The goal of the CLS experiments is to;
    1. Generate physical disbond growth data with and without a DAF which consist of the disbond length, DGR, disbond area, Disbond Area Growth Rate (DAGR) and the location and cycle number of adherent fatigue damage initiation
    2. Study Mode I reduction as the main driver for disbond growth arrest using the CDAF
    3. Study the effectiveness of a BDAF in arresting disbond growth
    4. Study the effect of adherent fatigue damage on disbond growth arrest
    5. Study the relation between the disbond front, the DGR and adherent fatigue damage initiation
- The goal is achieved by testing CLS specimens with and without a DAF. Two different types of DAFs are tested: the BDAF and the novel, self developed CDAF. The CDAF has been developed

for several reasons. First, it will assess the hypothesis that Mode I reduction is the main driver for arrest by isolating the discrete clamping load of a bolt and by making it continuous along the clamped specimen width. Second, the relation between the disbond front, the DGR and the initiation of fatigue cracks can be studied in isolation by removing the bolt hole stress concentration. Third, the CDAF is used as a benchmark to evaluate the performance of the BDAF. One batch of specimens was bonded using a FM94 adhesive film and a second batch was bonded using a GF UD S2 FM94 prepreg material to enable testing at lower loads whilst still achieving disbond growth

- Three inspection methods are used to generate the required information. First, the disbond length on both sides of the CLS specimen is measured by visual inspection and used to calculate the DGR. Second, the disbond area is measured indirectly by Digital Image Correlation (DIC) where the strain field is used to create a 2D image of the disbond area. Third, a usb-microscope is used to inspect of adherent fatigue damage initiation at regular intervals

Component 2 Disbond Growth Model (MATLAB)

- The goal of the disbond growth model is to;
  1. Predict the disbond growth behavior of the CDAF at different maximum fatigue loads
  2. Model and evaluate the disbond growth behavior of theoretical DAF configurations other than the CDAF so that the relative importance of reducing Mode I and Mode II can be studied
  3. Model and evaluate the relation between the DGR and fatigue crack initiation
- The goal is achieved by implementing a geometric non-linear 1D model in MATLAB based on existing closed-form solutions. The model is capable of predicting Mixed Mode (MM) disbond growth under the influence of a DAF and to predict the location and cycle number of fatigue crack initiation. The effect of the DAF is modeled by importing the change in the SERR which is predicted by the SERR Footprint Model (see component 3). Only disbond growth and fatigue crack initiation are modeled; disbond initiation and fatigue crack growth are excluded from the analysis

Component 3 SERR Footprint Model

- The goal of the SERR Footprint model is to;
  1. Study the effect of the CDAF on the SERR and to confirm that it has an isolated effect on Mode I
  2. Calculate the percentile change of the Mode I and Mode II SERR components that results from the CDAF which will be used as an input for the disbond growth model. The percentile change of the SERR components is referred to as the SERR footprint for the remainder of this report
- The goal is achieved by creating a 2D geometric non-linear model of the CDAF in a commercially available FEM software package Abaqus. The SERR is measured using the Virtual Crack Closure Technique (VCCT) for a range of disbond lengths
- Originally, it was intended to create a 3D model to study the effect of the BDAF on the SERR as indicated in fig. A.3. However, this was not finished due to time constraints

B

Closed-Form Solutions of the Cracked Lap Shear Specimen: A Review

An exhaustive review of the closed-form solutions of the Cracked Lap Shear (CLS) specimen was performed in support of the development of the quasi analytical Disbond Growth Model. The review focuses on the solutions for the adhesive stresses and the Strain Energy Release Rate (SERR) as both are required for the model.

B.1. Adhesive Stresses

No solutions for the adherend stresses and just three closed-form solution applications were found to find the adhesive stresses in Cracked Lap Shear (CLS) specimen [13, 15, 16].

1. Delale *et al.* [12] solved for the adhesive stresses in an intermediate step to ultimately find the SERR of two CLS configurations for an ASTM Round Robin Report in 1987 by Johnson [15]. However, the closed-form solution is originally formulated for a skin-stiffened plate which is equivalent to two symmetrically joined CLS specimen. The adhesive stress results are not given in [15], but results from the original publication [12] show a remarkable good fit with FEM results as shown in fig. B.1(a) and fig. B.1(b). The solution is complex, but [86] provides a useful MATCAD implementation document. Sadly, the boundary used in [12] are not the same as the those seen in general experimental test set ups.

2. Edde and Verreman [13] created a geometric linear solution for the adhesive stresses and the SERR in a clamped-clamped CLS specimen by applying the Goland [82] solution framework. In their opinion, the calculated adhesive stresses show a reasonably well fit with FEM results as shown in fig. B.2(a) and fig. B.2(b). The over-prediction of the peak peel stress is explained in the words of the authors:

   "*...due to the fact that the latter is the solution of a differential equation of the fourth order, in which the parameters were obtained from the solution of the former third-order differential equation.*"

   It is not clear what they mean and it is not further clarified. Furthermore, their solutions could not be reproduced and re-doing their derivation have showed multiple algebraic mistakes. Whether these are typing mistakes or fundamental mistakes in their equations remains unknown, but their paper is deemed as unusable by the author.

3. Luo and Tong [16] adapted the Goland [82] stress formulation to include the Timoshenko beams instead of the Euler beam for a general bonded, semi-infinitely long joint with thick, thin and negligible adhesive thicknesses. The stress solution is used to find the SERR for the asymmetric CLS specimen from the ATM Round Robin by Johnson [15], the CLS-B specimen, but only the

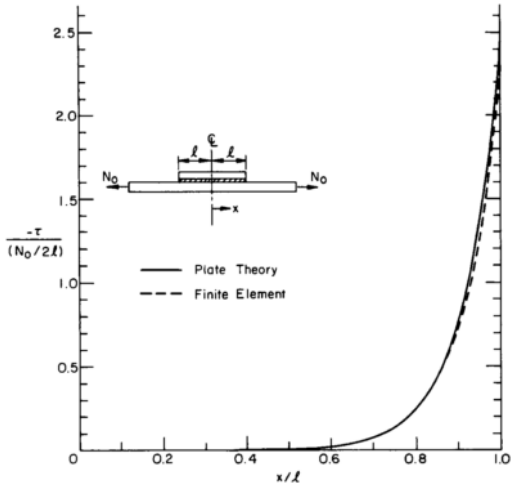

(a) Comparison of the analytical and FEM solution for the adhesive shear stress (from Delale *et al.* [12]).

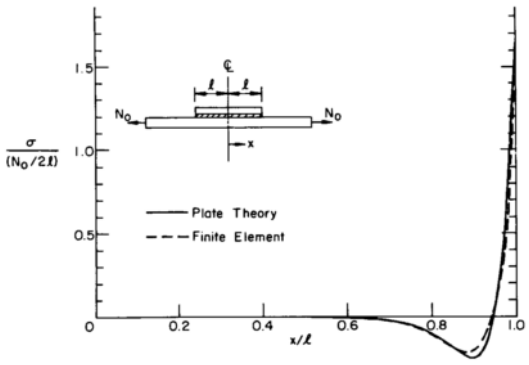

(b) Comparison of the analytical and FEM solution for the adhesive peel stress (From Delale *et al.* [12]).

Figure B.1: Analytical and FEM solutions for the adhesive stresses (from [12]).

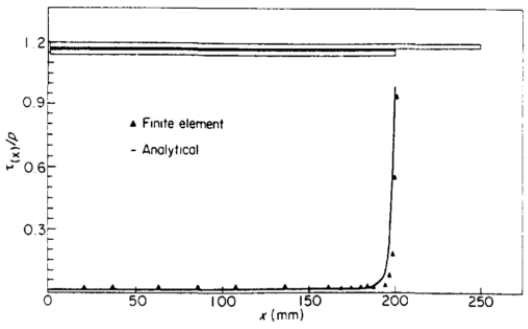

(a) Comparison of the analytical and FEM solution for the adhesive shear stress (from Edde and Verreman [13].)

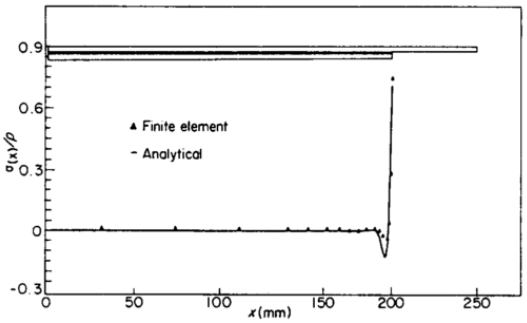

(b) Comparison of the analytical and FEM solution for the adhesive peel stress (From Edde and Verreman [13]).

Figure B.2: Analytical and FEM solutions for the adhesive stresses (from [13]).

SERR results are evaluated. Interestingly, Luo and Tong [16] accounted for the CLS-B clamped-clamped conditions by solving the overlap edge loads using Goland [82] for clamped-clamped boundary conditions from [10] and inputting those loads in the adhesive stress formulations

B.2. Strain Energy Release Rate

In general, the literature has focused on FEM based models to find the SERR in CLS specimen [10, 73]. However, some closed-form solutions have been created over time [13–16, 71, 73, 77].

Brussat *et al.* [71] was the first to create a closed-form solution for the SERR by applying the beam theory for an infinitely long specimen:

$$G = \frac{P^2}{2b_N(EA)_2}\left[1 - \frac{(EA)_2}{(EA)_0}\right] \tag{B.1}$$

where P, b_N, $(EA)_2$ and $(EA)_0$ are the applied load, specimen width, lumped overlap stiffness and free adherend stiffness respectively. The MR was assumed to equal to MR under pure bending moment loading, which is not entirely true. Because of the infinitely long assumption, the SERR and MR are independent from crack length.

Later, an ASTM Round Robin by Johnson [15] aimed to evaluated the State-of-the-Art in SERR calculations for CLS specimen by evaluating various FEM methods and two closed-form solutions [12, 71]. The predictions of Brussat *et al.* [71] matched well with geometric non-linear FEM methods for CLS specimen with identical adherends, but is limited in application due to the infinitely long assumption [15]. The solution of [12] compared well with the prediction of geometric linear FEM solutions, but it was noted by [15] that geometric non-linearity must be included for accurate results.

Edde and Verreman [13] used the Crack-Tip-Closure technique to relate the Mode I and Mode II SERR components to the adhesive stresses as has been done by other authors [19, 87, 88]:

$$\begin{aligned} G_I &= \frac{t_a}{2E_a}\left(\sigma_{max}\right)^2 \\ G_{II} &= \frac{t_a}{2G_a}\left(\tau_{max}\right)^2 \end{aligned} \tag{B.2}$$

where t_a, E_a, G_a, σ_{max} and τ_{max} are the adhesive thickness, Young's Modulus and Shear Modulus, adhesive peel and adhesive shear stress respectively. A major drawback of this method is that the support boundary conditions must be passed onto the SERR through the adhesive stresses. However, only reproducible roller-roller support solutions exist for the SERR specimen.

Fernlund and Spelt [14] and Fernlund *et al.* [77] used the J-integral to calculate the total SERR in a cracked CLS specimen:

$$G = \left[\frac{F_1^2}{2(EA)_1} + \frac{M_1^2}{2D_1}\right]^2 + \left[\frac{F_2^2}{2(EA)_2} + \frac{M_2^2}{2D_2}\right]^2 - \left[\frac{F_0^2}{2(EA)_0} + \frac{M_0^2}{2D_0}\right]^2 \tag{B.3}$$

where F_i, M_i, $(AE)_i$ and D_i are the tensile force, bending moment, tensile stiffness and bending stiffness respectively where $(i = 1, 2, 3)$ as shown in fig. B.3. Note that all units are per unit width. Interestingly to note is that the shear force does not contribute in to the SERR in the formulation of [14, 77] and [77].

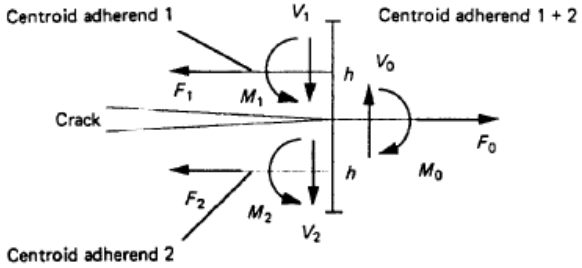

Figure B.3: Cross section at the crack tip of the cracked adhesive overlap sandwich (from Fernlund and Spelt [14]).

For mode partitioning, Fernlund *et al.* [77] evaluated the work of Suo and Hutchinson [89] and Williams [90], whose equations are note shown here due to their complexity, and observed similar results for CLS specimen with identical adherends. [89, 90] ignore the adhesive thickness and assume small deformations, both which are not true in a CLS specimen, so a comparison was made with FEM predictions from [15] which showed an excellent agreement with the non-linear FEM results. Fernlund and Spelt [14] showed that for a CLS specimen with identical adherends the individual mode components can be expressed in a much more convenient way:

$$\begin{aligned} G &= G_I + G_{II} \\ G_I &= \frac{M_2^2}{4D_2} \\ G_{II} &= \frac{F_2^2}{4(EA)_2} + \frac{4M_2^2 - M_0^2}{16D_2} \end{aligned} \tag{B.4}$$

Again, a comparison was made with the results from [15] showing a reasonable agreement with non-linear FEM predictions, shown in fig. B.4, but the results are not as good as the predictions from Fernlund *et al.* [77].

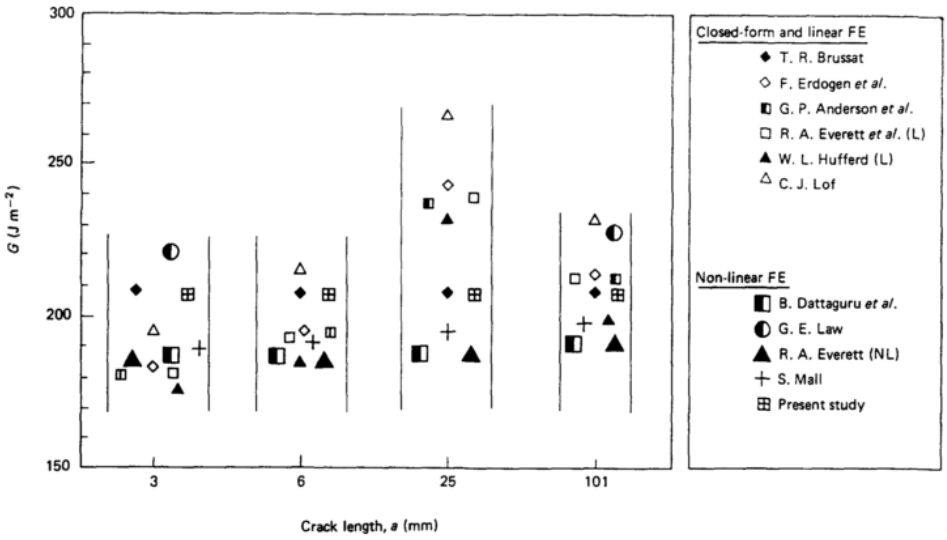

Figure B.4: Comparison of the Strain Energy Release Rate (SERR) calculations from Johnson [15] and [14] for equal adherend, bonded Cracked Lap Shear (CLS) specimen (from Fernlund and Spelt [14]).

Lai *et al.* [73] used the method of Suo and Hutchinson [89] for the total SERR and mode partitioning for CLS specimen with nonidentical adherends. They used the Goland [82] framework to express the overlap loads for roller-roller, clamped-clamped and clamped-roller boundary conditions which can be passed into the solution of the SERR. Comparison of the model using different boundary conditions with FEM solutions gave a reasonable to good fit. It is important to note that the clamped-clamped boundary condition solutions could not be reproduced, likely due to a typing mistake in the equations.

Luo and Tong [16] applied the J-integral along path 1 in fig. B.5 to achieve the same expression for the SERR as Edde and Verreman [13] given in eq. (B.2). Separate solutions are given for (1) bonded joints with thick adhesives, (2) bonded joints with thin adhesives and (3) interlaminar delamination, where the adhesive thickness approaches zero, by deriving adhesive stress solutions for each problem and inputting those in eq. (B.2). Comparison with the results from the asymmetric CLS specimen CLS-B from Johnson [15] shows a slight over estimation of the total SERR, but the predicted MR show a good fit. Clamped-clamped conditions could be accounted for as the overlap loads can be solved using existing solutions [10, 73] and the stress formulation is independent of support conditions due to the semi-infinite long joint assumption.

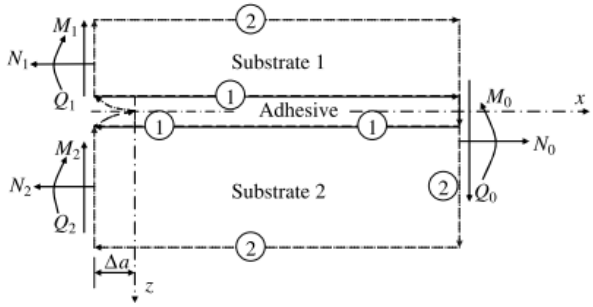

Figure B.5: J-integral paths 1 and 2 (from Luo and Tong [16]).

C

Fatigue Load Selection Approach

As discussed in chapter 4, fatigue tests are performed at Constant Amplitude (CA) loading with a fixed R-ratio and loading frequency. The R-ratio and loading frequency can be selected based on best practices in fatigue testing of disbond growth. The fatigue load however, must be determined based on the needs of this research.

To fully characterize the effect of a Disbond Arrest Features (DAF) on disbond growth, a meaningful disbond length and number of load cycles must be reached before the initiation of fatigue damages in the adherend. To increase the disbond length that can be achieved, the fatigue load could be increased so that the Disbond Growth Rate (DGR) becomes higher. At the same time however, increasing the fatigue load will also decrease the number of load cycles until fatigue crack initiation. Lowering the fatigue load has a similar effect; the maximum number of load cycles increases, but the DGR decreases.

The geometric non-linear behavior of the Cracked Lap Shear (CLS) specimen makes it difficult to estimate the net change in the disbond length that can be achieved when changing the fatigue load. At the time of selecting the fatigue load the model capable of making that prediction was not yet finished. As a result, the fatigue loads are determined experimentally.

The process of finding the optimum fatigue loads is described in this chapter for the adhesive and prepreg bond line specimens separately.

C.1. Adhesive Bond Line Specimens

The upper threshold of the fatigue load range is defined by the yield strength of the Fibre Metal Laminate (FML) adherend. Under pure tensile loading, the yield strength can readily be calculated using the ply properties and the Mixed Volume Fraction (MVF) rule [48]. In the case of a CLS specimen however, secondary bending exists which lowers the total load at which the FML will start to yield. Therefore, a static test was performed with specimen 2_01 and the results are shown in fig. C.1.

The load at which yielding starts to occur is characterized by the transition to the second, shallower slope of the force-displacement curve [48]. This transition was found to occur at an applied load of approximately 30 kN. At 63.45 kN the static strength of the specimen is reached and unstable disbond growth is initiated which continues until both adherends are completely disbonded. Beyond this point the slope of the force-displacement curve is defined by the stiffness of a single adherend that has yielded.

Initially, it was planned to test at 30% of the static strength, 19 kN, which is somewhat similar to [5] and [7], but this did not result in disbond growth. Therefore, a specimen was tested at 30 kN and the load was lowered to 26 kN in steps of 1 kN. The fatigue load of 26 kN was selected because it is the lowest load at which disbond growth was observed. The number of load cycles until fatigue crack

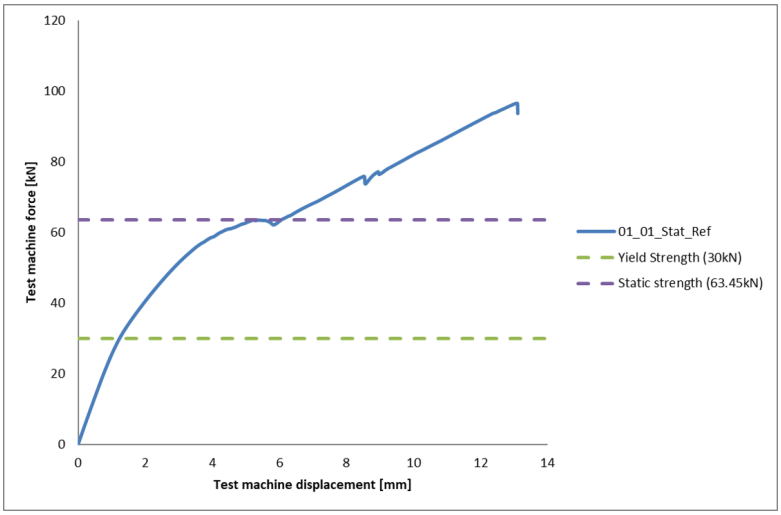

Figure C.1: Results of the static test - specimen 2_01.

initiation is not evaluated with this approach due to time constraints.

A similar test program that started at 26 kN and planned to move up to 30 kN at steps of 1 kN failed to initiate a disbond at 26 kN. Therefore, a fatigue load of 28 kN will be applied first to ensure the disbond initiation.

The determination of the fatigue load is considered a weak point of this research by the author. Mishaps and time constraints limited to lowest fatigue load to be tested to 26 kN. Future work with similar specimens is advised to investigate loads lower than 26 kN. This is because these lower loads seem to result in a more favourable fatigue life of the adherends. Additionally, it is advised to test one load per specimen so that the achievable disbond length can be obtained.

C.2. Prepreg Bond Line Specimens

The lower resistance to disbond growth of the prepreg bond line eliminates the problem that a minimum disbond length cannot be achieved before the initiation of fatigue damages in the adherends.

A fatigue load of 16.5 kN was selected as this would result in roughly 2.5x the DGR in the adhesive bond line specimens at 26 kN according to model predictions. The higher DGR was requested to reduce the total test time per specimen.

Additionally, fatigue loads of 19.5 and 21 were selected. The increase per step was decreased from 3 to 1.5 because of the exponential relation between the applied load and the DGR and the number of loads cycles until fatigue crack initiation.

D

Clamping Pressure Selection Approach

The applied clamping pressure must be determined for the Clamped Disbond Arrest Feature (CDAF). It was decided to select a clamping pressure that equals the pressure exerted by the fastener head of the 4.8 mm titanium Hi-Lok used as Bolted Disbond Arrest Feature (BDAF).

First, the clamping pressure of the Hi-Lok must be determined. The clamping pressure exerted by the CDAF is delivered by a bolt. The second step is to find the bolt torque that results in a clamping pressure similar to that of the Hi-Lok head.

D.1. Hi-Lok Clamping Pressure Determination

The determination of the clamping pressure exerted by the Hi-Lok fastener head is discussed here. First the equations are explained followed by the measurements and the results.

Equations

The dimensions needed for the calculations of the clamping load as proposed by Bickford [17] are visualized in fig. D.1. The dimensions and features shown in blue have been added by the author. The purpose of all dimensions will be explained throughout the calculations procedure.

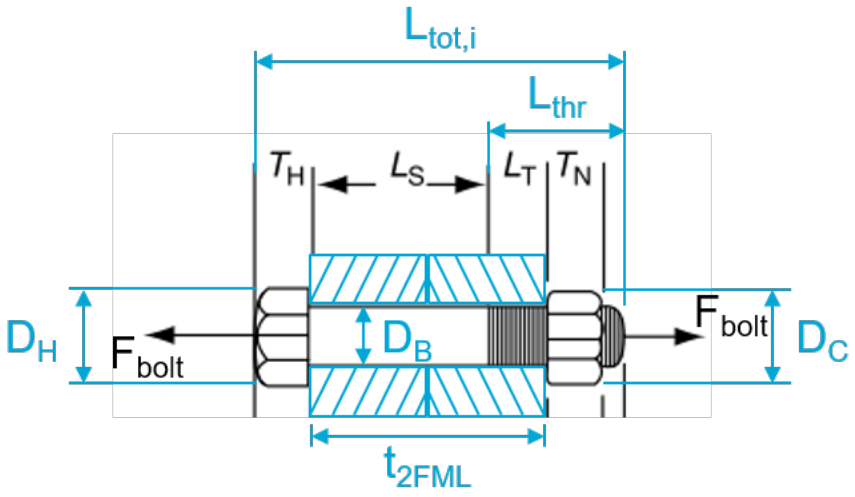

Figure D.1: Bolt dimensions (obtained from Bickford [17] and adjusted by the author; adjustments made in blue).

According to [17], the relation between the bolt load F_{bolt} [N] and the elongation of of the bolt ΔL_{tot} [mm] can be approximated by;

$$\Delta L_{tot} = F_{bolt}\left(\frac{L_{be}}{EA_B} + \frac{L_{se}}{EA_S}\right) \tag{D.1}$$

where L_{be} [mm] is the effective length of the body, L_{se} [mm] is the effective length of the threads, A_S [mm^2] is the effective stress area of the threads, A_B [mm^2] is the cross-sectional area of the bolt shank and E [MPa] is the material Young's Modulus. The elongation ΔL_{tot} can be obtained by measuring the total length of the bolt before and after installing. If all the other parameters can be obtained experimentally, then the bolt load F_{bolt} can be solved.

The parameters L_{be} and L_{se} are calculated using [17];

$$L_{be} = L_S + \frac{T_H}{2} \tag{D.2}$$

$$L_{se} = L_T + \frac{T_N}{2} \tag{D.3}$$

where L_S [mm], L_T [mm], T_H [mm] and T_N [mm] are depicted in fig. D.1. The parameters A_B [mm^2] and A_S [mm^2] are calculated using [17];

$$A_B = \frac{1}{4}\pi D_B^2 \tag{D.4}$$

$$A_S = 0.7854\,(D_B - 0.938p)^2 \tag{D.5}$$

where p [mm^{-1}] is the pitch of the threads which is calculated by [17];

$$p = \frac{N_{thr}}{L_{thr}} \tag{D.6}$$

where N_{thr} [-] is the number of threads and L_{thr} [mm] is the length of the threaded bolt section. It is noted that the expression for A_S in eq. (D.4) is derived for a standard 60° thread, but the thread of the Hi-Lok is unknown. This uncertainty was accepted as the calculations aim to give a ballpark figure of the bolt load.

All the parameters mentioned above can be measured except for the exposed threaded section of the bolt L_T. This can be calculated using the thickness of the two FML adherends with the bond line interface t_{2FML} and the length of the body L_S;

$$L_T = t_{2FML} - L_S \tag{D.7}$$

It is noted that this solution ignores the compression of the adherends and the stretch of the bolts when a state of static equilibrium is achieved. Again, these limitations are accepted given the accuracy required from the calculation.

The bolt load can now be calculated. The pressure exerted by the fastener head $F_{c,head}$ [MPa] and the collar $F_{c,collar}$ [MPa] is then calculated by dividing the bolt load by the area of the fastener head or collar that exerts the pressure onto the adherend surface;

$$F_{c,head} = \frac{F_{bolt}}{\frac{\pi}{4}\left(D_H^2 - D_B^2\right)} \tag{D.8}$$

$$F_{c,collar} = \frac{F_{bolt}}{\frac{\pi}{4}\left(D_C^2 - D_B^2\right)} \tag{D.9}$$

where F_{bolt} [N] is the bolt load, D_H [mm], D_B [mm] and D_C [mm] are the head, body and collar diameter respectively.

Measurements

The bolt length were measured using a micrometer as depicted in fig. D.2. All other dimensions were measured using a digital caliper. Six bolts were installed in the overlap section of a CLS specimen with an adhesive bond line. The results of the measurements are summarized in table D.1.

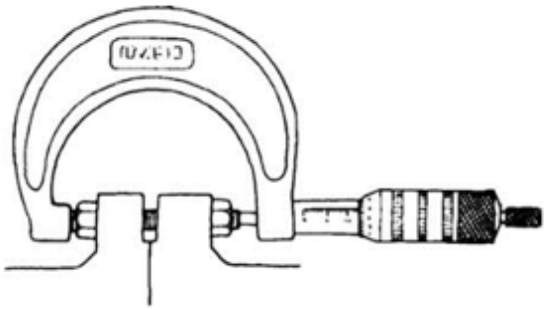

Figure D.2: Illustration of a micrometer.

Table D.1: Results of the measurements. Note: $L_{tot,0}$ and $L_{tot,1}$ are the total bolt length before and after installation respectively.

Bolt	D_H [mm]	D_C [mm]	D_B [mm]	L_H [mm]	T_N [mm]	L_{thr} [mm]	$L_{tot,0}$ [mm]	$L_{tot,1}$ [mm]	N_{thr} [-]	t_{2FML} [mm]
1	9.29	7.74	4.80	1.71	6.87	7.87	14.91	14.95	9.00	4.83
2	9.25	7.77	4.80	1.77	6.87	7.87	14.93	14.98	9.00	4.83
3	9.28	7.74	4.80	1.75	6.87	7.87	14.87	14.91	9.00	4.83
4	9.29	7.74	4.80	1.78	6.87	7.87	14.92	14.96	9.00	4.82
5	9.31	7.74	4.80	1.76	6.87	7.87	14.94	14.99	9.00	4.82
6	9.31	7.74	4.80	1.77	6.87	7.87	14.92	14.96	9.00	4.76

Results

Using the previously stated equations and the measured dimensions, the bolt load F_{bolt}, the pressure exerted by the head $F_{c,head}$ and the pressure exerted by the collar $F_{c,collar}$ have been calculated. The intermediate and final calculation results are summarized in table D.2. The Ti 6Al-4V titanium properties were used for the Hi-Lok: E = 113,800 MPa and σ_{yield} = 880 MPa [91].

Table D.2: Calculated results of the bolted load F_{bolt} and the clamping pressure exerted by the bolt head $F_{c,head}$ and the collar $F_{c,collar}$.

Bolt	p [1/mm]	A_H [mm^2]	A_C [mm^2]	A_B [mm^2]	A_S [mm^2]	L_T [mm]	L_{bc} [mm]	L_{se} [mm]	ΔL_{tot} [mm]	F_{bolt} [N]	$F_{c,head}$ [MPa]	$F_{c,collar}$ [MPa]
1	0.87	49.69	28.96	18.10	12.44	-0.50	6.19	2.93	0.04	8076.71	162.55	278.93
2	0.87	49.11	29.32	18.10	12.44	-0.47	6.18	2.97	0.05	9217.38	187.71	314.36
3	0.87	49.54	28.96	18.10	12.44	-0.43	6.13	3.01	0.03	6271.86	126.60	216.60
4	0.87	49.69	28.96	18.10	12.44	-0.45	6.16	2.98	0.04	7844.24	157.87	270.90
5	0.87	49.98	28.96	18.10	12.44	-0.50	6.20	2.93	0.04	7868.08	157.43	271.73
6	0.87	49.98	28.96	18.10	12.44	-0.53	6.17	2.91	0.04	7324.09	146.54	252.94

Based on these results, an average F_{bolt}, $F_{c,head}$ and $F_{c,collar}$ were found of 7767.06 [N], 156.45 [MPa] and 267.58 [MPa] respectively. A sanity check was performed by calculating the stresses in the bolt as a percentage of the titanium yield stress.

The results are summarized in table D.3 which shows that bolt is loaded at 57.3% to 84.2% of the material yield strength in the threaded section of the bolt. These values are within reasonable expectations of an installed bolt.

Table D.3: Calculated loads in the body $\%_{yield,B}$ and threaded $\%_{yield,S}$ bolt sections as a percentage of the material yield strength.

Bolt	AB [mm^2]	A_s [mm^2]	F_{bolt} [N]	S_B [MPa]	S_S [MPa]	$\%_{yield,B}$	$\%_{yield,S}$
1	18.10	12.44	8076.71	446.34	649.27	50.72%	73.78%
2	18.10	12.44	9217.38	509.37	740.97	57.88%	84.20%
3	18.10	12.44	6271.86	346.60	504.18	39.39%	57.29%
4	18.10	12.44	7844.24	433.49	630.59	49.26%	71.66%
5	18.10	12.44	7868.08	434.81	632.50	49.41%	71.88%
6	18.10	12.44	7324.09	404.74	588.77	45.99%	66.91%

D.2. Applied Torque for the Clamped Disbond Arrest Feature

The clamping pressure exerted by the Clamped Disbond Arrest Feature (CDAF) is controlled by a bolt and the applied bolt torque. To measure the clamping pressure, two Fujifilm Prescale Pressure Films capable of measuring the pressure range of 50-130 MPa [92] and 130-300 MPa [93] were placed between the adherend surfaces and the CDAF. The applied bolt torque was controlled using a torque wrench. It was found that an applied torque of 5 Nm resulted in a uniform pressure of 100-200 MPa across the surface of the clamps. Further increasing the bolt torque was not possible as it led to significant deformations of the CDAF.

In conclusion, a bolt torque of 5 Nm is selected to apply the clamping pressure of the CDAF. This results in a uniform pressure range of 100-200 MPa. This is somewhat comparable to the average pressure of 156.45 [MPa] and 267.58 [MPa] exerted by the bolt head and collar of the BDAF.

E

Disbond Growth Model: Numerical Implementation

The solution was implemented in MATLAB and can be accessed via the online repository [80]. A flow diagram in fig. E.1 gives an illustrative overview of the numerical implementation.

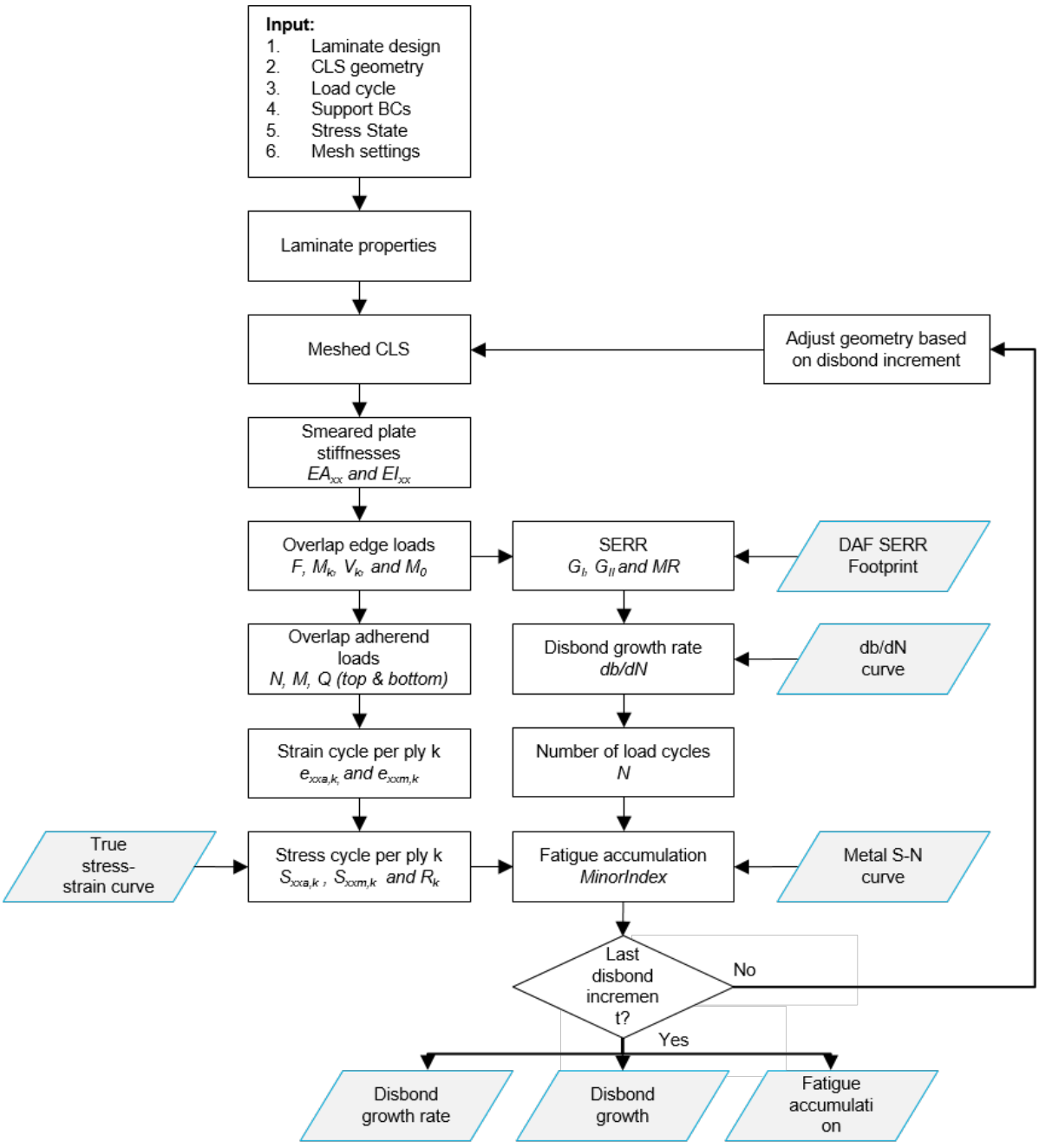

Figure E.1: Flow diagram of the quasi analytical disbond growth model.

F

DIC Processing Algorithm: From Strain Field to Disbond Area

A processing algorithm has been developed with the aim of finding the disbonded region based on the strain field measured using Digital Image Correlation (DIC). It was observed in fig. 5.12 that the strain field in the top ply of the top adherend exhibits a distinctive valley that coincides with the disbond front. This implies that the disbond length can be found if the valley can be located in the measured strain field.

The processing algorithm will be explained here by walking through the processing steps.

Step 1 - Interpolation

The first step is to interpolate the raw DIC data over a (x, z) mesh grid using a linear interpolation method as shown in fig. F.1. This must done because the coordinates of the DIC data, (x_{DIC}, z_{DIC}), are irregular and do not represent mesh which is needed for the next steps. During the interpolation the (x_{DIC}, z_{DIC}) reference frame is translated so that it coincides with the (x, z) reference frame.

Note that the data gap created by the fastener head in the raw data is filled during the interpolation. Before the interpolation is performed, a mask is created for these empty data points to ensure that they do not influence the interpolated values at the fastener head boundaries. The filled data points will be later removed.

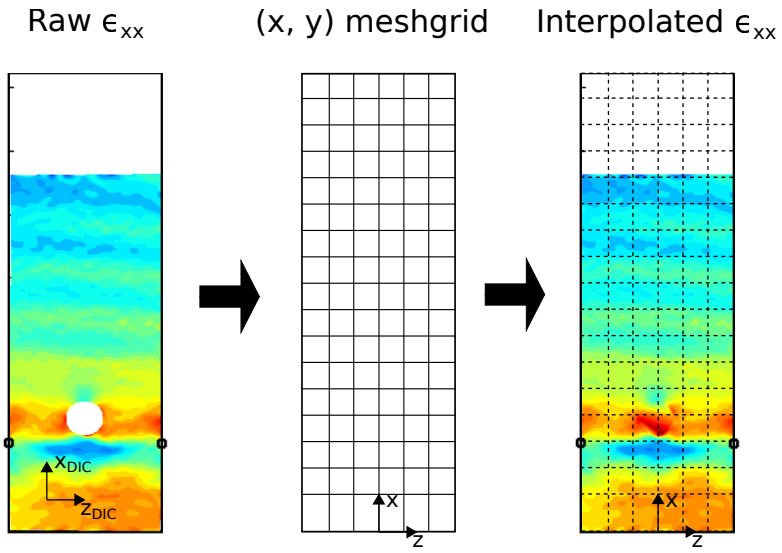

Figure F.1: Processing algorithm step 1 - Interpolation of the raw DIC ϵ_{xx} data.

Step 2 - Locating the disbond front

The next step is to locate the disbond front along all z_i slices by analyzing the strain ϵ_{xx} distribution as shown in fig. F.2. In order to do so, the algorithm must find the valley that corresponds to the disbond front location. This is achieved by calculating the difference between each local maximum and the preceding local minimum. The maximum value of the difference generally corresponds to the right wall of the valley; the corresponding local minimum is the location of the disbond front. Using this rule, it is possible that a lower lower local minimum exists in front of the identified local minimum. Therefore, a check is included that corrects the identified local minimum should this be the case. An example of such a correction is shown in fig. F.2.

Note that in this processing step the data gap created by the Hi-Lok head (see above) is still filled. The area of the Hi-Lok head will be removed in the next step when the disbonded area is calculated.

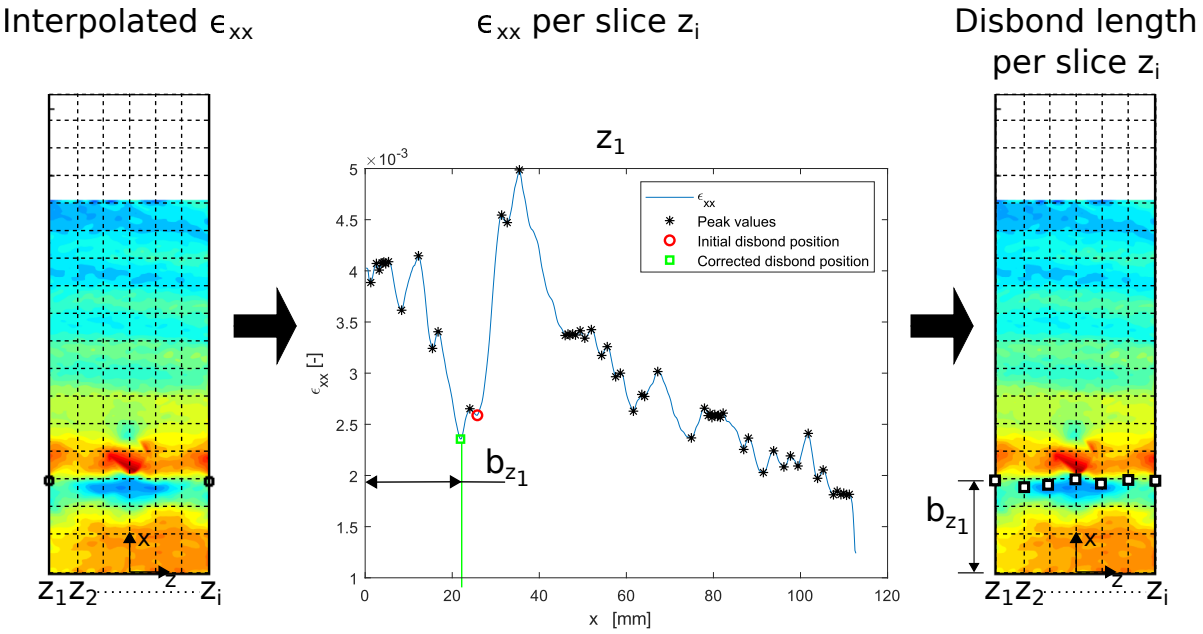

Figure F.2: Processing algorithm step 2 - Disbond front location.

Step 3 - Disbond area

After locating the disbond front, the disbond area is found by assuming that the entire region below the disbond front has been disbonded. The result is shown in fig. F.3.

Step 4 - Final output and verification

The disbond area results of specimen 2_13 are shown in fig. F.4 to give an example. The actual disbond length measured by the visual inspection has been included to verify the final results. Both results show an excellent match thereby confirming the surprising accuracy of the algorithm.

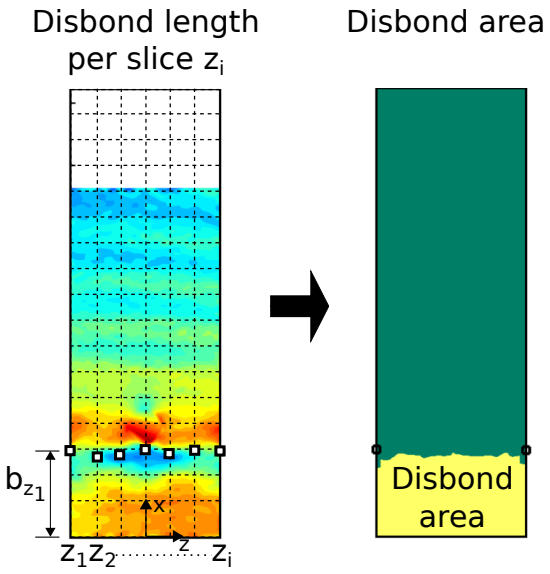

Figure F.3: Processing algorithm step 3 - Disbond area.

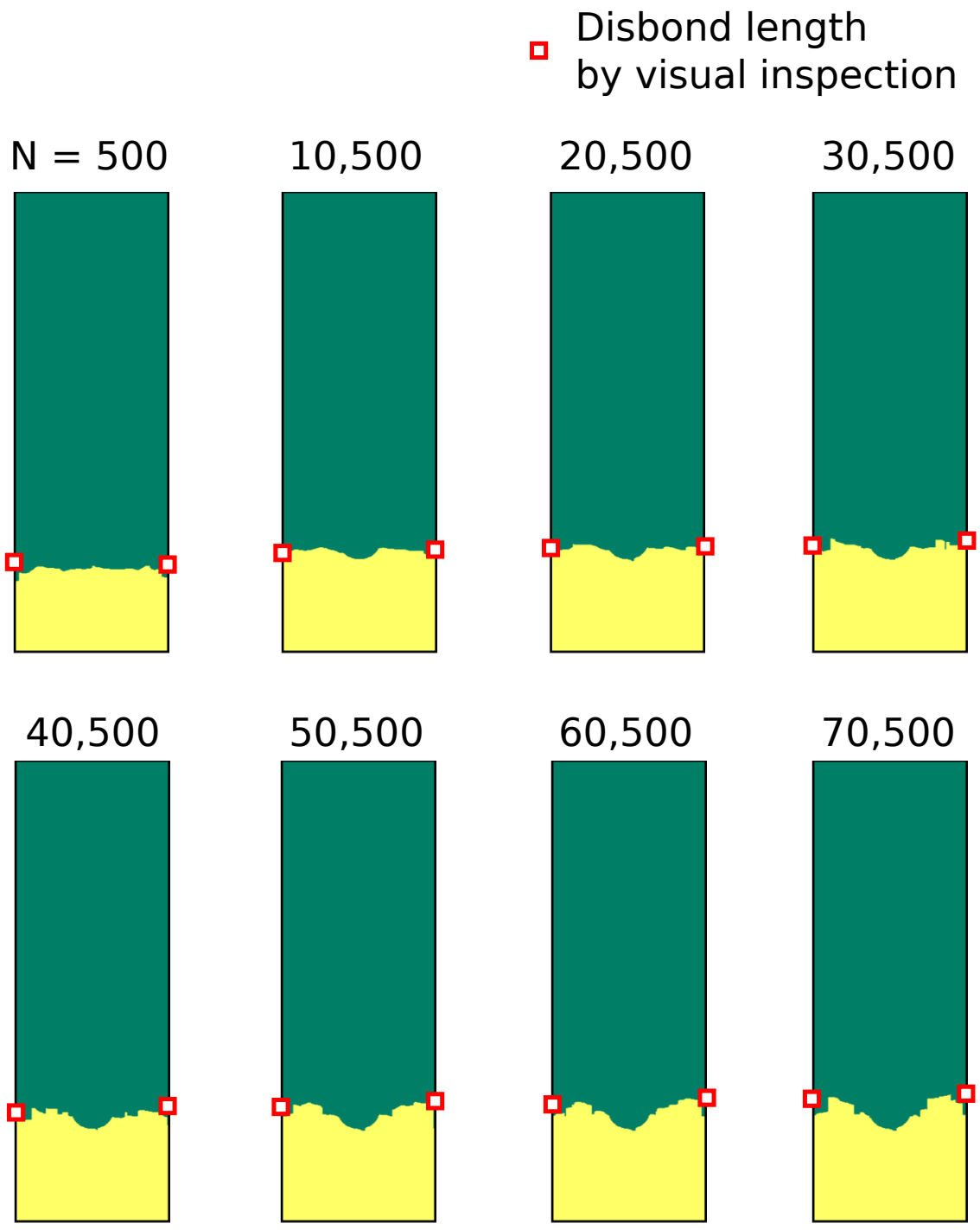

Figure F.4: Disbond area development - 2_13.

G

Prepreg Paris Law Coefficient Determination

The Mode I and Mode II Paris Law type of coefficients of the UD S2 FM94 GF prepreg interface bonded to a Aluminum 2024-T3 adherend have been determined by Delgrange [18] and Alderliesten [43] respectively. These must be adjusted to the coefficients of the Mixed Mode (MM) disbond growth model as proposed by Bürger [8]. The calculations are discussed here and consist of three steps: (1) adjusting the Mode I coefficients, (2) adjusting the Mode II coefficients and (3) re-fitting the Paris Law type of coefficients for Mode II using the exponent from Mode I as required by Bürger [8].

The fracture parameter proposed by Bürger [8] $\Delta\sqrt{G_{eq,1}}$ is calculated by;

$$\Delta\sqrt{G_{eq,1}} = \left(\sqrt{G_{eq1,max}} - \sqrt{G_{eq1,min}}\right)^2 \tag{G.1}$$

with

$$\sqrt{G_{eq1,max}} = \frac{\sqrt{G_{I,max}}}{2} + \sqrt{\frac{G_{I,max}}{2} + G_{II,max}} \tag{G.2}$$

$$\sqrt{G_{eq1,min}} = \frac{\sqrt{G_{I,min}}}{2} + \sqrt{\frac{G_{I,min}}{2} + G_{II,min}} \tag{G.3}$$

G.1. Step 1: Mode I Coefficients

The Mode I Paris Law type of curves were created by fatigue testing Double Cantilever Beam (DCB) specimens with GLARE 2A-2/2-0.4 adherends at Constant Amplitude (CA) loading with a fixed R-ratio of 0.1. The results are shown in fig. G.1. The Linear Elastic Fracture Mechanics (LEFM) parameter used in fig. G.1 is;

$$\Delta G = \left(\sqrt{G_{max}} - \sqrt{G_{min}}\right)^2 \tag{G.4}$$

According to Delgrange [18], the best fit Power Law coefficients are: $C_d = 5.15 \cdot 10^{-12}$ and $n_d = 4.34$ for G in (J/m^2) and b in (mm). It was observed by the author that it was not possible to obtain these coefficients when using the data of all specimens as shown in fig. G.2(a). This issue was not documented by Delgrange [18] and it remains unknown whether all or some of the specimens were used for curve fitting. By trial and error it was found that only using the data of specimens 3 and 4 resulted in coefficients that approach the given values of Delgrange [18]. Therefore, only specimen 3 and 4 are used to calculate $\Delta\sqrt{G_{eq,1}}$, but the reader must be aware of this deficiency.

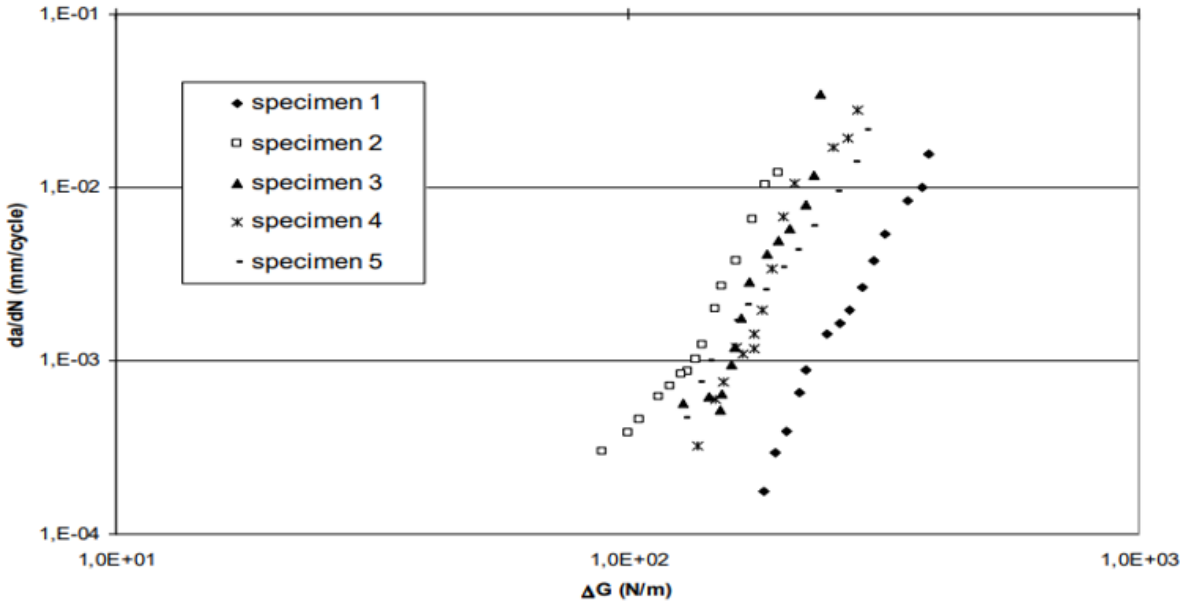

Figure G.1: Mode I Paris Law type of curve obtained using DCB specimens with 2A-2/2-0.4 adherends that were fatigue tested at CA loading with a fixed R-ratio of 0.1 (from Delgrange [18]).

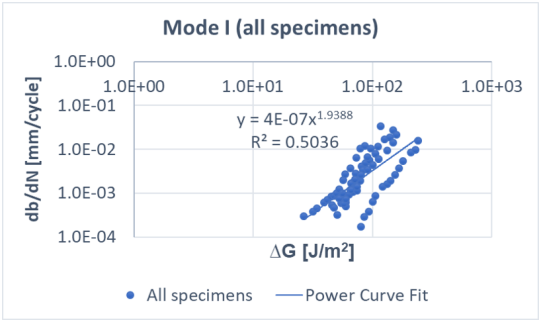

(a) Power Law curve fit using all specimens from [18]: $C_d = 4.32 \cdot 10^{-7}$ and $n_d = 1.94$ for G in (J/m^2) and b in (mm).

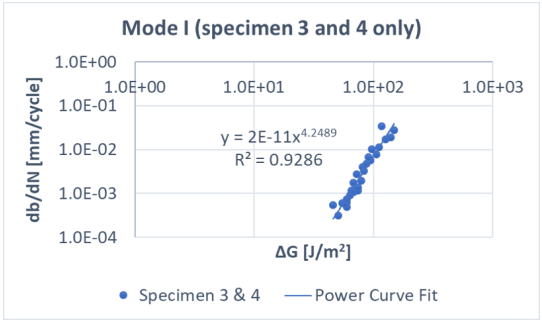

(b) Power Law curve fit using all specimen 3 and 4 from [18]: $C_d = 3.21 \cdot 10^{-11}$ and $n_d = 4.25$ for G in (J/m^2) and b in (mm).

Figure G.2: Reproducing the given Paris-type curve fit (from Delgrange [18]).

The data was extracted from fig. G.1 manually with a pixel based tool. Using the relation $G_{min} = G_{max} \cdot R^2$ with eq. (G.1) and eq. (G.2) the values of ΔG are converted to $\Delta\sqrt{G_{eq,1}}$ and the results are shown in fig. G.3.

Using the Excel Power curve fit, the coefficients were determined to be: $C_{0\%} = 2.77 \cdot 10^{-13}$ and $m_{0\%} = 4.95$ for G_{eq1} in (J/m^2) and b in (mm). Note the that m is instead of n for the exponent and the subscript 0% represents the value of the Mode Ratio (MR) [8].

G.2. Step 2: Mode II coefficients

The results of the Mode II delamination growth testing campaign by Alderliesten [19] are shown in fig. G.4.

In this case, the fracture parameter $\sqrt{G_{max}} - \sqrt{G_{min}}$ has been used. By taking the square of the fracture parameter the coefficient $\Delta\sqrt{G_{eq,1}}$ can be calculated with the same equations as was done for Mode I (see above). The results are shown in fig. G.5.

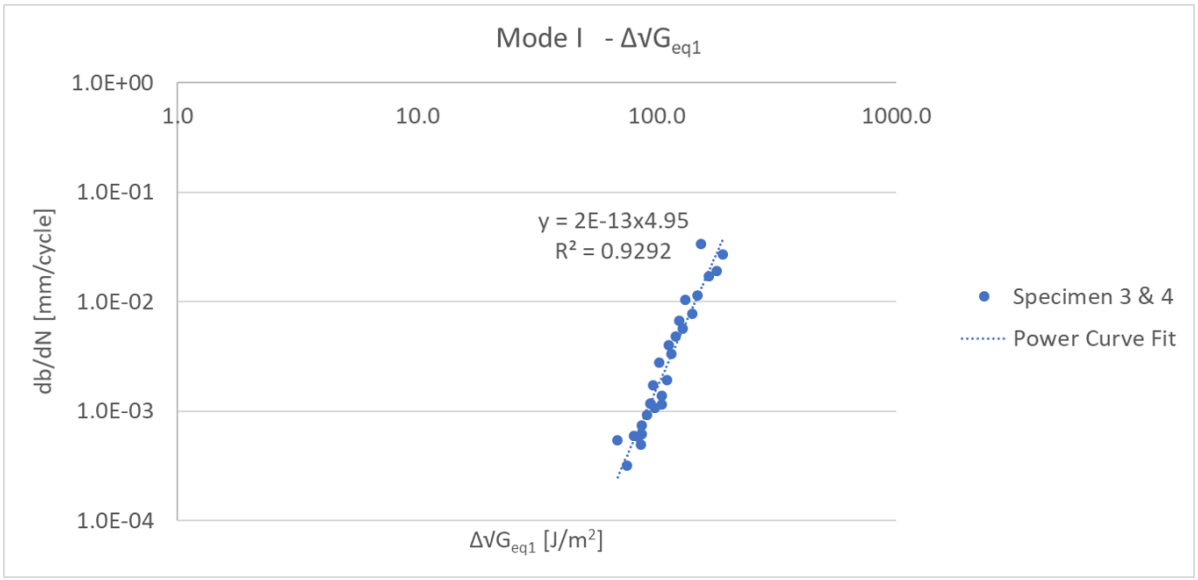

Figure G.3: Mode I Paris Law type of curve with $\Delta\sqrt{G_{eq,1}}$.

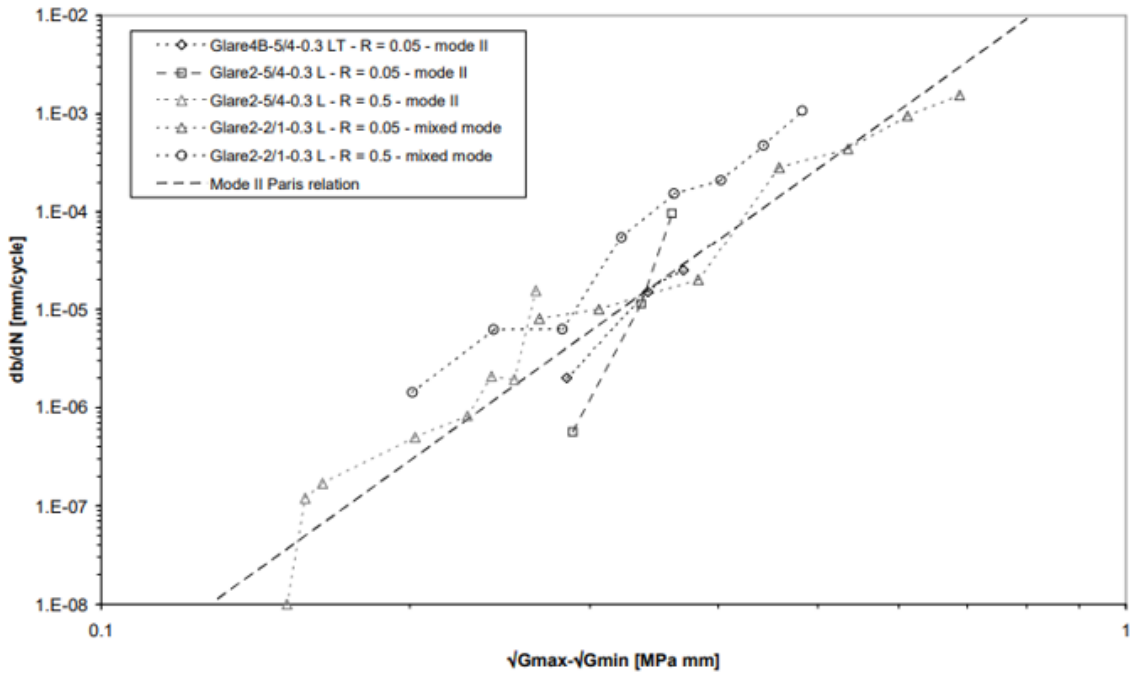

Figure G.4: Mode II Paris Law type of curve (from Alderliesten [19]).

Using the Excel Power curve fit, the coefficients were determined to be: $C_{100\%} = 6.40 \cdot 10^{-13}$ and $m_{100\%} = 3.67$ for G_{eq1} in (J/m^2) and b in (mm). Note the that m is used instead of n for the exponent and the subscript 100% represents the value of the Mode Ratio (MR) [8].

G.3. Step 3: Re-fitting Mode II using the Mode I Exponent

The MM disbond growth model from Bürger [8] requires the Mode II Paris Law type of curve to be fitted using the exponent from Mode I $m_{0\%}$. Using the value of $m_{0\%}$ that was found a new Power Law fit is performed and the results are shown in fig. G.6.

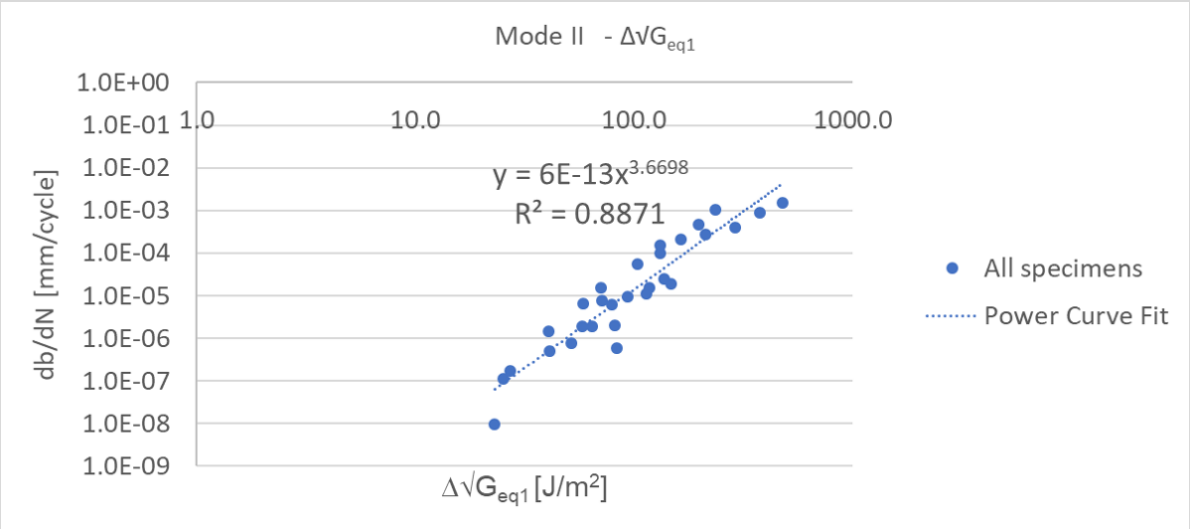

Figure G.5: Mode II Paris Law type of curve with $\Delta\sqrt{G_{eq,1}}$.

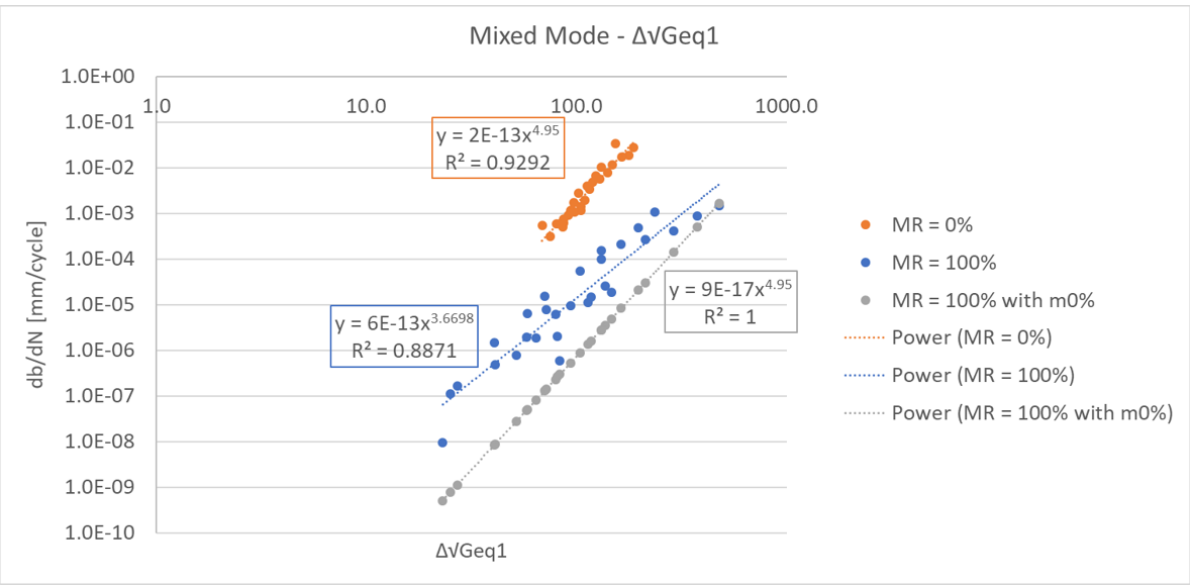

Figure G.6: Final Mode I and Mode II Paris Law type of curve with $\Delta\sqrt{G_{eq,1}}$.

The final coefficients are given in table G.1.

Table G.1: Adhesive and prepreg bond line material fracture parameters for the MM disbond growth model of Bürger [8] with G_{eq1} in (J/m²) and b in (mm).

Coefficient	Value
$C_{0\%}$	$2.77{\cdot}10^{-13}$
$C_{100\%}$	$9.21{\cdot}10^{-17}$
$m_{0\%}$	4.95

Bibliography

[1] R. Alderliesten, *Damage tolerance of bonded aircraft structures,* International Journal of Fatigue **31**, 1024 (2009).

[2] K. Y. Lin, L. Richard, and C. H. E. Cheung, *Delamination/disbond arrest features in aircraft composite structures,* (2018), DOT/FAA/TC-18/5, available on URL:http://www.tc.faa.gov/its/worldpac/techrpt/tc18-5.pdf.

[3] T. Kruse, T. Körwien, S. Heckner, and M. Geistbeck, *Bonding of cfrp primary aerospace structures - crack stoppings in composite bonded joints under fatigue,* (2015) available on URL:http://iccm20.org/fullpapers/file?f=KEBWMmg6Lm.

[4] R. Sachse, K. a. Pickett, W. Adebahr, M. Klein, and P. Middendorf, *Experimental investigation of mechanical fasteners regarding their influence on crack growth in adhesively bonded cfrp-joints subjected to fatigue loading,* (2015) available on URL:http://www.iccm-central.org/Proceedings/ICCM20proceedings/papers/paper-1118-3.pdf.

[5] T. Kruse, *Fatigue behavior and damage tolerant design of bonded joints for aerospace application on fiber metal laminates and composites,* (2017) available on URL:https://calvinrans.com/pubs/.

[6] L. I. Richard, *Delamination Arrest by Fasteners in Aircraft Structure Under Static and Fatigue Loading*, Ph.D. thesis, University of Washington (2017), available on URL:https://digital.lib.washington.edu/researchworks/handle/1773/39923.

[7] R. Hanx, *Disbond arrest in fibre metal laminates*, Master's thesis, Delft University of Technology (2017), available on https://repository.tudelft.nl/islandora/object/uuid%3Aed61399b-a656-4126-99b6-14461bfb09f4?collection=education.

[8] D. Bürger, *Mixed-Mode Fatigue Disbond on Metallic Bonded Joints*, Ph.D. thesis, Delft University of Technology (2015), available at https://repository.tudelft.nl/islandora/object/uuid%3Aec4dbcd6-052d-4009-bf9e-cdcbf4614174?collection=research.

[9] A. Poulis, *Adhesive bonding - structures and stresses,* (2014).

[10] L. F. M. Da Silva and A. Öchsner, *Modeling of adhesively bonded joints* (Springer, 2008).

[11] M. Banea and L. F. da Silva, *Adhesively bonded joints in composite materials: an overview,* Proceedings of the Institution of Mechanical Engineers, Part L: Journal of Materials: Design and Applications **223**, 1 (2009).

[12] F. Delale, F. Erdogan, and M. Aydinoglu, *Stresses in adhesively bonded joints: a closed-form solution,* Journal of Composite Materials **15**, 249 (1981).

[13] F. Edde and Y. Verreman, *On the fracture parameters in a clamped cracked lap shear adhesive joint,* International journal of adhesion and adhesives **12**, 43 (1992).

[14] G. Fernlund and J. Spelt, *Failure load prediction of structural adhesive joints: Part 1: Analytical method,* International Journal of Adhesion and Adhesives **11**, 213 (1991).

[15] W. S. Johnson, *Stress analysis of the cracked-lap-shear specimen: an astm round-robin,* Journal of testing and evaluation **15**, 303 (1987).

[16] Q. Luo and L. Tong, *Fracture prediction of adhesively bonded structures using energy release rates,* Journal of Adhesion Science and Technology **23**, 1415 (2009).

[17] J. H. Bickford, *Introduction to the Design and Behavior of Bolted Joints* (Taylor & Francis Group, 2008).

[18] G. Delgrange, *Delamination behaviour of bonded structures and hybrid materials,* (2010), report B2v-10-01.

[19] R. Alderliesten, *Delamination growth at bonded interfaces,* (2002).

[20] R. Alderliesten, *Fatigite crack propagation and delamination growth in Glare,*, Ph.D. thesis, Delft University of Technology (2005), available on URL:https://repository.tudelft.nl/islandora/object/uuid%3A15006e44-1232-4ef2-87bd-776b249d61f5.

[21] Cytec, *Fm94 adhesive material technical data sheet*, Tech. Rep. (2010).

[22] *"boeing 787 - from the ground up",* Available on http://www.boeing.com/commercial/aeromagazine/articles/qtr_4_06/article_04_2.html.

[23] *"the black gold of stade",* Available on https://magazin.lufthansa.com/xx/en/nonstop-you-more-than-just-a-good-flight/the-black-gold-a350/.

[24] *"c series earns its wings",* Available on https://www.aero-mag.com/bombardier-c-series-cs100/.

[25] K. Y. Lin and A. V. Styuart, *Probabilistic approach to damage tolerance design of aircraft composite structures,* Journal of Aircraft **44**, 1309 (2007).

[26] FAA, *U.S. Department of Transportation Federal Aviation Administration (FAA). Advisory circular - composite aircraft structure. AC-107B*, Tech. Rep. (NATIONAL AERONAUTICS AND SPACE ADMINISTRATION HAMPTON VA LANGLEY RESEARCH CEN TER, 2009).

[27] C. H. E. Cheung and K. Y. Lin, *Numerical analysis of fastener delamination/disbond arrest mechanism in aircraft composite structures,* Journal of aircraft **49**, 630 (2012).

[28] G. Phillip, *Experimental and Analytical Study of Mode II Interlaminar Failure of Bolted and Bonded Composite Structures*, Master's thesis, University of Washington (2012), available on URL:https://digital.lib.washington.edu/researchworks/handle/1773/20278.

[29] C. H. E. Cheung, P. Gray, and K. Y. Lin, *Design and optimization of an axial mode ii crack arrest specimen,* in *53rd AIAA/ASME/ASCE/AHS/ASC Structures, Structural Dynamics and Materials Conference 20th AIAA/ASME/AHS Adaptive Structures Conference 14th AIAA* (2012) p. 1892.

[30] E. Bruun, C. H. Cheung, P. Gray, and K. Y. Lin, *Design and experimental validation of a mixed-mode crack arrest specimen,* in *53rd AIAA/ASME/ASCE/AHS/ASC Structures, Structural Dynamics and Materials Conference 20th AIAA/ASME/AHS Adaptive Structures Conference 14th AIAA* (2012) p. 1696.

[31] L. I. Richard, *Experimental and Analytical Study of Delamination Arrest by Multiple Fasteners in Composite Structures*, Master's thesis, University of Washington (2013), available on URL:https://digital.lib.washington.edu/researchworks/handle/1773/25092?show=full.

[32] C. H. E. Cheung, *Delamination Arrestment in Bonded-Bolted Composite Structures by Fasteners*, Ph.D. thesis, University of Washington (2016), available on URL:https://digital.lib.washington.edu/researchworks/handle/1773/36471.

[33] K. Lin, L. Richard, and W. Liu, *Delamination arrest fasteners in aircraft composite structures,* in *The 19th International Conference on Composite Materials Google Scholar* (2013).

[34] L. I. Richard and K. Y. Lin, *Analytical and experimental studies on delamination arrest features in aircraft composite structures,* in *56th AIAA/ASCE/AHS/ASC Structures, Structural Dynamics, and Materials Conference* (2015) p. 2066.

[35] L. Richard, P. Rodriguez, and K. Lin, *Analytical study of delamination arrest features in abaqus fea,* Proceedings of SAMPE , 23 (2016).

[36] L. I. Richard and K. Y. Lin, *Analytical and experimental studies on delamination arrest in bolted-bonded composite structures,* in *57th AIAA/ASCE/AHS/ASC Structures, Structural Dynamics, and Materials Conference* (2016) p. 1502.

[37] L. I. Richard and K. Y. Lin, *Analytical and experimental studies on delamination arrest in bolted-bonded composite structures,* in *58th AIAA/ASCE/AHS/ASC Structures, Structural Dynamics, and Materials Conference* (2017) p. 1602.

[38] L. I. Richard and K. Y. Lin, *Delamination arrest by fasteners in aircraft structures under static and fatigue loading,* in *2018 AIAA/ASCE/AHS/ASC Structures, Structural Dynamics, and Materials Conference* (2018) p. 2246.

[39] C. H. E. Cheung and K. Y. Lin, *Reliability of damage tolerance composite structure using fasteners as disbond arrest mechanism,* in *50th AIAA/ASME/ASCE/AHS/ASC Structures, Structural Dynamics, and Materials Conference 17th AIAA/ASME/AHS Adaptive Structures Conference 11th AIAA No* (2009) p. 2242.

[40] J. Schijve, *Fatigue of structures and materials in the 20th century and the state of the art,* International Journal of fatigue **25**, 679 (2003).

[41] T. Sinmazçelik, E. Avcu, M. Ö. Bora, and O. Çoban, *A review: Fibre metal laminates, background, bonding types and applied test methods,* Materials & Design **32**, 3671 (2011).

[42] G. Roebroeks, *Fibre-metal laminates: recent developments and applications,* International journal of fatigue **16**, 33 (1994).

[43] R. Alderliesten, *Fatigue crack growth propagation and delamination growth in GLARE*, Ph.D. thesis, Delft University of Technology (2005).

[44] T. Beumler, *Flying GLARE*, Ph.D. thesis, Delft University of Technology (2004), available at https://repository.tudelft.nl/islandora/object/uuid%3Acee40186-6a76-4843-b740-0c0df081b87e?collection=research.

[45] J. Pascoe, *Delamination of Bonded Repairs - A Damage Tolerance Approach*, Master's thesis, Delft University of Technology (2012), available on https://repository.tudelft.nl/islandora/object/uuid%3A38e5d9ac-8c04-48d5-801f-b0c9308f67fa?collection=education.

[46] V. Niranjan, *Bonded joints; a photoelastic study*, Tech. Rep. (University of Toronto, 1970).

[47] A. Vlot, S. Verhoeven, and P. Nijssen, *Bonded repairs for aircraft fuselages,* (1998).

[48] R. Alderliesten, *Fatigue and Fracture of Fiber Metal Laminates* (Springer International Publishing, 2017).

[49] S. Spronk, I. Şen, and R. Alderliesten, *Predicting fatigue crack initiation in fibre metal laminates based on metal fatigue test data,* International Journal of Fatigue **70**, 428 (2015).

[50] J. Pascoe, *Characterisation of Fatigue Crack Growth in Adhesive Bonds*, Ph.D. thesis, Delft University of Technology (2016), available at https://repository.tudelft.nl/islandora/object/uuid%3Aebbf552a-ce98-4ab6-b9cc-0b939e12ba8b?collection=research.

[51] J. Pascoe, R. Alderliesten, and R. Benedictus, *Methods for the prediction of fatigue delamination growth in composites and adhesive bonds–a critical review,* Engineering Fracture Mechanics **112**, 72 (2013).

[52] J. Schijve, *Fatigue of structures and materials* (Springer Science & Business Media, 2001).

[53] P. C. Paris, *The fracture mechanics approach to fatigue.* (1964).

[54] C. Rans, R. Alderliesten, and R. Benedictus, *Misinterpreting the results: How similitude can improve our understanding of fatigue delamination growth,* Composites Science and Technology **71**, 230 (2011).

[55] N. Blanco, E. K. Gamstedt, L. Asp, and J. Costa, *Mixed-mode delamination growth in carbon–fibre composite laminates under cyclic loading,* International journal of solids and structures **41**, 4219 (2004).

[56] R. Ramkumar and J. Whitcomb, *Characterization of mode i and mixed-mode delamination growth in t300/5208 graphite/epoxy,* in *Delamination and debonding of materials* (ASTM International, 1985).

[57] C.-G. Gustafson and M. Hojo, *Delamination fatigue crack growth in unidirectional graphite/epoxy laminates,* Journal of Reinforced Plastics and Composites **6**, 36 (1987).

[58] A. J. Russell and K. N. Street, *Predicting interlaminar fatigue crack growth rates in compressively loaded laminates,* in *Composite materials: fatigue and fracture, second volume* (ASTM International, 1989).

[59] C. Dahlen and G. S. Springer, *Delamination growth in composites under cyclic loads,* Journal of Composite Materials **28**, 732 (1994).

[60] G. Kardomateas, A. Pelegri, and B. Malik, *Growth of internal delaminations under cyclic compression in composite plates,* Journal of the Mechanics and Physics of Solids **43**, 847 (1995).

[61] M. Kenane and M. Benzeggagh, *Mixed-mode delamination fracture toughness of unidirectional glass/epoxy composites under fatigue loading,* Composites Science and Technology **57**, 597 (1997).

[62] J. Andersons, M. Hojo, and S. Ochiai, *Model of delamination propagation in brittle-matrix composites under cyclic loading,* Journal of reinforced plastics and composites **20**, 431 (2001).

[63] P. Cheuk, L. Tong, C. Wang, A. Baker, and P. Chalkley, *Fatigue crack growth in adhesively bonded composite-metal double-lap joints,* Composite Structures **57**, 109 (2002).

[64] M. Quaresimin and M. Ricotta, *Stress intensity factors and strain energy release rates in single lap bonded joints in composite materials,* Composites Science and Technology **66**, 647 (2006).

[65] P. Carraro, G. Meneghetti, M. Quaresimin, and M. Ricotta, *Crack propagation analysis in composite bonded joints under mixed-mode (i+ ii) static and fatigue loading: experimental investigation and phenomenological modelling,* Journal of Adhesion Science and Technology **27**, 1179 (2013).

[66] P. Carraro, G. Meneghetti, M. Quaresimin, and M. Ricotta, *Crack propagation analysis in composite bonded joints under mixed-mode (i+ ii) static and fatigue loading: a damage-based model,* Journal of Adhesion Science and Technology **27**, 1393 (2013).

[67] R. Jones, W. Hu, and A. Kinloch, *A convenient way to represent fatigue crack growth in structural adhesives,* Fatigue & Fracture of Engineering Materials & Structures **38**, 379 (2015).

[68] R. Jones, S. Stelzer, and A. Brunner, *Mode i, ii and mixed mode i/ii delamination growth in composites,* Composite Structures **110**, 317 (2014).

[69] R. Jones, S. Pitt, A. Bunner, and D. Hui, *Application of the hartman–schijve equation to represent mode i and mode ii fatigue delamination growth in composites,* Composite Structures **94**, 1343 (2012).

[70] L. F. da Silva, P. J. das Neves, R. Adams, and J. Spelt, *Analytical models of adhesively bonded joints—part i: Literature survey,* International Journal of Adhesion and Adhesives **29**, 319 (2009).

[71] T. Brussat, S. Chiu, and S. Mostovoy, *Fracture mechanics for structural adhesive bonds*, Tech. Rep. (LOCKHEED-CALIFORNIA CO BURBANK, 1977).

[72] C. Lin and K. Liechti, *Similarity concepts in the fatigue fracture of adhesively bonded joints,* The Journal of Adhesion **21**, 1 (1987).

[73] Y.-H. Lai, M. D. Rakestraw, and D. A. Dillard, *The cracked lap shear specimen revisited—a closed form solution,* International Journal of Solids and Structures **33**, 1725 (1996).

[74] D. Schmueser and N. Johnson, *Effect of bondline thickness on mixed-mode debonding of adhesive joints to electroprimed steel surfaces,* The Journal of Adhesion **32**, 171 (1990).

[75] G. Fernlund and J. Spelt, *Failure load prediction of structural adhesive joints: Part 2: Experimental study,* International journal of adhesion and adhesives **11**, 221 (1991).

[76] P. Cheuk and L. Tong, *Failure of adhesive bonded composite lap shear joints with embedded precrack,* Composites Science and Technology **62**, 1079 (2002).

[77] G. Fernlund, M. Papini, D. McCammond, and J. Spelt, *Fracture load predictions for adhesive joints,* Composites Science and Technology **51**, 587 (1994).

[78] W. Slager, *Static strength of riveted joints in fibre metal laminates*, Ph.D. thesis, Delft University of Technology (1994), available on URL:https://repository.tudelft.nl/islandora/object/uuid%3A5db80592-96ce-4007-82eb-0a37708a7c01?collection=research.

[79] *ASTM: Standard Test Method for Measurement of Fatigue Crack Growth Rates 1.*, pages: 1–43, Date: 03/07/1999.

[80] *Online github repository: Tudelft_msc_thesis_ivt,* Available on: https://github.com/IvarvanTeeseling/TUDelftMScThesisIvT.

[81] S. Tsai and H. Hanhn, *Introduction to composite materials* (Technomic Publishing Company Inc., 1980).

[82] M. Goland, *The stresses in cemented joints,* J. Applied Mechanics, Trans. ASME **66**, A (1944).

[83] MIL-HDBK, *5h: Metallic materials and elements for aerospace vehicle structures,* (1998).

[84] W. Schütz, *The prediction of fatigue life in the crack initiation and propagation stages—a state of the art survey,* Engineering fracture mechanics **11**, 405 (1979).

[85] M. Tsai and J. Morton, *An evaluation of analytical and numerical solutions to the single-lap joint,* International Journal of Solids and Structures **31**, 2537 (1994).

[86] J. Vaningen and A. Vlot, *Stress analysis of adhesively bonded single lap joints: Survey and evaluation of analyses,* NASA STI/Recon Technical Report N **94** (1993).

[87] S. Krenk, *Energy release rate of symmetric adhesive joints,* Engineering Fracture Mechanics **43**, 549 (1992).

[88] G. Fernlund and J. Spelt, *Mixed mode energy release rates for adhesively bonded beam specimens,* Journal of Composites, Technology and Research **16**, 234 (1994).

[89] Z. Suo and J. W. Hutchinson, *Interface crack between two elastic layers,* International Journal of Fracture **43**, 1 (1990).

[90] J. Williams, *On the calculation of energy release rates for cracked laminates,* International Journal of Fracture **36**, 101 (1988).

[91] *Asm aerospace specification metals inc.* Available on: "http://asm.matweb.com/search/SpecificMaterial.asp?bassnum=mtp641", (accessed: 04.12.2018).

[92] Fujifilm, *Fujifilm HS Instruction Manual*, Tech. Rep., available at http://www.spare.it/prescale-fuji/Fuji-Prescale-Film-LLLLW.pdf.

[93] Fujifilm, *Fujifilm HHS Instruction Manual*, Tech. Rep., available at http://www.spare.it/prescale-fuji/Fuji-Prescale-Film-LLLLW.pdf.